Metastable Helium BEC production and numerical simulation of a BEC in a bipartite optical lattice

By

Abbas Hussein

A thesis submitted in partial fulfillment of the
requirements for the degree of Doctor of Philosophy in Physics

Department of Quantum Science and Technology Research School of Physics, ANU, Canberra, Australia.

Metastable Helium BEC production and numerical simulation of a BEC in a bipartite optical lattice

Abbas Hussein

He* BEC group

Quantum Science & Technology department

Research School of Physics

Joint Colleges of Science

Australian National University
Canberra, Australia

Supervisory committee

Dr. Sean S. Hodgman,

Professor. Andrew G. Truscott,

Professor. Elena Ostrovskaya.

Declaration

I declare that the work in this dissertation was carried out at The He* Lattice Laboratory, The Research School of Physics and Engineering, The Australian National University, Canberra, Australia.

Except where acknowledged in a customary manner, the material presented in this thesis is, to the best of my knowledge, original and has not been submitted in whole or part of a degree in any university.

Abbas Hussein

March 2023

THE AUSTRALIAN NATIONAL UNIVERSITY

Acknowledgements

FIRST and foremost, I would like to praise Allah the Almighty, the Most Gracious and the Most Merciful for His blessings given to me during my study and in completing this thesis.

I would like to express my gratitude and appreciation to my supervisor, Dr. Sean Hodgman, who has given me valuable guidance, advice, and encouragement so I could complete this thesis on time. I also express my deepest gratitude to my co-supervisor, Prof. Andrew Truscott, for his endless support and guidance. Your encouraging words and advice have been very important to me. Moreover, I would like to extend my thanks to Prof. Elena Ostrovskaya for her insightful discussions.

A special thanks to the teammates Bryce Henson, David Shin, and Rohit Patil. In particular, I appreciated Jacob Ross for his fruitful discussion and encouragement. A lot of credit is also due to my lab companion, Samuel Meng, who provided me with much-appreciated support and help while working in the lab. Also, we appreciate the technical support available at RSPhy. I would like to thank Ross Tranter and Colin Dedman for providing assistance with an enthusiastic attitude.

Last, but not least, my sincere gratitude goes to my family, especially my beloved wife, Hend for the tremendous support and hope she has given me. Without that hope, this thesis would not have been possible. A huge thanks to my children, Haneen and Yassin for their unwavering love and support, which provided me with a renewed perspective and motivation during challenging times.

I am grateful to all of you for your unwavering support and encouragement, which provided me with the strength and resilience to successfully complete this thesis.

Contents

This page intentionally left blank.

List of Figures

Dissertation Overview

Bose-Einstein condensates (BECs) using metastable helium atom (He*) provide an ideal setting for manipulation and control of quantum many-body systems. Due to the capability of single-atom detection, BEC with metastable helium atoms has demonstrated unprecedented insight into such systems, exposing their dynamics and correlations on the microscopic scale. Unlike alkali gases, the realization of He* BEC occurs in its metastable state 2^3S_1 rather than the electronic ground state. Owing to a lifetime of more than two hours, the helium triplet state 2^3S_1 can be considered an effective ground state in experiments. With its considerable internal energy (19.8 eV per atom), single-atom detection with high precision is possible when a He atom hits a multi-channel plate (MCP). This advantage can be employed for single-atom-resolved measurements of correlation functions, which allow probing quantum phenomena with high spatial and temporal resolution.

Furthermore, beyond directly studying coherent matter waves, ultracold atoms in optical lattice potentials serve as an artificial platform to emulate quantum condensed matter phenomena in a periodic landscape. They can be used to examine a variety of systems, ranging from strongly correlated systems to implementations in information technology, where a neutral atom inside optical lattice sites serves as a quantum qubit. Due to their high controllability, optical lattices can be spatially reconfigurable, which offers the possibility to study rich and complex dynamics. In particular, optical lattices with higher band occupation allow investigating physics beyond the tight-binding model and mimicking exotic quantum states such as unconventional Bose-Einstein condensates (UBECs) and topological superfluids.

This work describes two main projects: (1) experimental realization of He* BEC in an optical dipole trap and (2) dynamics of an interacting condensate in the p-band of a bipartite optical lattice potential.

First, we report a rapid generation of He* BEC in a crossed-beam optical dipole trap using an in-vacuum coil magnetic trap. A magnetic trap with 10 G bias generated by a quadrupole-Ioffe configuration made from in-vacuum hollow copper tubes provides fast switching times without compromising optical access. The bias enables in-trap one-dimensional Doppler cooling to be used, which is the only cooling stage between the magneto-optic trap (MOT) and the optical dipole trap. This allows direct transfer to the dipole trap without the need for any additional evaporative cooling in the magnetic trap. The entire experimental sequence takes 3.3 s, with essentially pure BECs observed with $\sim 10^6$ atoms after evaporative cooling in the dipole trap.

Second, we apply the coupled-mode theory to study the stationary states of an interacting condensate loaded into the p-band of a bipartite optical lattice potential. In the plane-wave basis, we analyze the linear band-gap structure and the associated Bloch states. The geometry of the first excited state is tuned such that two degenerate energy minima are formed at the quasi-momentum of the first Brillouin zone (FBZ), where the cold atomic cloud condenses. At the two degenerate minima, Bloch states are formed via hybridization of the s- and p-orbitals of the individual lattice sites with $\pi/2$ phase shift. The steady-state solutions of condensate in the p-band of a 1D 2D bipartite optical induced potential are studied. In the isotropic-2D bipartite optical lattice, we show that these two modes can form a 2D vortex array with a global orbital angular momentum across the entire lattice, which can be explained as a chiral superposition of 2D Bloch states in the two degenerate band minima.

Finally, a full band gap is observed between the ground and the first excited bands, indicating a possibility of two-dimensional spatial localization. The study is extended to investigate the localization of a nonlinear matter wave in a 2D bipartite optical lattice. We find that a 2D bipartite optical lattice admits monopole and dipole gap solitons. Moreover, gap solitons with different spatial extents bifurcate from the upper edge of the first excited state into the second bandgap under a defocusing nonlinearity. These findings are highly relevant to localized structures in nonlinear optics and atomic matter waves.

Thesis outline

This thesis presents work comprised of two parts: The first part represents an experimental scheme for rapid production of He* BEC in a cross-beam optical dipole trap, which is covered in chapters 1 & 2. In the second part, we introduce a numerical simulation on interaction-induced states of a condensate, which is loaded into the p-band of a bipartite optical lattice, which is discussed in chapters 3, 4 & 5.

This thesis is arranged as follows:

- In the next chapter, we cover in brief a theoretical background to describe BECs. The experimental techniques required to achieve BECs such as laser cooling, and magneto-optical trap will be covered. The principle of trapping neutral atoms in an optical dipole trap is provided in the next section. We also explain two different probing and detection schemes used in our experimental setup. We conclude this chapter by presenting a few aspects of metastable helium and its level structure.

- Chapter 2 describes the experimental apparatus setup in detail, starting with the source chamber where helium atoms are excited to the 2^3S_1 metastable state, then slowing down the atomic beam using a two-stage Zeeman slower, which is terminated at our first MOT. Finally, we explain the science chamber where the second MOT loading, magnetic trap, cross-optical dipole loading, and evaporative cooling are performed. Characterization and analysis of the cooling stage are described. Physical parameters such as temperature T and the number of atoms N at different stages are also discussed using an optical detection method (absorption imaging) and/or electronic method (MCP). We end this chapter by summarizing and concluding the important results.

- Chapter 3 presents a theoretical background to optical lattice potential. A brief introduction to the Bloch theorem for a periodic potential is presented. Also, the physical principles involved in topological states such as a chiral state are discussed in this chapter.

- In chapter 4, we demonstrate the possibility to create a superposition of Bloch states with a nontrivial orbital texture in the second band of a bipartite optical lattice potential. We start by analyzing the linear spectrum and Bloch states associated with the first excited state. Then, the stationary state of a weakly interacting condensate in the p-band of a bipartite optical potential is analyzed using the coupled mode theory.

- In chapter 5, we numerically investigate the localization of nonlinear matter waves in a 2D bipartite optical potential. The non-linear Schrodinger equation is solved in the first and second bandgap using the Newton-conjugate algorithm. Self-localized gap soliton states under both focused and defocused nonlinearity are observed. A conclusion and summary of our findings are presented in the last section.

- Finally, chapter 6 provides a summary and conclusion of all the results presented in this thesis. Outlook and possible future work are also discussed.

List of publications

- Rapid generation of metastable helium Bose-Einstein condensates
  A. H. Abbas, X. Meng, R. S. Patil, J. A. Ross, A. G. Truscott, and S. S. Hodgman.
  Phys. Rev. A 103, 053317(2021).

- Chiral superfluid in a one-dimensional bipartite optical lattice
  A. H. Abbas.
  Phys. Rev. A 105, 023327(2022).

- Nonlinear localization of Bose-Einstein condensates loaded into a square bipartite optical lattice.
  A. H. Abbas, A. G. Truscott, S. S. Hodgman and E. Ostrovskaya
  under preparation

Part I

Metastable Helium (He*) BEC production

This page intentionally left blank.

Chapter 1

Ultracold atoms: theory and experiment

BOSONS are particles with integer spin. Unlike a system of fermionic particles, their wave function is symmetric under the interchange of any two particles. There is no restriction on the number of Bosons residing in the same quantum state. Consequently, under certain conditions bosons can accumulate into one quantum state and form *Bose-Einstein condensation*.

Experimental realization of BEC state requires cooling and trapping of atoms. For this purpose, light-induced forces combined with magnetic field gradients can be used. In the following sections, we cover the basic concept of Doppler cooling, magneto-optical, and optical dipole trap, which play a crucial part in the creation of a BEC. The fundamental ideas of the detection methods used in our experimental setup, such as absorption imaging and the multi-channel plate detector (MCP), will also be covered. This section concludes by explaining certain aspects of the metastable state of helium atoms as well as the laser source employed in our experiment.

1.1 Theory of Bose-Einstein condensation

BEC is a novel state of matter in which a macroscopic fraction of particles of an ensemble of bosonic atoms condenses into a single quantum state. The ensemble exhibits collective quantum behavior on the macroscopic scale due to the indistinguishability of the constituent particles [1, 2]. This state was initially proposed by A. Einstein based on the well-known black-body radiation formula of a quantized massless harmonic oscillator derived by S.N. Bose. Einstein pointed out that a system of arbitrary particles satisfying Bose statistics should exhibit an exotic phase transition at a specific critical temperature T_c. Below this critical temperature, a significant fraction of particles occupies a single quantum mechanical state of the system.

BEC is a direct consequence of three quantum mechanical effects; the indistinguishability of particles, the quantized energies allowed for each particle due to the wave nature of atoms, and violation of the Pauli exclusion principle, which is only true for bosonic particles. In quantum mechanics particles are indistinguishable, and due to the indeterministic nature of particles, their positions and trajectories are defined only in a probabilistic sense. In contrast, classical particles are distinguishable and their trajectories are determined. In order to quantify this peculiar state, phase-space density is the key parameter that characterizes the onset of BEC in accordance with wave-particle duality [1].

$$n\lambda_T^3 = Nh^3/V(2\pi mk_BT)^{3/2},$$

where n is the particle number density of the ensemble. The quantity λ_T is the particles thermal wavelength $\lambda_T = \sqrt{h^2/(2\pi mk_BT)}$. The thermal wavelength λ_T can be interpreted as the uncertainty of the position associated with the thermal momentum distribution. The quantity ($n\lambda_T^3$) can be a very appropriate parameter to capture the physics of such a system in a simple way. In a simplified picture, an atom in a canonical ensemble can be represented as a wave packet with a spatial extension of the order of the thermal wavelength λ_T. For relatively high temperatures, the thermal wavelength is negligible and the phase-space density ($n\lambda_T^3$) goes to zero, and the system behaves in a classical manner and does not show any quantum feature. As the temperature is lowered, λ_T increases, and for sufficiently high density n, the thermal wavelength becomes comparable to the mean inter-particle spacing $d = n^{-1/3}$, where the onset of the degenerate phase (i.e $nd^3 = 1$) occurs. Below this point, the overlap of the single particle wavefunctions becomes significant (

$n\lambda_T^3 \geq 1$). The individual particle loses its identity and becomes indistinguishable. This leads to the conclusion that BEC occurs if the temperature is sufficiently low and/or the density of particles is sufficiently high.

1.1.1 BEC in an ideal gas

In the framework of the grand canonical ensemble, the average occupation of a single particle state with energy ϵ_p and a chemical potential μ for a non-interacting Bose gas at thermodynamic equilibrium is given by the Bose statistics [1]

$$n(\epsilon_p) = \frac{1}{e^{\beta(\epsilon_p - \mu)} - 1}, \tag{1.1}$$

where $\beta = 1/k_B T$, k_B is Boltzmann's constant, T is the temperature and μ is the chemical potential of the system. Eq.(1.1) implies a physical constraint for the chemical potential of a Bose gas $\mu \leq \epsilon_0$, where ϵ_0 is the lowest energy eigenvalue of the single-particle Hamiltonian. Violation of this condition would result in a negative occupation number of the states, which cannot be true. The total number of particles in the ensemble is obtained by the sum of the occupancies of the single particle state

$$N = \sum_p n(\epsilon_p) = \sum_p \frac{1}{e^{\beta(\epsilon_p - \mu)} - 1}. \tag{1.2}$$

As the temperature reaches the critical temperature T_c, particles start to accumulate in the ground state of the system. The total atom number can be expressed as,

$$N = N_0 + N_{th}, \tag{1.3}$$

where N_0 is the number of particles that reside in the lowest quantum state. N_{th} represents the number of particles distributed among excited states. In the thermodynamic limit, the summation over the discrete index p is replaced by integration. We have at the onset of Bose condensation

$$N_{th} = V/\lambda^3 g_{3/2}(z), \tag{1.4}$$

where $g_\nu(z) = 2/\sqrt{\pi} \int x^{\nu-1} dx / z^{-1} e^x - 1$ ($\nu = 3/2$) is called the Bose Einstein function [1] with $z = e^{\beta\mu}$. For $T = T_c$, $N = N_{th}$, one can obtain

$$T_c = \frac{2\pi\hbar^2}{m k_B} \left[\frac{n}{g_{3/2}(1)} \right]^{2/3}, \tag{1.5}$$

where $g_{3/2}(1) = \zeta(3/2) \sim 2.612$. The above equation shows that the critical temperature is inversely proportional to the mass of a particle, which means a high T_c is attainable in a system of the high density of light atoms such as H or He.

In fact, the ideal Bose gas is not a realistic model since it lacks inter-particle interactions, which are not negligible at sufficiently low temperatures. For a weakly interacting Bose gas, the effect of inter-particle interactions is captured by the low energy $s-$wave scattering length a, while configurations involving high-order interaction can be safely neglected. In this system, the stationary many-body wavefunction cannot be simply the product $|\Psi\rangle = |\psi_p\rangle^N$ of the single particle state $|\psi_p\rangle$. To account for this, the Penrose-Onsager criterion [3, 4] introduces the single-particle density matrix, which is the expectation value of the one-body field operator

$$\rho^{(1)} = Tr\left(\rho\hat{\Psi}^{\dagger}\hat{\Psi}\right).$$

An eigenvalue of $\rho^{(1)}$ gives the occupation probability of the corresponding eigenvector, which is a superposition of non-interacting eigenstates. Under the Penrose-Onsager criterion, the system exhibits BEC if one of the eigenvalues of $\rho^{(1)}$ is proportional to N in the thermodynamic limit.

Realization of BEC requires slowing down the atoms and holding them in a trap. Since most of the traps considered in cold atom experiments are approximated as a harmonic trap near their centers to the lowest order, in what follows we present some analytical results derived for a non-uniform Bose gas in a harmonic trap. Furthermore, at sufficiently low temperatures, the effect of two-body interactions cannot be neglected. As a result, the physical parameters such as the transition temperature and density will be altered compared to the uniform ideal Bose system.

1.1.2 BEC in a harmonic trap

Consider a system of an interacting Bose gas confined in an anisotropic harmonic potential given by [1, 2]

$$V(r) = \frac{1}{2}m(\omega_x^2 x + \omega_y^2 y^2 + \omega_z^2 z^2) \tag{1.6}$$

with oscillator frequencies $\omega_{x,y,z}$. The effective interaction between two particles at low energies is dominated by $s-$wave scattering with the interaction strength $U_0 = 4\pi\hbar^2 a/m$ resulting in the contact potential $U = U_0\delta(r - r_0)$.

In the condensed state, all N bosons occupy the same single-particle state, $\phi(r)$, and therefore the many-body wavefunction can be expressed as a symmetrized product of single-particle wavefunctions

$$\psi(r_1, ..r_N) = \prod_{i=1}^{N} \phi(r_i).$$

The effective Hamiltonian can be written as

$$\hat{H} = \sum_{i}^{N} \frac{p_i^2}{2m} + V(r_i) + U_0 \sum_{i<j} \delta(r_i - r_j), \tag{1.7}$$

where $V(r)$ is the external trapping potential.

The short-wavelength modes are integrated out by assuming slow variations in the density using the Born approximation and therefore one can derive the Gross-Pitaevskii equation (GPE)

$$i\hbar\frac{\partial\psi(t,r)}{\partial t} = -\frac{\hbar^2}{2m}\nabla^2\psi(t,r) + V(r)\psi(t,r) + U_0|\psi(t,r)|^2\psi(t,r), \tag{1.8}$$

where m is the mass of the particle and $\hbar$ is Planck's constant.

The GPE (1.8) is a mean field equation that describes the collective dynamics of the weakly interacting BEC at zero temperature. The first term accounts for the kinetic energy of the system and the effect of the external potential is included in the second term. The effective interparticle interactions between the particles are accounted for in the non-linear $U_0|\psi(t,r)|^2$ coupling term. Due to the nonlinearity of the GPE approximations should be implemented to find its solution. Considering the harmonic trap (1.6) as the potential term in (1.8) some analytical results can be derived under certain conditions. It should be pointed out that in the weak interacting limit ($U_0 n \ll \hbar\omega_{x,y,z}$), the interaction term is negligible. Hence, the condensate wavefunction can be expressed as the ground state of the harmonic oscillator. More importantly, when ($U_0 n \gg \hbar\omega_{x,y,z}$) the strong coupling regime is reached, where the effect of kinetic energy can be omitted compared to the interaction term. This is the so-called *Thomas-Fermi approximation*, whereby the density profile $n(r)$ of the condensate shows an inverted parabola form

$$n(r) = max\left(\frac{\mu - V(r)}{U_0}, 0\right), \tag{1.9}$$

where μ is the chemical potential determined by the normalization condition of the wave-function $\psi(r)$

$$\mu = \frac{\hbar\bar{\omega}}{2}\left(\frac{15Na}{\bar{a}}\right)^{2/5}, \tag{1.10}$$

with $\bar{\omega} = (\omega_x\omega_y\omega_z)^{1/3}$ is the geometric frequency and $\bar{a} = \sqrt{\hbar/m\bar{\omega}}$ is the harmonic oscillator length.

Since the particle density cannot be negative ($\mu - V(r) \geq 0$), the spatial extent of the cloud is determined such that $V(r) = \mu$, which defines the *Thomas-Fermi radii*

$$R_i = \sqrt{2\mu/m\omega_i^2}. \tag{1.11}$$

It is possible to visualize the condensate in the Thomas-Fermi limit as filling the trapping potential up to the height of the chemical potential μ, which is determined by $\mu = 1/2m\omega_i^2 R_i^2$, $i = x, y, z$. The peak density of the condensate in the harmonic trap has a parabolic profile, given by

$$n_0(r) = \frac{15}{8\pi}\frac{N_0}{R_xR_yR_z} max\left(1 - \left(\frac{x}{R_x}\right)^2 - \left(\frac{y}{R_y}\right)^2 - \left(\frac{z}{R_z}\right)^2, 0\right). \tag{1.12}$$

The density goes to zero beyond the Thomas-Fermi radii. The onset of condensation is achieved at the transition temperature T_c

$$\begin{aligned} T_c &= \frac{\hbar\bar{\omega}}{k_B}\left(\frac{N}{\zeta(3)}\right)^{1/3} \\ &\sim 0.94\frac{\hbar\bar{\omega}}{k_B}N^{1/3} \end{aligned}$$

when the inter-particle interaction is ignored, the condensed fraction below the critical temperature is given as

$$\frac{N_0}{N} = 1 - \left(\frac{T}{T_c}\right)^3. \tag{1.13}$$

Assuming repulsive interactions between particles, a negative shift in the transition temperature will occur, as the density will be reduced which will require decreasing the temperature. Interaction effects are significant for higher N. It can be measured in term of the interaction parameter η_0, which is the ratio of the chemical potential μ and thermal energy k_BT

$$\eta_0 = \frac{\mu}{k_BT_c} = \frac{\zeta(3)^{1/3}}{2}\left(15N^{1/6}\frac{a}{a_{ho}}\right)^{2/5}. \tag{1.14}$$

This results in a negative shift of the critical temperature: $\delta T/T_c = -0.43\eta_0^{5/2}$, which is more significant in the thermodynamic limit.

1.2 Experimental realization of BEC

The standard route to achieve condensation starts with laser cooling based on radiation pressure caused by a slightly off-resonance laser beam, followed by trapping and evaporative cooling in a magnetic trap and/or optical dipole trap. The realization of BEC can be confirmed by an abrupt increase in the cloud phase space density. The following sections are concerned with the techniques involved in the experimental realization of BEC. The key experimental procedures needed to create a BEC in the lab will be covered.

1.2.1 Laser cooling

According to the detuning of a laser beam relative to a resonant transition of an atom, the light field interacts with neutral atoms in either a destructive or a conservative way [5]. The momentum transfer due to the absorption and spontaneous emission of photons results in a dissipative force on the atoms, which is used for laser cooling and magneto-optical traps. In contrast, the conservative interactions result in the AC-Stark shift in the potential energy which provides a trapping potential for the neutral atoms, which will be covered later.

Suppose a laser beam with frequency ω_L and intensity I is incident on a two-level stationary atom in the ground state E_g. The beam is slightly detuned by $\delta = \omega_L - \omega_0$ relative to the resonant atomic frequency $\omega_0 = (E_e - E_g)/\hbar$, where E_e is the excited state. The dissipative force caused by the absorption and emission of the photons is given by [6]

$$F_{dis} = \hbar k \Gamma_{sc}, \tag{1.15}$$

where k is the wavevector of the laser beam and Γ_{sc} is the scattering rate of the photons,

$$\Gamma_{sc} = \frac{\gamma}{2} \frac{s_0}{1 + s_0 + (2\delta/\gamma)} \tag{1.16}$$

where $s_0 = I/I_{sat}$ is the relative saturation parameter, I_{sat} is the saturation intensity and γ is the decay rate of the transition. The photon scattering rate (1.16) is maximum for the high-intensity limit $s_0 \gg 1$ i.e $I \gg I_{sat}$, which becomes simply half of the natural linewidth $\gamma/2$ and therefore the scattering force reaches its maximum.

In the process, the laser frequency is slightly red-detuned with respect to the electronic transition state of the atom. Thus, the atoms will absorb the light photons as they travel toward the light source due to the Doppler effect (see Fig. 1.1(a)). Consequently, over a few cycles of absorption and spontaneous emission of the light photons, the average speed and kinetic energy of the atom will decrease. Subsequently, the temperature of the atomic cloud will be reduced, which causes the cooling of the atoms.

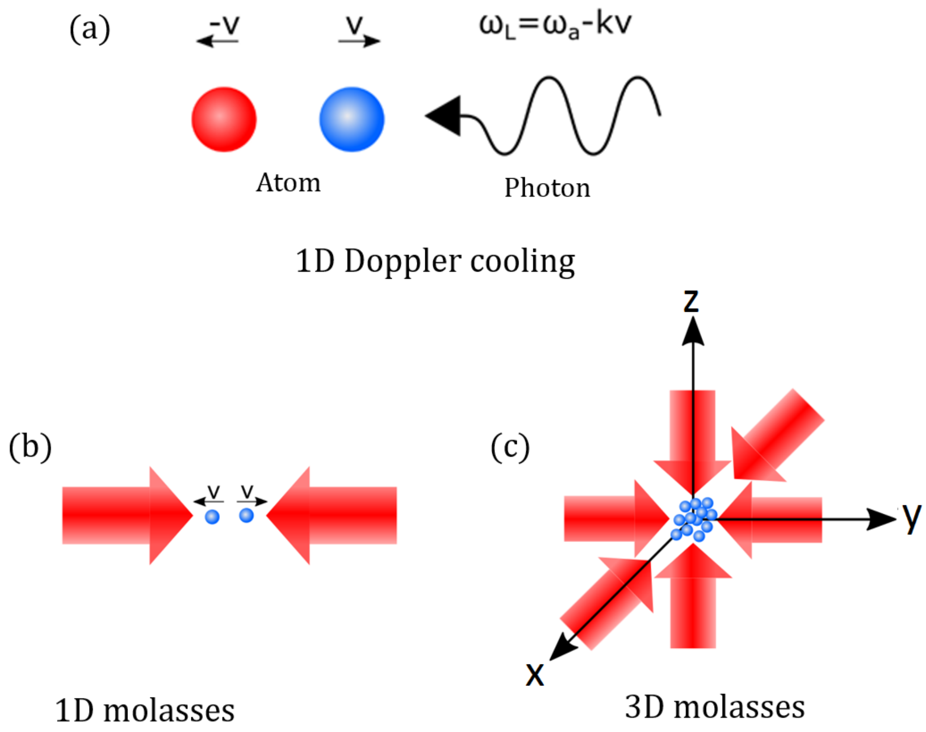

Figure 1.1: (a) One-dimension Doppler cooling. Configuration of laser beams for (b) a one-dimensional (c) three-dimensional optical molasses. A pair (three pairs) of counter-propagating laser beams detuned by δ from the atomic resonance for 1D (3D) optical molasses.

Consider an atom moving with a velocity v, the apparent frequency of the light photon will be shifted to $\omega_L^{'} = \omega_L + \omega_D$, where $\omega_D = -k.v$ is the Doppler shift. This causes an increase in laser frequency seen by the atoms moving into the beam. Thus, the laser frequency is detuned by the amount δ to compensate for the Doppler shift seen by the atoms. As a result of the detuning, atoms moving towards the laser beam are shifted closer to resonance, and thus experiencing a force in the direction of laser beam propagation. Given that, using a single laser beam, the atoms can be slowed down in one direction (opposite to the laser beam propagation).

The atoms can thus be stopped in 1D by implementing an additional counter-propagating laser beam to reduce the motion in the opposite direction as shown in Fig. 1.1(b),(c). Consequently, an opposed friction force is proportional to the velocity of the atomic beam, which will cool it along the beam propagation direction. This configuration is known as an *optical molasses*. Moreover, in 3D additional pairs of counter-propagating beams can be implemented along the other spatial axes to slow atoms moving along these directions.

Optical molasses has a limitation on the temperature achievable using laser dissipative cooling due to the non-zero average kinetic energy added to the system during the absorption-emission cycles. The minimum attainable temperature -*Doppler limit*- is given by $T_D = \frac{\hbar\gamma}{2k_B}$. For He* (in our case), T_D is about 40 μK. Since the laser detuning is fixed in the above approach, and after a photon absorption-emission cycle the speed of the atom would be reduced, as a result, the resonance condition $\omega_0 = \omega_L + kv$ would also no longer be fulfilled, and the slowing process will stop. However, this can be overcome by applying a spatial field gradient technique called a *Zeeman slower* (will be discussed later). By implementing this elegant approach, the photon absorption-emission cycles will continue, since the Zeeman slowing will compensate for the Doppler shift.

1.2.2 Magneto-Optical Trap

A pair of coils in an anti-Helmholtz configuration is used to form a weak quadrupolar magnetic field. A locally linear magnetic strength near the trapping region is created with a gradient of the form $(B', B', 2B')$. According to the Maxwell equation $\nabla B = 0$, the field gradient is twice along the stronger axis, which implies that the trapping force will be twice as strong along this axis. The field varies linearly with the position in the proximity of the field zero. In addition to three pairs of counter-propagating laser beams with circular polarisation in opposite directions (σ_+, σ_-) as shown in Fig. 1.2.

To explain the basic principle of a MOT, consider a two-level system with angular momentum states $J = 0$ and $J = 1$. Due to the Zeeman shift, these states will each be split into $2J + 1$ magnetic substates M, where J is the magnitude of the angular momentum vector. Therefore, a spatially-dependent energy shift of the excited-state sub-levels will occur. The laser beams are circularly polarized and red-detuned from the transition $J = 0 \rightarrow J = 1$ by an amount $\delta = \omega_0 - \omega > 0$. According to the selection rules, a σ_+

polarised beam will drive the atomic transitions between two states such that the magnetic substate $\Delta M = +1$, and $\Delta M = -1$ for a σ_- beam. The three magnetic substates $M_e = -1; 0; 1$ of the excited state $J = 1$ split in energy by different amounts as shown in Fig. 1.3.

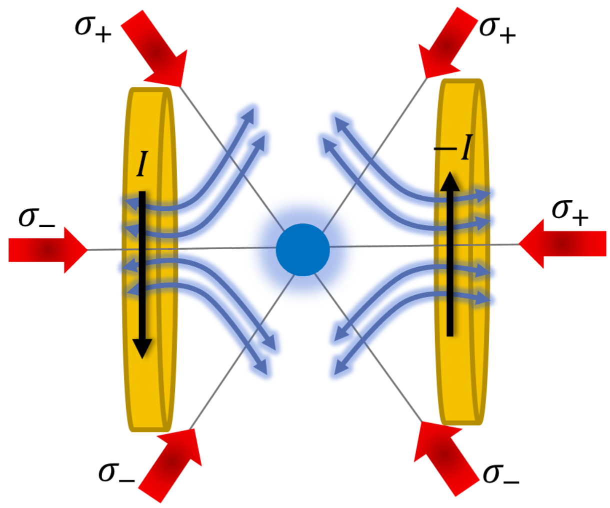

Figure 1.2: A diagram shows the geometry of a MOT. It is formed of a quadrupole magnetic field (shown in blue) generated by a pair of anti-Helmholtz coils in addition to three pairs of circularly polarized laser beams (shown in red) overlapped at the trap center.

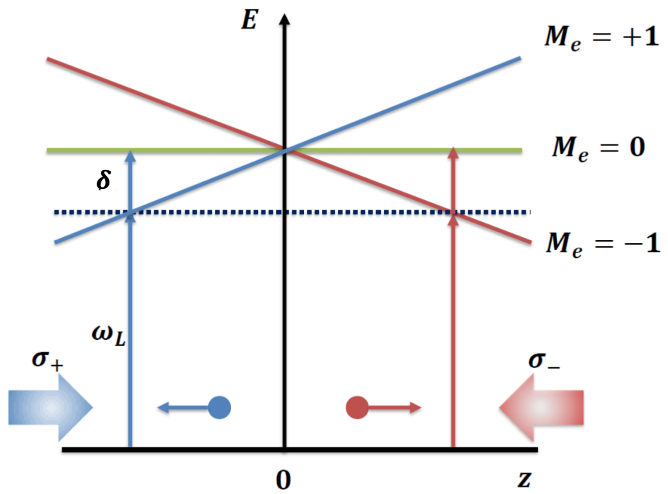

Figure 1.3: The principle of a 1D-MOT for a two-level atom with angular momentum states $J = 0$ and $J = 1$. The two-level atom is subjected to an inhomogeneous magnetic field gradient. In 1D, a pair of counter-propagating red-detuned laser beams with circular polarization exerts a restoring force on the atoms.

At the center of the trap, the magnetic field is zero and the Zeeman shift is zero. Hence the atoms are not in resonance with the laser beams and remain unchanged. The sublevel $M_e = +1$ and $M_e = -1$ are shifted up and down in energy respectively by $\Delta E = g\mu_B \alpha z$ where g is the Lande g-factor and μ_B is the Bohr magneton. As an atom moves further away from the origin towards the positive or the negative direction, it will come into resonance with one of the molasses beams in this direction, thus would absorb a photon, which reduces its momentum. This position-dependent force exerted by the laser beam on the atoms pushes them toward the center ($z = 0$), where they are trapped.

1.2.3 Optical trapping potential

The final cold state of a bosonic system can be confined by an extremely shallow optical dipole trap. Significant transfer efficiencies are achieved in very far-detuned potentials where the resonant excitations are negligibly small [7]. An optical trap allows the investigation of many aspects of BECs that are not accessible in common magnetic traps.

Unlike laser cooling and magneto-optical traps, an optical dipole trap relies on the conservative interaction of the light-induced dipole moment of an atom when it is subjected to a light field. This conservative interaction results from an AC-Stark shift in the potential energy to create a trapping potential for neutral atoms. In this case, the dissipative forces are suppressed by the very far-detuning of the light.

An electric dipole moment can be induced when an atom is illuminated by a light field. The induced dipole moment oscillates at the same frequency ω_L of the electric field E with the complex amplitude d given by,

$$d = \alpha(\omega_L)E, \tag{1.17}$$

where $\alpha(\omega_L)$ is the complex polarizability, which depends on the laser frequency ω_L. The interaction potential is defined in terms of the time average of

$$V_{dip} = -\frac{1}{2}\langle dE\rangle = -\frac{1}{2\epsilon_0 c}Re(\alpha)I. \tag{1.18}$$

The resulting dipole potential energy of the atom in the light field is proportional to the intensity of the laser field $I \propto |E|^2$ and the real part of the polarizability $Re(\alpha(\omega_L))$, which can be determined using Lorentz's model of a damped oscillator. This gives

$$\alpha(\omega_L) = 6\pi\epsilon_0 c^3 \frac{\Gamma/\omega_0}{\omega_0^2 - \omega_L^2 - i(\omega_L^3/\omega_0^2)\Gamma}, \tag{1.19}$$

with ω_0 the resonance frequency and Γ the on resonance damping rate. Substituting Eq. (1.19) into (1.18), the strength of the dipole potential is found to be,

$$V_{dip}(r) \approx \frac{3\pi c^2}{2\omega_0^3}\frac{\Gamma}{\delta} I(r). \tag{1.20}$$

The trapping potential in Eq. (1.20) is directly proportional to the intensity of the light field, with the sign determined by the laser detuning (see Fig. 1.4). The potential is repulsive for blue detuned light ($\delta > 0$), and attractive for red detuned light field ($\delta < 0$). The intensity profile for a Gaussian laser beam can be expressed as

$$I(r;z) = \frac{I_0}{\sqrt{1+(z/z_R)^2}} e^{r^2/2w(z)^2},$$

where $w(z) = w_0\sqrt{1+(z/z_R)^2}$ is the beam waist and $z_R = \pi w_0^2/\lambda$ is the Rayleigh length. The atom will experience a conservative force given by

$$F_{dip}(r) = -\nabla V_{dip}(r) \propto -\nabla I(r). \tag{1.21}$$

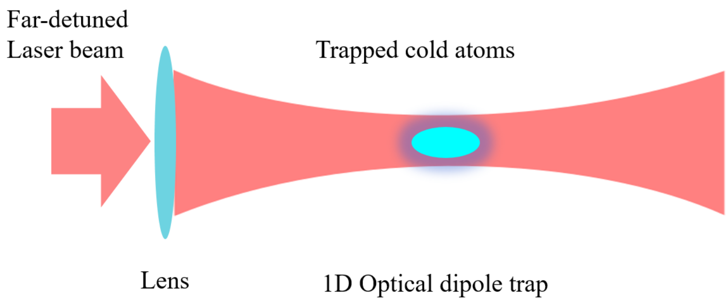

Figure 1.4: A trapping geometry of a single beam- optical dipole trap. A far-detuned laser field induces a dipole moment in the atom, which results in the atom being attracted and trapped to the focal region, where the field is strong.

The resulting force is proportional to the gradient of the intensity of the laser beam, which means that a focused gaussian beam will have a force increasing towards the focus of the beam, and thus a trap will be formed from a single focused laser beam. For $\delta < 0$ the laser beam is red-detuned, which forms an attractive potential that confines the atomic cloud in the region of high intensity. The potential formed will have a radial component that is approximately harmonic near the center at the beam waist, and longitudinal potential along the propagation axis. A blue detuned laser beam with $\delta > 0$ can form a dipole trap with the right intensity profile, however, this will not be discussed in this thesis.

The stability of a dipole trap is based on the minimization of the heating rate due to the dissipative interaction from the trapping beam. The photon scattering rate Eq. (1.16) is proportional to $1/\delta^2$, while the dipole force Eq. (1.19) scales inversely with the detuning parameter, which means the heating rate will decrease faster than the trap potential as the detuning increases. Because both are also linear with I, for a laser with sufficient detuning to minimize the spontaneous heating yet large enough power to still confine atoms, a stable trap can be created.

1.2.4 Probing BEC

Measuring physical parameters such as temperature T or density n for various regimes of the condensate can be achieved optically or electronically. The absorption imaging technique relies on the illumination of the atomic cloud with a laser beam at resonance. Electronically, a *Multi-channel plate* and *Delay-line detector* are used to construct a far-field profile for energetic atoms (He^* in our case). Here we provide a brief description of each method used in our experimental setup. The absorption imaging technique and multi-channel plate were utilized to collect the data presented in this work.

Absorption Imaging

Absorption imaging is a common imaging technique used in cold atom experiments. It provides information about the atom number and the average temperature of the atomic cloud. A low-intensity near-resonant laser beam tuned to excite the desired atomic transition is directed at the cold atomic sample into the vacuum chamber. A CCD camera captures the image of the shadow cast by the cloud after absorbing the light, which allows the cloud density and temperature to be estimated.

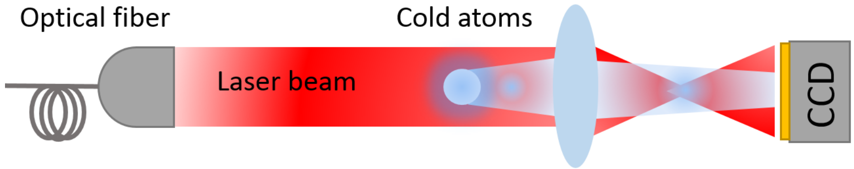

Figure 1.5: Schematic of the absorption imaging setup. A near-resonance laser beam is shone on an atomic cloud. Light photons are scattered by the atoms and the shadow created is imaged by a CCD camera.

Fig. 1.5 illustrates the general scheme of absorption imaging. The amount of photons absorbed by the cloud is proportional to the optical density. According to Beer's law, the attenuation of the initial beam intensity I_0 along the imaging axis is given by

$$I = I_0 e^{-OD},$$

If the intensity of the incident laser beam is below saturation, then the above equation can be rewritten in terms of the column density of the atomic cloud, $n(x, y)$:

$$I = I_0 e^{-\sigma n(x,y)}$$

where σ is the absorption cross-section. Experimentally, the optical density can be measured by measuring the incoming and outgoing intensities of the laser beams. However, in order to obtain a clearer image, a reference image without an atomic cloud is taken a few milliseconds after the first image with the same exposure time, which normalizes the background noise caused by scattered light, beam movement, etc. The 2D absorption profile can be represented in terms of the ratio of pixel intensities in the presence of atoms I_{abs} to the reference image as

$$OD(x, y) = \frac{I_{abs} - I_{dark}}{I_{ref} - I_{dark}},$$

for detection and analysis of clouds released from the trap, the quantity $OD(x, y)$ is integrated along the x and y directions to obtain the total atom number N.

$$N = \frac{1}{\sigma} \int OD(x, y) dxdy.$$

Far-field single atom detection

Thanks to the large internal energy of the metastable helium atom, single-atom detection with high temporal and spatial precision are possible using a *multi-channel plate (MCP)* and a *Delay Line Detector (DLD)*. The MCP-DLD system is an important component in the detection and analysis of the dynamics of ultra-cold atoms in a controlled environment, including their cooling dynamics, kinetic energy distribution, and correlation functions. In order to accurately measure and analyze these interactions, it is important to have a high-sensitivity and accurate detection system.

MCP assembly is a specially designed plate consisting of a pair of stacked discs each of which is made of array pores serving as an electron multiplier (see Fig. 1.6). The upper surface is mounted below the center of the magnetic trap.

Since the internal energy of He* ($\sim 19.8eV$) is greater than the work function for typical metals ($\sim 5eV$), a single atom will liberate an electron (or even several) in the event of a He* atom hitting the MCP surface. A potential difference of $\sim$ 2.2 KV is adjusted between the front and back faces of the MCP assembly.

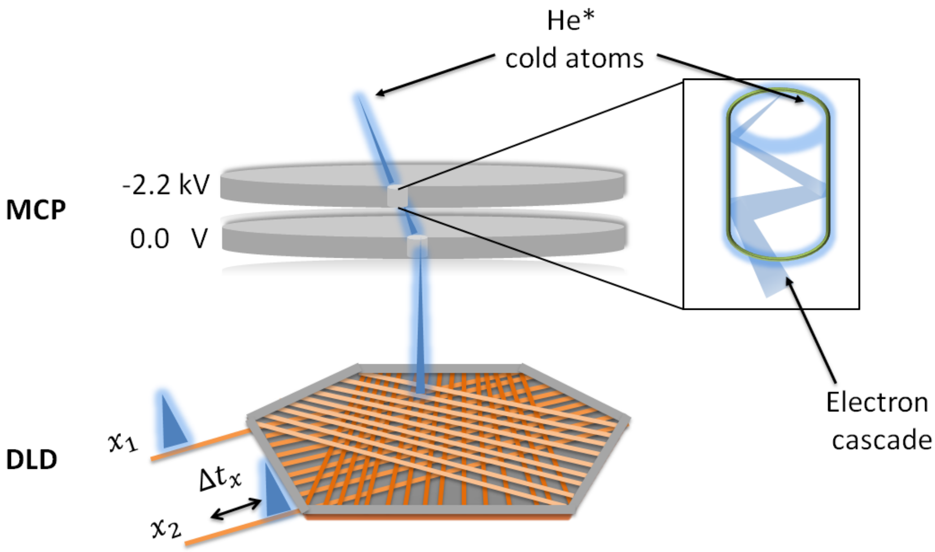

Figure 1.6: A Multi-channel plate assembly and a hexagonal delay-line detector with three layers for redundant multi-hit detection. The DLD wires are wound at an angle of 60^o *with each other. The inset shows an electron cascade generated in one of its capillaries.*

The primary electron(s) are accelerated by the voltage applied across the plates of the MCP assembly and thus a cascade of electrons is triggered into the MCP capillaries. As a result, the shower of electrons yields a pulse of several thousand electrons, which emerge from the rear of the plate. Eventually, the individual channel produces an electric pulse with a spatial pattern at the rear plate which preserves the pattern of the atoms hitting the front surface.

Using the MCP the time of flight profile in the far field of the free fall atomic cloud can be measured by detecting the count rate of He* atoms falling onto its surface. An advantage of an MCP over absorption imaging is the ability to detect the time of flight profile of a very small signal due to the single-atom detection capabilities and low background count rate. However, absorption imaging is useful for imaging MOTs and magnetic traps, since these clouds are relatively hot and broad on the MCP detector which makes measuring their width accurately challenging. Thus temperature and the atom number of the cloud measured in this way would be an underestimate.

The output of the MCP is typically read out using a delay-line detector. The Hexanode delay line detector [1] comprises a hexagonal disc wound with three wires (see Fig. 1.6). The principle of the delay-line position readout is based on the measurement of the time difference between the arrival of the induced signal at each end of the detection wire [8]. The signal is generated by an electron cloud emitted at the location of the particle impact on the DLD, which travels along the wire. By measuring the arrival time difference, the position of the particle impact on the wire can be deduced. The spatial position of the event, corresponding to the collision of a He* atom with the detector, can be determined along the axis perpendicular to the wire winding by examining the difference in the arrival times of the signals at the x_1 and x_2 terminals of the wire. When the time difference is zero, the event occurred at the midpoint of the wire, whereas the event is located at the edge of the detector when the time difference attains its maximum possible value.

A DLD works as follows: Suppose an atom impacts a specific layer of the detector at a location denoted by u, resulting in the emission of a signal delayed by time t_0. The signal propagates along the wire at a velocity of v_u, and the time it takes to arrive at each end of the wire is expressed as:

$$\begin{aligned} x_1 &= t_0 + u/v_u \\ x_2 &= t_0 + (L-u)/v_u, \end{aligned} \tag{1.22}$$

where L is the length of the wire. The position of the atom can then be determined from

[1]For more information see: http://www.roentdek.de/info/Delay$_Line/$

the time difference between the arrival of the signal at each end of the wire:

$$u = (x_1 - x_2)v_u \tag{1.23}$$

The position u is defined in the hexagonal coordinate system, which can be transformed back into the standard xy coordinates. By measuring the arrival times of the signal at each end of the wire, the position and timing information of individual atoms can be obtained with high resolution. This information is critical in the study of cold atoms and is widely used in the research and development of advanced quantum technologies.

1.3 Metastable Helium

The superfluid state of helium isotopes and the Cooper pairs of superconductors were only known to exhibit BEC prior to 1995. Afterward, condensation was accomplished in weakly interacting alkali gases such as rubidium, lithium, sodium, and hydrogen. A few years after, BEC using metastable helium atoms is reported.

The experimental creation of Bose-Einstein condensates of dilute weakly interacting gases of atoms [9, 10] has opened the possibility of exploring interesting phenomena of the quantum world on a macroscopic scale. Over the subsequent years, the field has exploded, with BECs now used in diverse fields of quantum science, including quantum many-body systems [11], topological physics [12], and precision inertial measurements [13]. The precise manipulation of inter-particle interactions [14, 15] provides a tool for investigating the dynamics of the strongly interacting regimes [16] and higher-order correlation functions. While BEC experiments were initially limited to observing collective properties of the ensemble, a number of more recent detection techniques allow for the detection of individual atoms [17], opening up a broad new range of experimental possibilities. In experiments involving alkali or rare earth atoms, such single atom detection is usually performed via high-resolution fluorescence imaging, either in-situ in optical lattices [18, 19] or after expansion from a trap [20, 21]. However, such techniques usually have limitations on their spatial extent and the atom number able to be imaged.

Achieving Bose-Einstein condensation in helium atoms was challenging since a far UV light source is required for manipulation of their ground state. Unlike alkali gases, metastable helium (He*) BEC was realized in its metastable triplet state 2^3S_1 rather than the ground state. Typical atomic state lifetimes are on the order of nano-seconds, whereas for the first excited state of helium 2^3S_1 decay is forbidden by quantum mechanical selection rules, which leads to a metastable state with lifetime (7900 s for Helium) much longer than typical experimental times scales. The main feature is based on their large internal energy (several eV compared to about 10^{-10} eV of kinetic energy in a BEC). This energy can be used to release a cascade of electrons when hitting the detector surface. The high internal energy is very efficient for the direct detection of individual atoms with full 3D temporal and spatial resolution using electronic detectors such as multi-channel plates and delay-line detectors (MCP-DLD) [22].

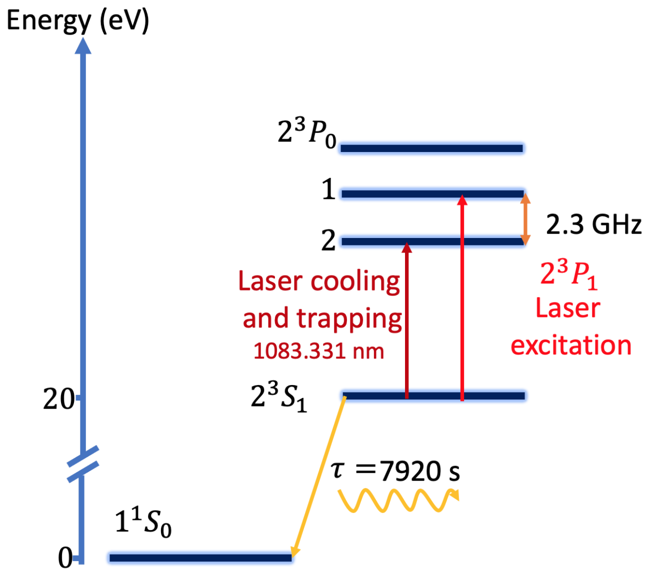

Figure 1.7: Energy levels diagram of ^4He. The triplet 2^3S_1 metastable state is an effective ground state where the condensation occurs. For cooling and trapping the ($2^3S_1 \rightarrow 2^3P_2$) transition at 1083 nm is used.

This opens the possibility of new experimental studies, that can not be realized with alkaline atoms such as allowing quantum-optics equivalent demonstrations with atoms of iconic experiments such as the Hanbury Brown-Twiss (HBT) effect [23], Wheeler's delayed choice [24], the Hong-Ou-Mandel effect [25], ghost imaging [26] and the measurement of Bell correlations [27]. The simple electronic structure of the Helium atom offers another advantage; its atomic structure can be calculated with high accuracy using the ab initio technique [28]. Moreover, the nuclear spin of ^{4}He is zero and thus the atomic structure does not show a hyperfine structure as shown in Fig. 1.7.

A drawback of the large internal energy of the metastable atoms is the losses due to the ionization process of the colliding particles. Two Helium atoms in the metastable state have a high probability to undergo *penning ionization* [29], which can be described by the following equation:

$$\begin{aligned} He^* + He^* &\rightarrow He + He^+ + e^- \\ &\rightarrow He_2^+ + e^- \end{aligned}$$

with collision rate of the order of 10^{10} $cm^3 s^{-1}$ [30], which may prevent the realization of the degenerate state with high atomic density. However, it is found that the penning ionization is suppressed four orders of magnitude for the spin-polarized cloud of He* [31], due to the conservation of electronic spin between the input ad the output channels.

In this thesis work, we present the construction and optimization of a new experimental setup allowing the rapid realization of He* BEC using an optical dipole trap. The dipole force caused by far-detuned laser beams allows the creation of optical potentials for neutral atoms. An optical dipole trap provides an elegant approach to trapping atomic gases. Owing to its small volume a significant increase in the atomic phase space density is observed. With sufficient initial trap depth, the atomic cloud is transferred directly to the optical dipole trap where the cloud is cooled further evaporatively. These trapping potentials have several advantages over common magnetic traps.

Unlike the magnetic traps, in optical potentials atoms are trapped regardless of their spin state, which offers the possibility to investigate spin mixture states. Another possible implementation for optical potentials is controlling the geometry and the dimensionality of the trap, which allows for exploring physics in low spatial dimensions. Much experimental research has been conducted on the novel phenomena that occur from the strong confinement of a quantum gas [32, 33, 34]. It is reported that collision rates are strongly dependent on the dimension of the trap [35, 36, 37]. The tight traps provided by dipole traps can overcome the slow thermalization rate in magnetic traps [38, 39, 40, 41, 42], either in a hybrid combination with a magnetic trap [43] or in a stand-alone cross beam configuration [44] and hence shorter experimental sequence is possible. Confining He* atoms in a cross-optical dipole trap at $\lambda = 1550$ nm allows the preparation of interesting quantum Hamiltonian such as quantum quenching which opens the possibility to study the dynamics of correlated states in different spatial dimensions since it is easy to change its spatial shape.

1.4 Laser source

All detunings for laser cooling and imaging in this work are relative to the $2^3S_1 \rightarrow 2^3P_2$ transition (1083), with a negative sign indicating red detuning. The laser cooling and imaging beams are sourced from a home-built external gain-chip laser [45] which operates with a locked linewidth below 100kHz [45]. The laser source for our experimental setup is depicted in Fig. 1.8 (this diagram is adapted from D. Shin, Ph.D. thesis [46].). The output of the cavity passes through an in-fiber beamsplitter, from which one output is blue-shifted using an acoustic-optical modulator (AOM) by 253 MHz and directed to a helium gas cell for saturation absorption spectroscopy. The remaining output arm is coupled by optical fibers to a fiber amplifier that produces up to 5 Watts of laser power from the $\sim$ 3 mW supplied by the cavity.

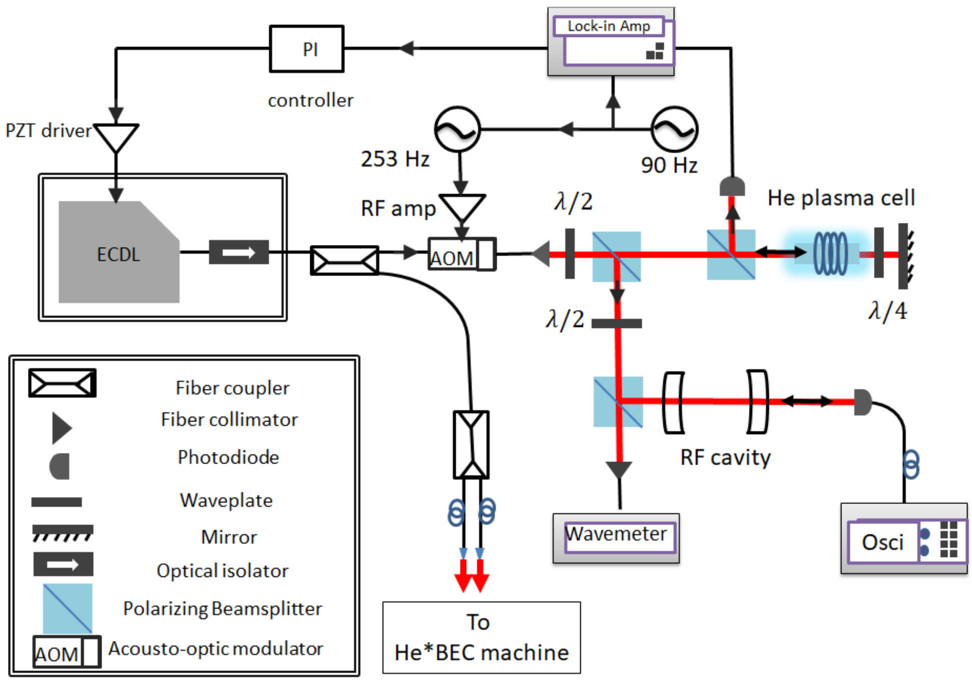

Figure 1.8: This diagram shows the generation of a cooling laser operating at 1083.331 nm. The laser cavity filters the resonant light, which is then split by an in-fiber beamsplitter. The output is sent to the experiment, while the remaining part passes through an in-fiber AOM to the saturated-absorption spectroscopy system. The offset is modulated at 90 kHz and generates a demodulated signal that serves as the error signal for a PID controller. The controller feeds back to the frequency-selective diffraction grating's piezoelectric actuator to minimize the gradient of the signal at the absorption peak.

The light is distributed to the laser cooling and trapping chambers. Individual frequency shifts are provided by acousto-optic modulators in each beam, which independently control its power and frequency. For this purpose, each AOM is supplied by a half-waveplate and beamsplitter. The order of the diffraction pattern is tweaked for highly efficient transmission. The AOMs are set up in a double-pass configuration and a quarter-wave plate introduced in the optical path through the doubly-diffracted beams is transmitted back through the beamsplitter into the distribution optics. However, we use electronic shutters to reduce the risk of stray light interacting with atoms.

In the next chapter, I will present the general layout and the specifications of our experiment setup.

This page intentionally left blank.

Chapter 2

Rapid generation of He* BEC

MANY of the possible exciting experiments with ultracold He* require measuring correlation functions, often to higher orders, which necessitates large amounts of data. For this purpose, a shorter experimental sequence is required to shorten the data acquisition time. The slow thermalization rate in the relatively weak magnetic traps commonly employed in He* experiments constrains the length of the experimental sequence. However, this can be circumvented in the tight trap provided by an optical dipole potential. The present chapter outlines the infrastructure of our experimental setup, where we use such a trap to produce BECs of He* atoms in a short sequence.

This chapter supplements work that has previously been published in:

- [47]:- A. H. Abbas, X. Meng, R.S. Patil, J. Ross, A.G. Truscott, and S.S. Hodgman, Rapid generation of metastable helium Bose-Einstein condensates. Phys. Rev. A 103, 053317 (2021).

Author contribution

This section elaborates on the author's contribution to the development and optimization of a new science chamber for creating a He* BEC in a cross-optical dipole trap [47].

Initially, the lattice machine was an upgraded version of a pre-existing machine that was used for the study of dual-species He*-Rb MOT experiments. Dr. S. S. Hodgman and some students began by fixing the discharge source and pumping down the existing chamber to low pressure of 10^{-10} Torr. Additionally, the cooling and trapping beams were already in place. However, the existing chamber had small ports that could not accommodate the expanding lattice.

The previous version of the machine consisted of a source chamber and a Zeeman slower that terminated at a MOT chamber, as well as a secondary science chamber. In the upgraded version, the author and the team designed a simple QUIC trap that is inserted inside the science chamber, allowing for better control and optimization of experimental parameters. Moreover, the control sequence was optimized for the atom number and the temperature of the cloud at different stages. This optimization included tuning experimental parameters to trap a decent fraction of atoms in the second MOT, magnetic trap, and optical dipole trap. Laser beams had to be re-aligned based on the new location of the magnetic trap, and the cross-optical dipole trap was built and re-aligned.

The author and the team reconstructed the new science chamber includes a detector chamber (MCP-DLD stack) and an imaging system for the new magneto-optical, magnetic, and optical traps, addressing the limitations of the previous version and expanding its capabilities.

2.1 Apparatus upgrade

Quantum simulation using He* BEC into an optical lattice potential is the long-term goal of our experimental setup (*lattice machine).* He* BEC is first realized at ANU in a bi-planar quadrupole Ioffe configuration (BiQUIC) magnetic trap [41]. Due to insufficient optical access to the BEC chamber of the BiQUIC machine, building optical lattice potential was a challenge. The lattice machine is an upgraded version of a pre-existing machine used for the study of dual-species He*-Rb MOT experiments [48], electron scattering [49] and the electronic transition rates in He* [50]. It comprised a DC source chamber, a Zeeman slower that ends at a first MOT chamber, and a secondary science chamber with relatively small ports with limited optical access, and an upgrade was required to allow adding several trapping beams for the purpose of loading He* BEC into an optical lattice. The pre-existing machine has a large magnetic coil, which has a long switch-off time.

In the upgraded version, we designed a new QUIC trap that allows fast switching-off time with good optical access, which permits the building of an optical lattice. Furthermore, an MCP-DLD stack and an imaging system will also be included in the new setup.

2.2 Fast Data Acquisition

Quantum many-body phenomena arise from the quantum statistics of particles, which can be quantified by correlation functions. These functions describe how microscopic parameters such as local density at two different points in space or time are related. The type of correlation is identified by the order of the correlation function. For instance, the correlation function of the first order is highly sensitive to phase fluctuations and describes correlations in the fringes formed in a double-slit experiment. The second-order correlation function is used to differentiate between different types of sources (incoherent fermions, thermal bosons, and coherent bosons). Such correlation functions require large amounts of data, especially if higher-order correlations are being measured [51, 52], often needing 10,000-100,000 individual experimental runs for a single experiment. This has led to constant improvements across generations of experimental He* apparatuses aiming for ever shorter experimental sequences.

Most He* BEC experiments [38, 39, 40, 41, 42] use magnetic traps, where the sequence length is limited by the slow thermalization rates in magnetic traps that have relatively weak trap frequencies. The tight traps provided by dipole traps can overcome this, either in a hybrid combination with a magnetic trap [43] or in a stand-alone cross-beam configuration [44]. However, due to the limited depth of the dipole trap, to enable an efficient transfer the atoms need to first be cooled, either optically via complex additional cooling schemes such as grey molasses and/or evaporatively in a magnetic trap [44]. Here, we present a simplified experimental scheme to generate BEC using helium atoms by direct evaporative cooling in a crossed-beam optical dipole trap. The length of the experimental sequence is reduced to half of the previously reported work [44].

The experimental apparatus

Experimental realization of He* BEC starts with exciting Helium atoms to the 2^3S_1 metastable state which can be produced by a cryogenically cooled DC discharge source. The velocity of the atomic beam is then slowed down to a few tens of ms^{-1} using a Zeeman slower before it is captured in our first MOT. Finally, a MOT with several hundred million atoms is loaded in the science chamber where the BEC is formed in a cross-optical dipole trap. The physical parameters such as temperature T and the number of atoms N are determined using an optical detection method (absorption imaging) and an electronic method (MCP) [47]. The general layout of our experiment is comprised of four main stages, which are sketched in Fig. 2.1. In the following sections, I will now explain each of these stages in more detail.

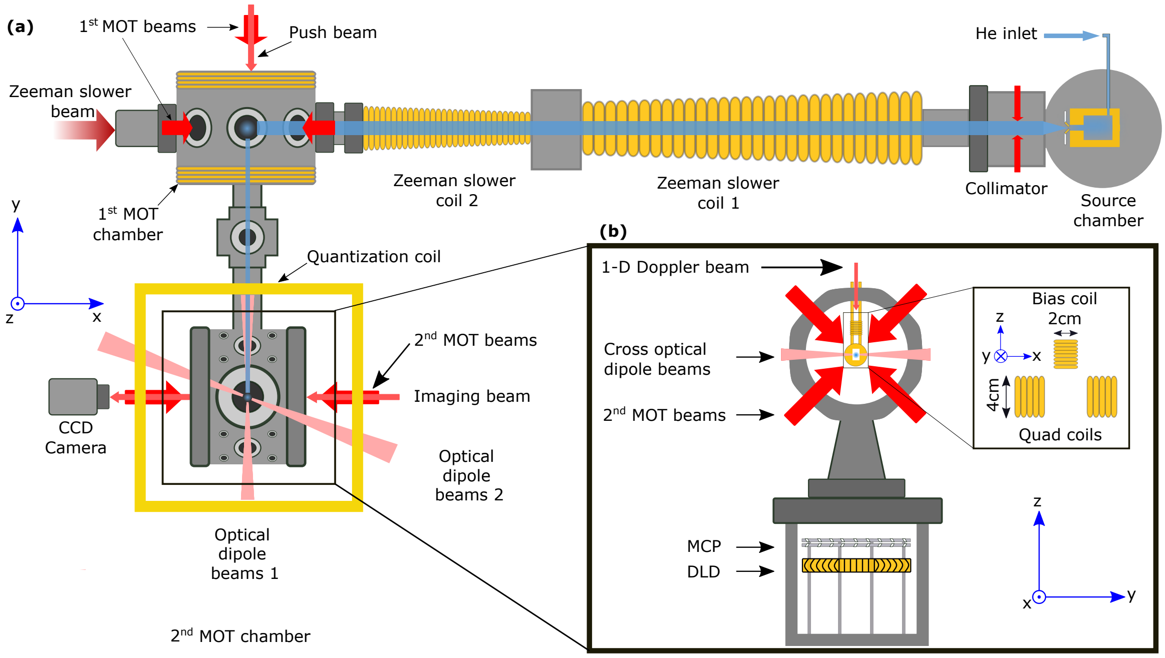

Figure 2.1: Schematic of the experimental apparatus (see main text for details). (a) Top view of the experimental setup. A beam of He atoms is produced in a cryogenically liquid nitrogen-cooled source, before being optically collimated, slowed, and cooled in the 1^{st} MOT stage. This forms a source for the 2^{nd} MOT, where the atoms are then transferred to a magnetic trap and subsequently to an optical dipole trap, where the BEC is generated. (b) Side view of the 2^{nd} MOT chamber, showing the quadrupole-Ioffe configuration in-vacuum trap and MCP-DLD detector. The inset shows the trapping coil geometry from a different angle.*

Figure 2.2 illustrates the control system and laser beam distribution on the optical table. The output of a fiber amplifier is split across multiple AOMs, with their power regulated by a combination of half-wave plates and a polarizing beamsplitter. The first diffracted order is then directed to the atomic beam flux by reflecting it back through a quarter-wave plate and an aperture. The properties (i.e power and detuning) of each beam will be described in detail in the following text.

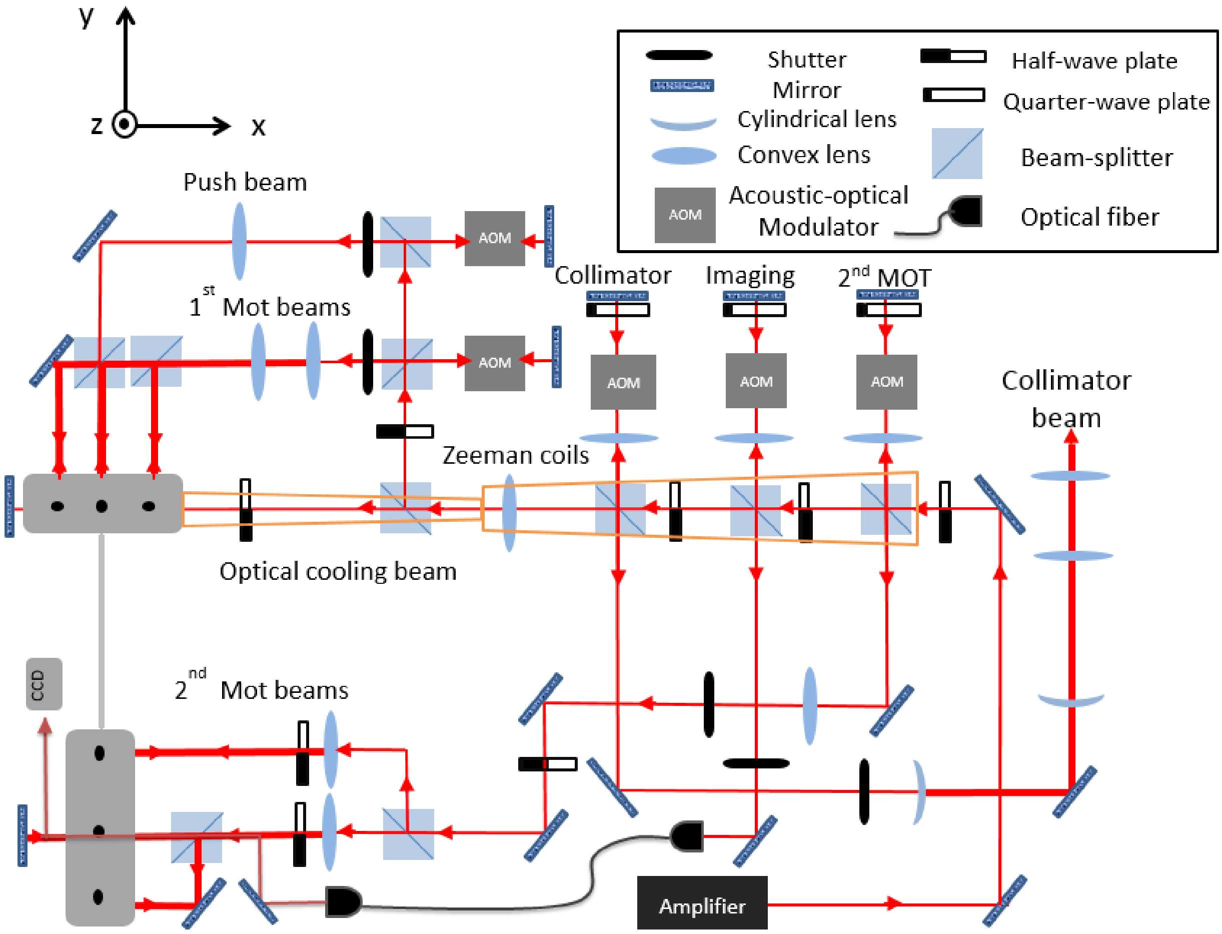

Figure 2.2: Schematic diagram describes the system for controlling and distributing cooling light in a lattice machine. The light is supplied by a fiber amplifier to several AOMs. The power to each AOM is controlled by half-wave plates and polarizing beam splitters. The first diffracted mode is selected by an aperture, and a quarter-wave plate before the light is transmitted through a beamsplitter and sent to the optics. Finally, the light is inserted into the vacuum chamber and used to achieve BEC.

2.3 Helium Beam line

2.3.1 He* atom source

The metastable state of Helium is created in a custom-built cryogenically cooled DC discharge chamber, shown schematically in Fig. 2.3. The source is composed of a grounded hollow copper block [53], where the discharging occurs, cryogenically cooled by liquid nitrogen which serves as a cathode. A tungsten anode is placed in front of the open side of the copper block, separated by an electrically insulating (but thermally conductive) boron nitride disc with a small hole in the front face. A pulse of $\sim$ 5 kV voltage is required to ignite the source and excite the He atoms, although is reduced to 2.5 kV during operation.

The DC discharge source produces a high atomic flux with only 0.01 % of the atoms into the He* state. A high-speed turbomolecular pump connected to the source chamber maintains a pressure of low 10^{-5} mbar when the source operates. The atomic beam emerges with a small solid angle from an outlet nozzle in the front of the copper cathode, which then passes through a small hole in a skimmer into an evacuated region converting thermal energy into kinetic energy. The emerging beam has a longitudinal velocity that is of the order of 1000 ms^{-1} and transverse velocities of the order of $\sim$ 60 ms^{-1}, causing a divergence of the beam in the transverse axis.

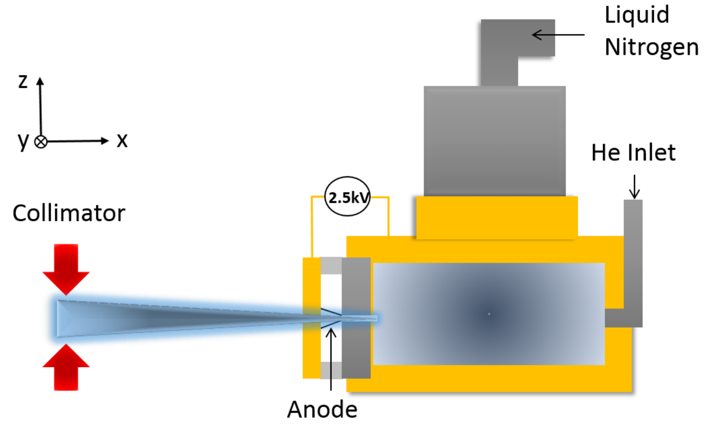

Figure 2.3: A beam of He atoms is produced in a hollow copper cathode, which is cooled cryogenically by liquid nitrogen. The atomic flux emerges from a small hole into an evacuated region where it is optically collimated.*

The expanding atomic beam is then collimated using an optical collimation stage, which reduces the divergence of the flux transversely and thus enhances the atomic flux in the longitudinal axis per solid angle. The collimation stage is achieved by multiple reflections of a single laser beam, which allows cooling in the two transverse directions [41]. The collimator beam has an intensity $\sim 67I_{sat}$ (I_{sat} = 0.167 mW/cm^2) and is detuned by $\sim -5\Gamma$ ($\Gamma/2\pi$ = 1.63MHz) from resonance. The laser beam is red detuned from the transition $2^3S_1 \rightarrow 2^3P_2$ and therefore only affects atoms in the metastable state. Before entering the chamber, the laser beam is elongated ($\sim$ 5 cm at the source position) along the axis parallel to the helium flux using a cylindrical lens, which in turn extends the interaction time between the fast atoms and the light.

At this stage, the emerging flux is a mixture of different energy states. In order to slow the He* atoms further to enable capture by the first MOT stage, a beam of $\sim 92\ I_{sat}$ intensity and $\sim -160\Gamma$ detuning, is aligned counter-propagating with the direction of the atomic beam. The radiation pressure only affects He*, which will scatter photons and be collimated, hence the He* flux is increased in the center of the beam. However, due to the Doppler shift, the atomic transition is shifted and the cooling process is terminated. To ensure the atom continues absorption of light and therefore effective cooling, a spatially varying magnetic field is implemented to compensate for the induced Doppler shift. This has been done in different ways, but here we will be focusing on the Zeeman slowing approach.

2.3.2 Zeeman slower

The Zeeman slowing technique was developed to deal with the velocity-induced Doppler shift in laser cooling [54]. In our experiment, a Zeeman slower stage is required to reduce the collimated atomic beam velocity to the point where it can be captured by the magneto-optical traps located at the end of the slower. An atom moving towards a laser beam will have its electronic levels shifted by the Doppler effect, which means that as atoms are slowed, they will no longer be at resonance, which stops the cooling process. A spatial dependant magnetic field $B(z)$ can be implemented to compensate for this shift via the Zeeman effect and brings the atom back into resonance with the laser beam, see Fig. 2.4. For an appropriate Zeeman shift, the resonance condition can be restored such that

$$\omega_L + kv = \omega_0 + (g_p m_{J_p} - g_s m_{J_s})\mu_B B(z)/\hbar, \tag{2.1}$$

where $g_P = 3/2$ is the Lande factors of 2^3P_2 excited state with magnetic moment $m_{J_p} = 2$ and $g_s = 2$ is the Lande factors of 2^3S_1 metastable triplet state with magnetic moment $m_{J_s} = 1$. The Zeeman shift $\mu_B B(z)/\hbar$ on the right-hand side should compensate for the Doppler shift on the other side kv. Thus an atom with velocity v_i will reach a position z where the resonance condition (2.1) is fulfilled and the matching between the laser frequency and the atomic transition frequency is restored.

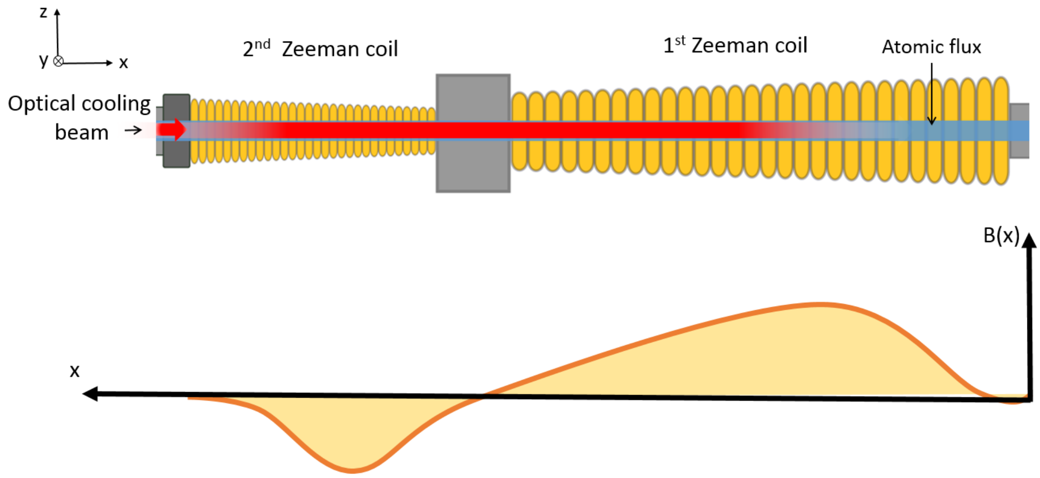

Figure 2.4: The double coil Zeeman slower configuration used in our setup, and the associated magnetic field profile B(z) along the direction of propagation (z) of the atoms.

In our setup, a Zeeman slower is employed to reduce the velocity of the atoms to < 100 m/s, featuring a σ_- laser beam of ~ 92 I_{sat} intensity and $\sim 160\Gamma$ detuning, counter-propagating with the direction of the atomic beam. A spatially varying field to keep the atoms on resonance while they slow down is generated by two separate coils with variable windings along their length and a zero field in the center. This double-coil Zeeman configuration has been designed to circumvent the degeneracy of the two transitions $2^3S_1, m_J = +1 \rightarrow 2^3P_2, m_J = +2$, and $2^3S_1, m_J = +1 \rightarrow 2^3P_1, m_J = 0$ occurring for a 600 G field, which would be required for a single coil Zeeman slower [55].

The magnetic field profile $B(z)$ along the direction of propagation of the atoms is determined by the longitudinal velocity of the atoms into the Zeeman slower and can be achieved by multiple coils of gradually decreasing radii.
The associated magnetic field profile of one Zeeman coil can be expressed as [55]

$$B(z) = B_0\sqrt{(1 - \frac{2a_{max}}{v_0^2})z} + B_{bias}, \tag{2.2}$$

where B_0 is the field value at the beginning of the slower for which an atom with velocity v_0 is resonant with the laser detuning δ. The minimum length of the Zeeman slower is set by the maximum possible deceleration, a_{max}, achieved when the atom is in resonance with the high-intensity laser beam, which is given by

$$a_{max} = \frac{\hbar k\Gamma}{2m}. \tag{2.3}$$

The magneto-optic trap (MOT) is located at the end of the Zeeman slower, which represents a challenge since the magnetic field of the solenoid extends beyond the end of the slower and does not vanish abruptly, and a small stray field will affect the trapping field of the MOT. To overcome this, a compensation coil "anti-phase coil" is introduced to ensure a zero field at the end of the second Zeeman coil [53]. Furthermore, the Zeeman slowing laser beam is aligned along the horizontal axis of the MOT region and hence it passes through the atomic cloud, which is trapped in the center of the MOT where the magnetic field is zero. Therefore, this beam needs to be detuned carefully, otherwise, the slowing laser will exert a scattering force on the atoms in the MOT and push them out of the trap. An atomic flux of $\sim$ 2.5 nA ($\sim 4 \times 10^9$ atoms/sec) is measured at the end of the first Zeeman slower using a Faraday cup on a rotation stage and a pico ammeter. The second Zeeman slower has been built in order to reduce the longitudinal velocity of the beam to $\sim 70\ ms^{-1}$, which is within the capture velocity of our first magneto-optical trap.

2.3.3 First magneto-optical trap

The slowed atomic beam is then trapped and cooled by our first MOT, with the three counter-propagating red-detuned MOT beams with a diameter of $\sim$ 40 mm having $\sim$ 87 I_{sat} intensity (horizontal beam), 140 and 110 I_{sat} intensity (vertical beams). The detuning of all the beams is set to $\sim -22\ \Gamma$, which is relatively large to mitigate losses due to Penning ionization [56]. They are circularly polarized σ_+ and σ_- so that a restoring force is created along each axis, which creates a restoring force on the atoms toward the trap center.

The quadrupole magnetic field is generated by two coils mounted on the front window as shown in Fig. 2.5. However, the degenerate state cannot be achieved in this chamber since the atomic beam flux contains unexcited helium atoms in addition to the He*, which increases the background pressure in this chamber (of order 10^{-9} torr), and a long-lived magnetic trap cannot be maintained. Thus, the first MOT serves as a secondary source of a cold helium beam, which is then directed to the science chamber for the final trapping stages.

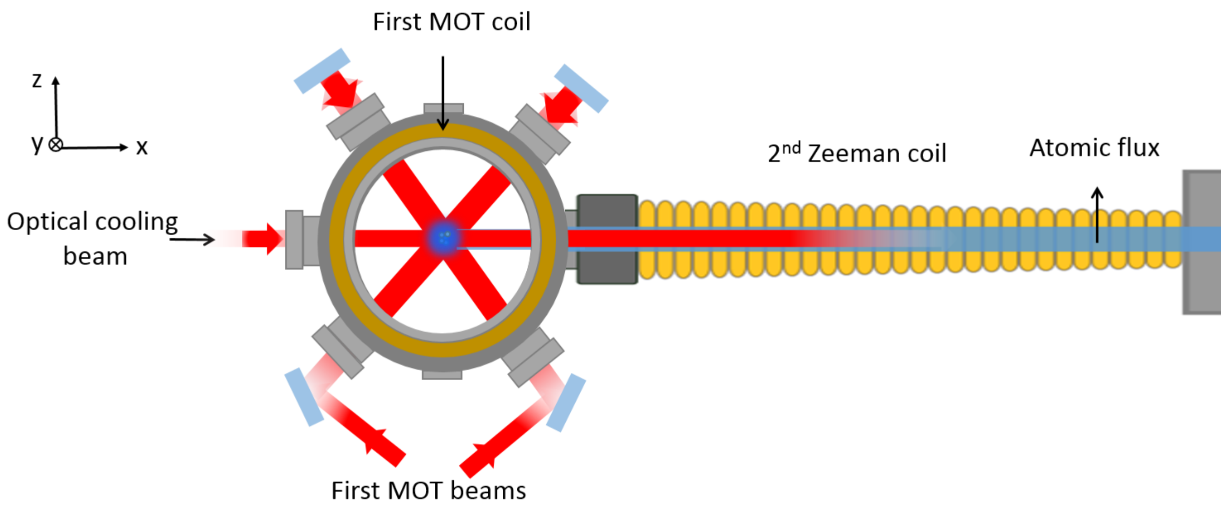

Figure 2.5: The first Magneto-optical trap with three counter-propagating pairs of laser beams intersecting at the trap center which is created by a pair of coils with opposing currents (anti-Helmholtz coils). The slowed atomic beam is captured by the first MOT, which is located at the end of the second Zeeman slower stage.

The horizontal MOT retro mirror located inside the vacuum chamber features a ~ 1.5 mm diameter hole in the center, which enables atoms to leak out of the MOT and into the UHV 2^{nd} MOT chamber, where the pressure is $< 5 \times 10^{-11}$ Torr. To assist this process, an additional "push" beam is added ($\sim 110\ I_{sat}$ intensity and $\sim 3.3\Gamma$ blue detuned) is used to push atoms through the aperture of the first MOT retro-mirror into the second MOT, forming a low-velocity intense source scheme (LVIS) [41]. At this stage, a flux of ~ 70 pA from the LVIS, which corresponds to $\sim 9 \times 10^{8}$ atoms/s, is measured using a Faraday cup on a rotation stage and a pico ammeter, which exists ~ 10 cm beyond the location of the 2^{nd} MOT.

2.4 Science chamber

Typically, The temperature achieved in a MOT is of order several hundreds of μK. In order to decrease the temperature further and thus increase the phase-space density (PSD), the atomic cloud is transferred into the conservative potential of a magnetic trap. A number of magnetic trap designs are used in BEC experiments, with some commonly used ones including the cloverleaf design [57], the Quadruple-Ioffe configuration (QUIC) trap [58] and atomic chip traps [59]. Any design has strengths and weaknesses, and inevitably involves compromises and trade-offs between factors such as confinement, depth, stability, switch-off time, physical size, current required, and heat dissipation.

In our magnetic trap setup, no evaporation is implemented; we only perform 1D Doppler cooling in the trap. Hence we require a large enough bias to split the atomic energy levels (as well as prevent Majorana and Penning losses) but are not so concerned about the usual consideration of having tight confinement, as all evaporation is conducted in the dipole trap.

2.4.1 In-vacuum magnetic trap

Based on the Zeeman effect, the magnetic trap is used to confine an atom with magnetic moment μ placed in an external magnetic field B. This atom will experience a force $F = -\nabla U(r)$, where $U(r)$ is the potential energy and is given by

$$U(r) = -\mu B(r) cos(\theta),$$

with θ is the angle between the magnetic moment vector $\overrightarrow{\mu}$ and the magnetic field vector $\overrightarrow{B}$. The projection of the magnetic moment along the magnetic field vector is given by $\mu = -g m_J \mu_B$, with g the Lande vector, μ_B the Bohr magneton and m_J the magnetic substate. According to the sign of the magnetic substate (m_J), the atom is either attracted or repelled from the magnetic trap minimum at the trap center. Therefore, atoms with $m_J > 0$ are attracted toward the trap center and known as low-field seekers. In contrast, the atoms with $m_J < 0$ states are repelled away from the trap origin. The magnetic trap does not affect the state with $m_J = 0$. For He*, the triplet state 2^3S_1, $m_J = +1$ will be confined and therefore trapped at the minimum of the magnetic trap, while the other two states $m_J = 0$ and -1 will be untrapped and anti-trapped, respectively.

The quadrupole trap (Quad trap) is provided by two coils in an anti-helmotz configuration. This quad trap has a singular point at the center where the field is zero. At sufficiently low temperatures, the low-field seekers are able to escape such a trap from the trap bottom (Zero-field point). This is because atoms change state between the different sub-levels when they are all degenerate at (spin-flip) at the zero-field point, which is known as Majorana spin-flip [60], and as a result atom losses. This can be circumvented by using a magnetic trap in the Ioffe Pritchard configuration [57], in which an addition coil perpendicular to the anti-Helmholtz coils known as the bias coil, generates an extra field component along the axis of symmetry and thus shifts the bottom of the magnetic field upward. This configuration is known as a Quadrupole Ioffe Configuration or QUIC trap.

In our experimental setup, the magnetic trap is in a simple QUIC configuration, consisting of two 5-turn anti-Helmhotz (AH) coils of 40 mm diameter centered on the y axis and an 8-turn bias coil of 20 mm diameter centered on the z axis, as shown in Fig. 2.6. These coils are made from 2 mm hollow copper tubing (internal diameter 0.4 mm) mounted in-vacuum to ensure they are close to the atoms. Cooling is provided by pumping chilled water through the tubes, with each tube attached to hollowed-out 1/4 inch feed-throughs sealed with vacuum-compatible solder.

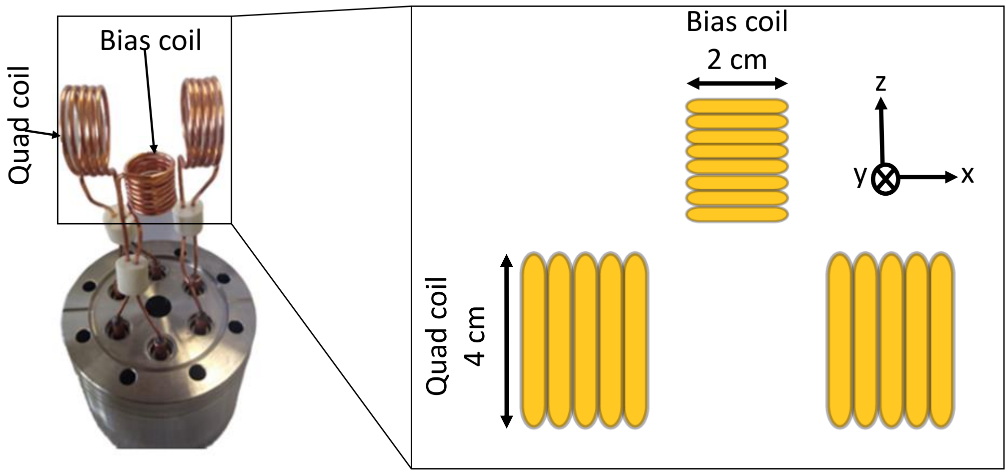

Figure 2.6: New geometry of QUIC trap used in our setup. Five-turn Quad coils configuration centered on the x axis and an eight-turn bias coil centered on the z axis. These coils are made from 2 mm hollow copper tubing, mounted in-vacuum to ensure they are close to the atoms. Cooling is provided by pumping chilled water through the tubes.

The trapping potential in cylindrical coordinates can be approximated near the center by $U(r,z) = U_0 + \frac{1}{2}m(\omega_\perp^2 r^2 + \omega_z^2 z^2)$, with the radial and axial trap frequencies are $\omega_{\perp(=x(y))}$ and ω_z respectively. These coils are used to generate the quadruple trap for the second MOT and the magnetic field gradient for the magnetic trap.

2.4.2 Second magneto-optical trap

Our second MOT consists of a quadrupole magnetic field generated by our in-vacuum AH coils with a gradient along the tight axis of $B' \sim 4.4$G/cm, along with three pairs of counter-propagating laser beams (see Fig. 2.7) with detunings $\Delta \sim -33\Gamma$ and intensities of $\sim 140\ I_{sat}$, $\sim 37\ I_{sat}$ and $\sim 400\ I_{sat}$. In 1s we load a cloud with $\sim 1.7 \times 10^8$ atoms at a temperature of ~ 2.5mK. The atom number is measured using saturated fluorescence on an InGaAs photodiode [41].

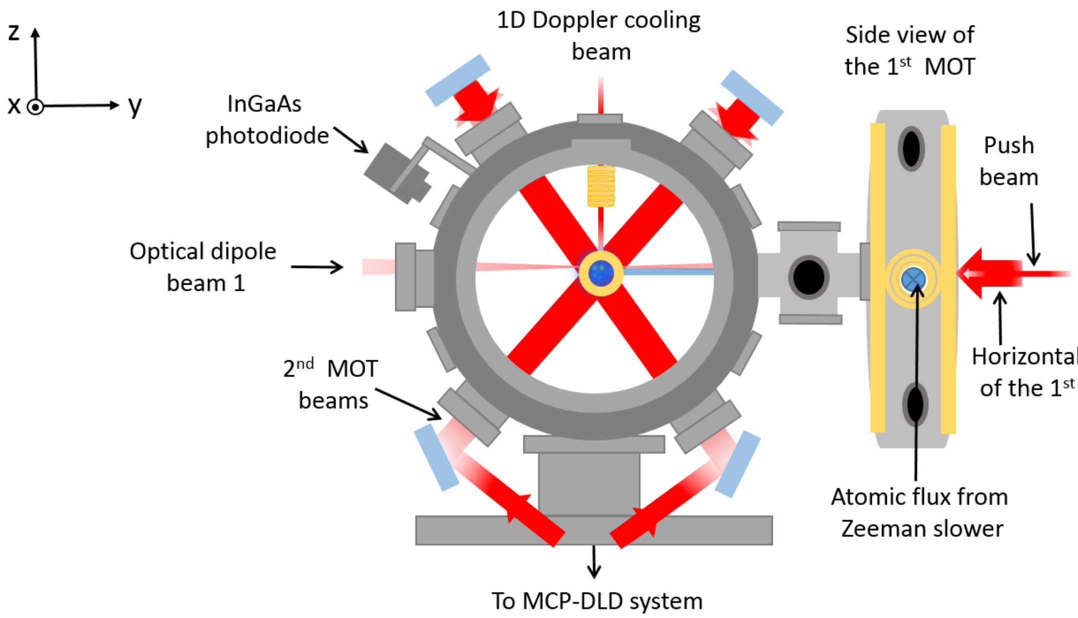

Figure 2.7: A sketch of the second MOT setup. Three pairs of retro-reflected laser beams cross each other in the center of the trap where the atomic cloud is collected and trapped. The quadrupole magnetic field is provided by our in-vacuum AH coils (shown in yellow). The saturated fluorescence signal is captured by an InGaAs photodiode mounted on one of the chamber ports.

To measure the temperature we switch off the MOT beams and the quadrupole magnetic field and allow the atoms to fall ~ 451 mm onto a detector comprising an 80mm diameter stacked pair of MCP. By using pick-off electronics we extract a signal pulse from the charge depletion of the plates that each atom causes. For a hot cloud, only a fraction of the atoms will hit the MCP because the cloud will have expanded beyond the MCP diameter during TOF. After fast amplification and discrimination of the pulses, they are recorded using a digital counter, which provides an integrated 1D TOF distribution of the atoms.

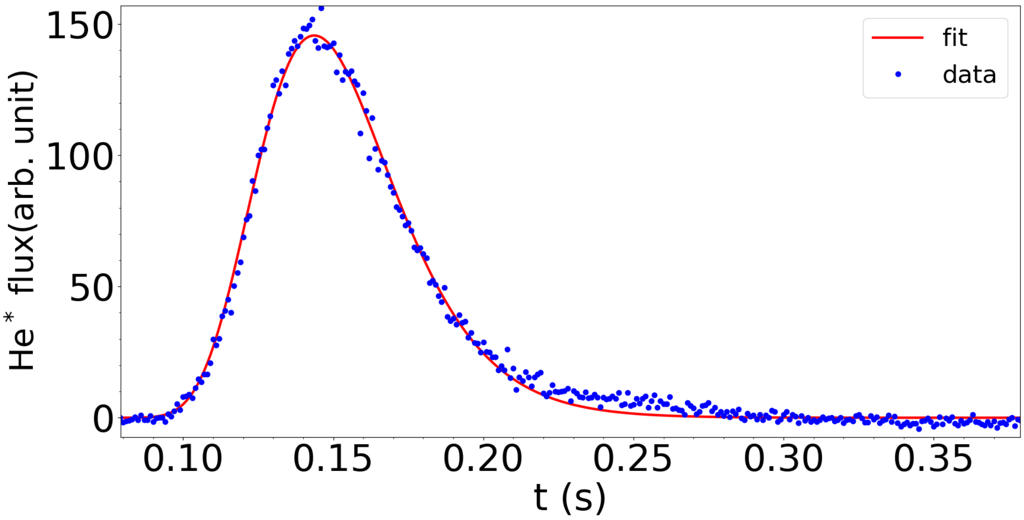

Figure 2.8: Time-of-flight signal of the MOT recorded on the MCP. The red-solid line represents the fitting using the analytic model from equation (2.4), for a temperature $T = 2.5\ mK$ of the MOT.

To model the experimental data, the cloud is initially assumed to be point-like. For a thermal cloud $T > T_c$, the TOF distribution is fitted to a Maxwell-Boltzmann distribution, given by [61, 41]

$$n(t) = A v_0^2 \pi \left(\frac{(gt^2/2 + l_0)}{t^2} \right) \exp \left(- \frac{(gt^2/2 - l_0)^2}{v_0^2 t^2} \right) \tag{2.4}$$

where $A = (m/2\pi kT)^{3/2}$, $v_0 = \sqrt{(2kT/m)}$, m is the mass of a ^{4}He atom, k is Boltzmann's constant and l_0 is the fall distance. From this distribution, we extract the temperature T, with the only other free fit parameter being the amplitude A. Fig. 2.8 shows the time of flight signal trace taken from the MCP after the MOT loading is switched off and atoms are allowed to fall onto the detector. The best fit was found for a temperature $T = 2.5$ mK, and the number of atoms $N \sim 2 \times 10^8$ as estimated by saturated fluorescence on an InGaAs photodiode.

2.4.3 Loading of the magnetic trap

Following loading, the MOT is then compressed by ramping the magnetic field down to 1.4G/cm in 10ms, while simultaneously the laser detuning is ramped up to $\Delta \sim -0.4\Gamma$ and the intensity of the MOT beams are reduced by two orders of magnitude. The MOT beams are then switched off and the atoms in the $m_J = +1$ state remain trapped in the quadrupole magnetic field of the AH coils.

To increase the trap depth and atom density we tighten the quadrupole field to 16.6G/cm in 100μs. The bias coil current is then ramped up in 100ms to form a QUIC trap with a 10G field offset, removing the magnetic field zero in the quadrupole trap. By driving 120A through the AH coils and 62A through the bias, we are able to produce a trap of $\sim 1.6\ mK$ depth and 10G bias field (see Fig. 2.9) in the trap center, which is offset 6mm vertically along the z axis from the center of the AH coils. This configuration provides weak trapping frequencies of $\omega_r \sim 2\pi \times 89$Hz in the radial (x-y) direction and $\omega_z \sim 2\pi \times 57$Hz in the axial (z) direction.

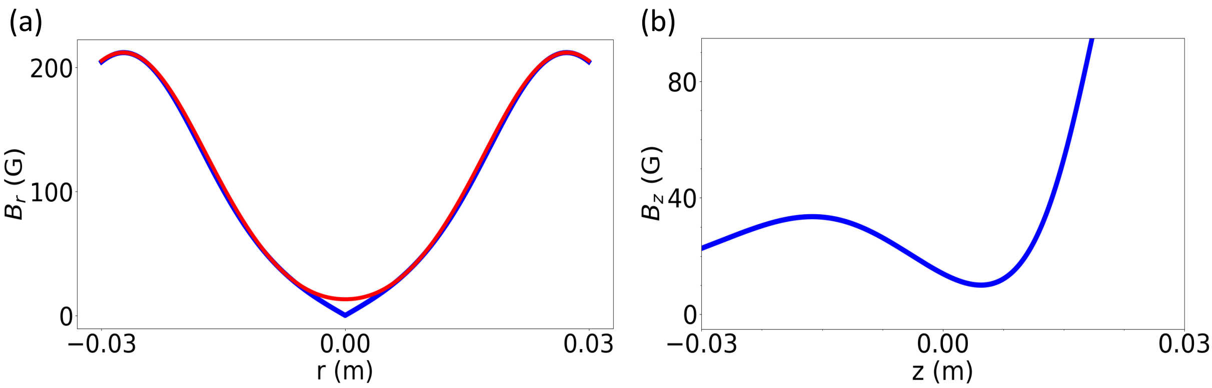

Figure 2.9: The magnetic field potential along the radial $\hat{r}$ in (a) and vertical axis $\hat{z}$ in (b) for our in-vacuum magnetic trap. (a) The blue solid line represents the quadrupole trap with zero field point at the origin. The effect of the bias coil is shown in the red solid line, which shifts the trap minimum up.(b)The trap minimum is 10 Gauss located 6 mm above the center of the quadrupole coils, while the total trap depth is ~ 25 Gauss, equivalent to 1.6 mK.

The temperature and the atom number are estimated via absorption imaging and the MCP using the time of flight measurement, as detailed below. In the next section, we analyze the TOF traces from the absorption imaging and the MCP quantitatively.

Quantitative analysis of TOF: Absorption imaging

The atom number and temperature in the magnetic trap are measured using absorption imaging, with the imaging beam along the x-axis being imaged on an InGaAs CCD camera.

Mechanical flipper mirrors allow us to swap between imaging and MOT beams on the same axis, although this prevents absorption imaging during the operation of the MOT.

The cloud is released from the trap to free fall under gravity for a fixed time interval, during which the cloud expands in all directions. For a thermal cloud, the 2D optical density profile of the expanded cloud is then fitted to a 1D-Gaussian along the vertical (y) and horizontal (x) direction respectively, with an RMS velocity $v = \sqrt{k_B T/m}$ as shown in Fig. 2.10. For a cloud of initial width σ_0, the width $\sigma_{x(y)}$ after a time of flight t is given by

$$\sigma_{x(y)}(t) = \sqrt{(\sigma_0^2 + v^2 t^2)}. \tag{2.5}$$

The in-situ image for the atomic cloud in the magnetic trap is captured via absorption imaging, in addition to absorption images for the cloud after switching off the trap for various times of flights.

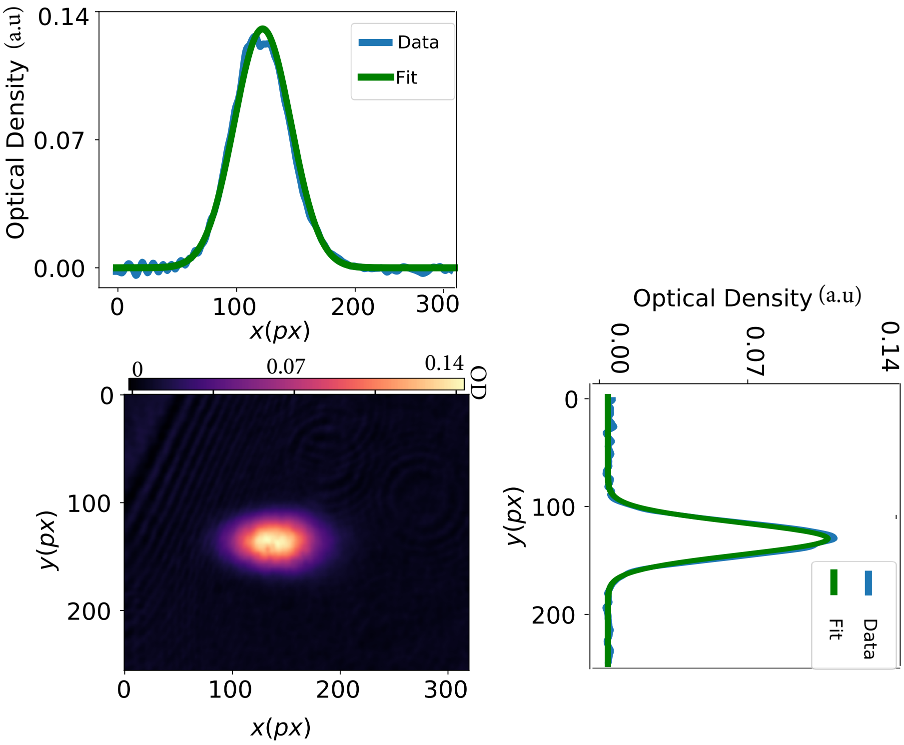

Figure 2.10: In-situ absorption image for the magnetic trap shown in Fig. 2.9 with a gaussian fit to each axis, taken by an InGaAs CCD camera ($1pixel = 20\mu m$).

The widths of the expanded clouds at a different TOF are then extracted by fitting the Gaussian optical density profile. The two Gaussian widths σ_x and σ_y are plotted versus the time of flight and thus the temperature is obtained using Eq. (2.5).

Fig. 2.11 presents the absorption images of the atomic cloud from the magnetic trap without applying the in-trap cooling stage, after different TOF. At short TOF the widths of the cloud are not uniform because the magnetic trap is relatively tight along the radial direction and weak along the axial direction.

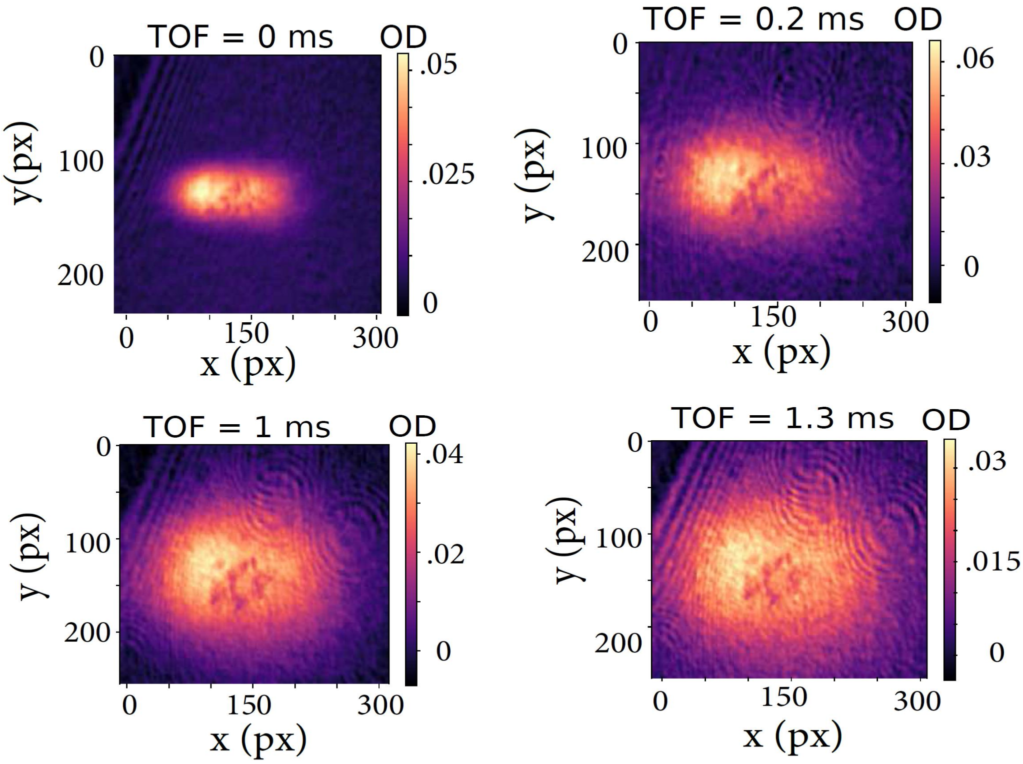

Figure 2.11: Absorption images of the atomic cloud from our magnetic trap without in-trap cooling, after a time of flight of 0, 0.2, 1, and 1.3 ms. The drop times are calculated by switching off the magnetic field.

The results for the widths σ_x and σ_y of the atomic cloud without in-trap cooling vs time of fight are shown in Fig. 2.12. The initial width of the cloud with zero time of flight (in situ) is excluded from the fitting because the image is taken while the cloud is trapped in the magnetic field and thus only a small fraction of the cloud can be imaged. Using the RMS velocities v we obtain temperatures of $\sim 747(23)\ \mu K$ and $\sim 693(73)\ \mu K$ along the vertical (z) and horizontal (r) direction of the cloud with $\sim 5.3 \times 10^7$ atoms.

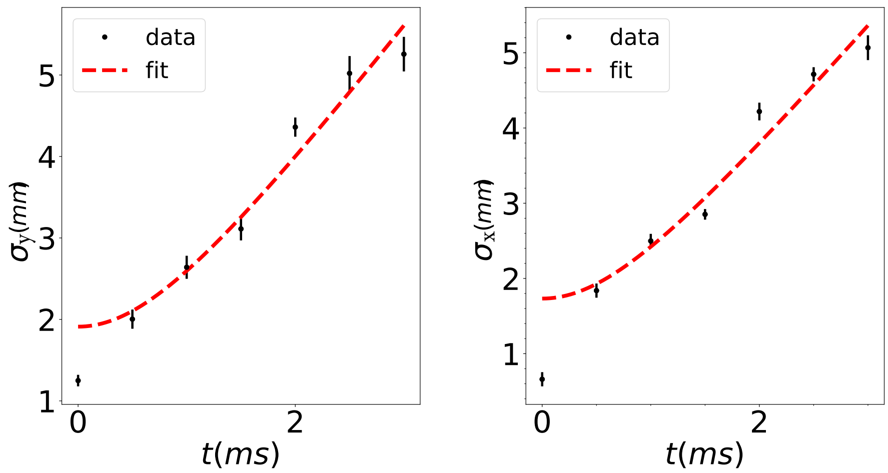

Figure 2.12: The widths σ_z (left) and σ_r (right) of the atomic cloud without in-trap cooling vs time of the fight. The fit is to Eq. (2.5). Data are shown as black dots, with fits shown in red dashed lines. The estimated temperatures are $\sim 747\ \mu K$ and $\sim 693\ \mu K$ along the vertical (z) and horizontal (r) direction of the cloud respectively, with $\sim 5.3 \times 10^7$ atoms.

To cool the cloud further it is illuminated for 500 ms with a 1D Doppler (in-trap) cooling beam [40] of intensity $\sim 0.01\ I_{sat}$, aligned vertically along the bias field axis, circularly polarised to drive the σ^+ transition and red detuned by $\sim -\Gamma/2$. The effect of in-trap cooling can be examined by the time of flight measurements using absorption imaging. For this purpose, several time of flight images are taken after 500 ms of in-trap cooling (see Fig. 2.13). The widths of the expanded cloud are plotted vs the corresponding time of flight, shown in Fig. 2.14. In this case, The estimated temperatures are ~ 140 and $\sim 250\ \mu K$ along the vertical (y) and horizontal (r=x) direction of the cloud with $\sim 4.9 \times 10^7$ atoms respectively. Due to the in-trap cooling the temperature along each direction is significantly reduced compared with Fig. 2.12 with just 7 % reduction in the number of atoms. After the in-trap cooling stage, the temperature is suitable to transfer the cloud to our optical dipole trap.

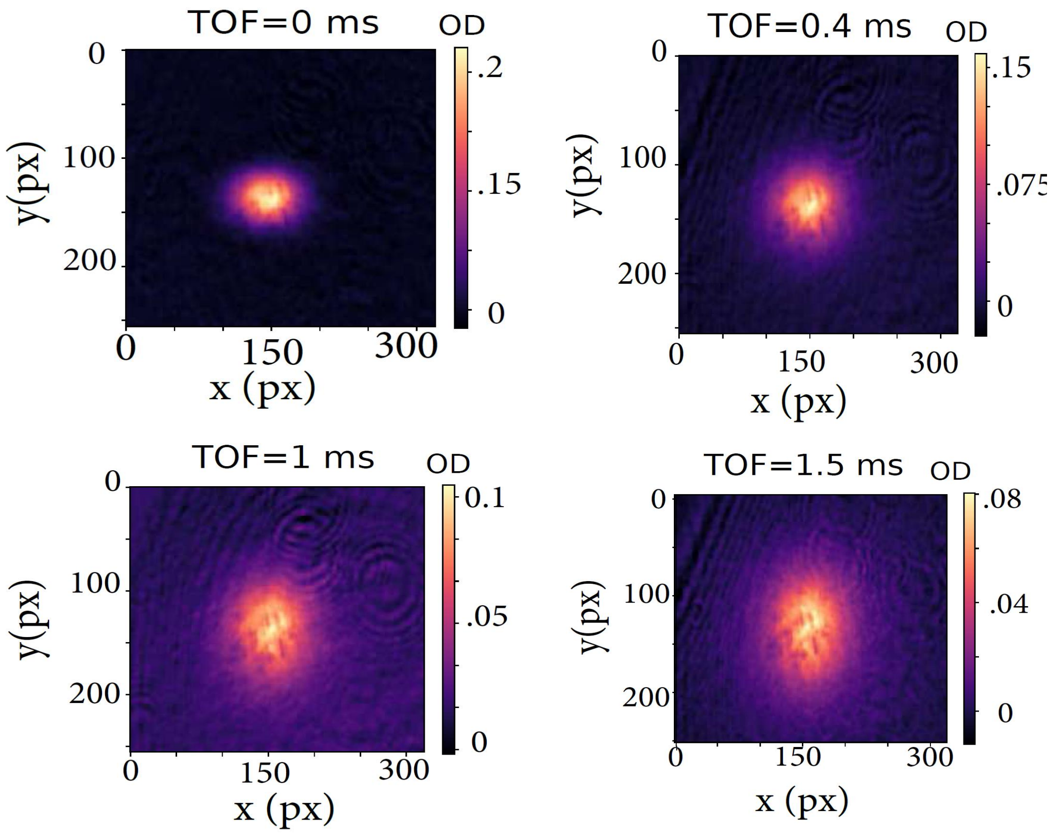

Figure 2.13: Time of fight profiles of the atomic cloud from our magnetic trap via absorption imaging after 500 *ms of in-trap cooling. The TOFs (0, 0.4, 1, and 1.5 ms) are taken after switching off the magnetic trap.*

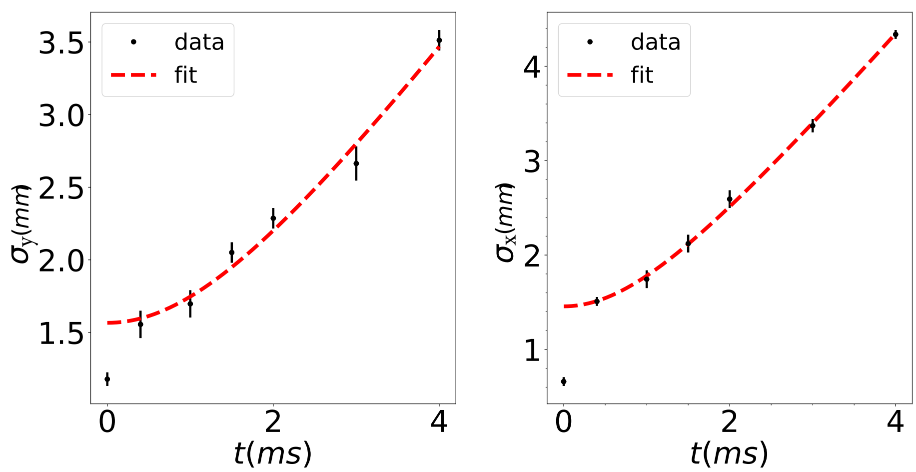

Figure 2.14: The fitted widths σ_z (left) and σ_r (right) of the atomic cloud with in-trap cooling vs time of flight. Data are shown as black dots, with fits shown in red dashed line based on Eq.(2.5). The temperatures are ~ 140 μK and ~ 250 μK along the vertical (z) and horizontal (r) direction of the cloud respectively, with $\sim 4.9 \times 10^7$ atoms.

Quantitative analysis of TOF: MCP

As a consistency check, the cloud from the magnetic trap is released to free fall on the MCP and the time of flight trace is fitted to the distribution in Eq.(2.4).

Without in-trap cooling, the TOF trace from the MCP is shown in Fig. 2.15 (a). The estimated temperature is ($\sim 440\ \mu k$) for the atom number of $\sim 1.5 \times 10^7$ atoms. Again, to check the effect of in-trap cooling using the MCP, the time of flight measurement is taken by dropping the cloud on the MCP after the in-trap cooling as shown in Fig. 2.15 (b).

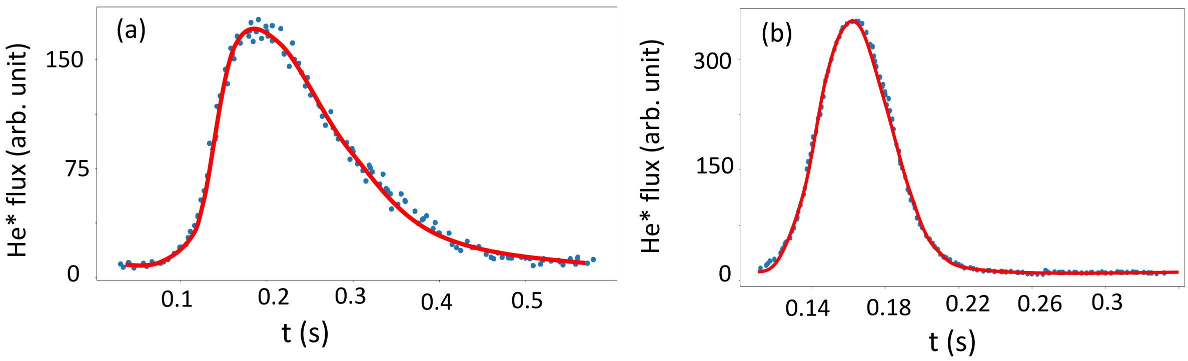

Figure 2.15: Time of flight signal trace taken from the MCP after the magnetic trap is switched off (a) without, (b) with in-trap. Data is shown as blue circles, with fits shown in red. The fit is to a Max-Boltz distribution in the far field after TOF given by Eq. (2.4).

The best fit is obtained for temperature of $\sim 83\ \mu K$ after 500 ms of in-trap cooling. This is sufficiently cold to directly transfer the atoms from the magnetic trap to the crossed optical dipole trap. The atomic cloud confined in the magnetic trap is relatively hot and broad on the MCP detector and thus a small fraction is hitting the MCP. consequently, the atom number of the cloud would be underestimated.

The results show that the temperature measured using the MCP is nearly half of that estimated from the absorption imaging. This discrepancy may be because the TOF measurement is taken by switching off our 10G magnetic trap, which may lead to a stray field affecting the short TOF ($TOF < 2$ ms in the case of the absorption imaging compared to $TOF =\sim 300$ ms the cloud takes to hit the MCP).

Before proceeding to the optical dipole trap stage, it is worth checking the magnetic trap lifetime. The long trap lifetime is necessary for cooling beyond a MOT and allows efficient transfer to the optical dipole trap. In the science chamber, the vacuum is of order

3×10^{-11} mbar, which permits the production of BEC since it yields a good magnetic trap lifetime. The lifetime of the atoms in the magnetic trap was measured using the absorption imaging method and the MCP method. The MCP method yields a $1/e$-lifetime of 5.5(2) s as shown in Fig. 2.16.

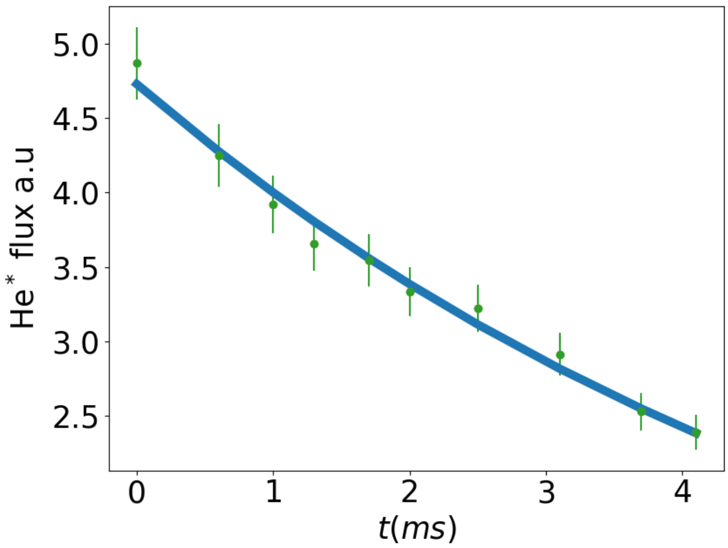

Figure 2.16: The magnetic trap lifetime using MCP detector. The atomic flux in a.u as a function of TOF in ms represents in the green circle. The blue curve is the exponential model that fit the data. It indicates that the lifetime of the magnetic trap is $\sim$ 5.5 s.

2.4.4 Optical dipole trap

A crossed optical dipole trap (CODT) is formed from two intersecting laser beams far detuned from the 1083nm helium resonance at 1550nm. It is generated from a 100kHz linewidth seed laser that is amplified to 30 W. The power is distributed between the two beams such that after feedback loops to regulate the intensity and losses due to AOM and fiber coupling the first beam (aligned along the y axis) has up to 6 W and the second beam (aligned $\sim 10°$ from the x axis in the $x - y$ plane) has up to 1 W of power.

By mounting an InGaAs camera on a sliding rail, the beam profile is measured by taking images which are then fitted to 2D gaussian profiles. The Gaussian widths at different positions along the rail are plotted and fitted by the expression $w(z) = w(0)\sqrt{1 + z/z_R}$ for the waist of a Gaussian beam. These beams are focused down to Gaussian $1/e^2$ waists of 73 μm and 55 μm, respectively, at the location of the atoms as described in Fig. 2.17.

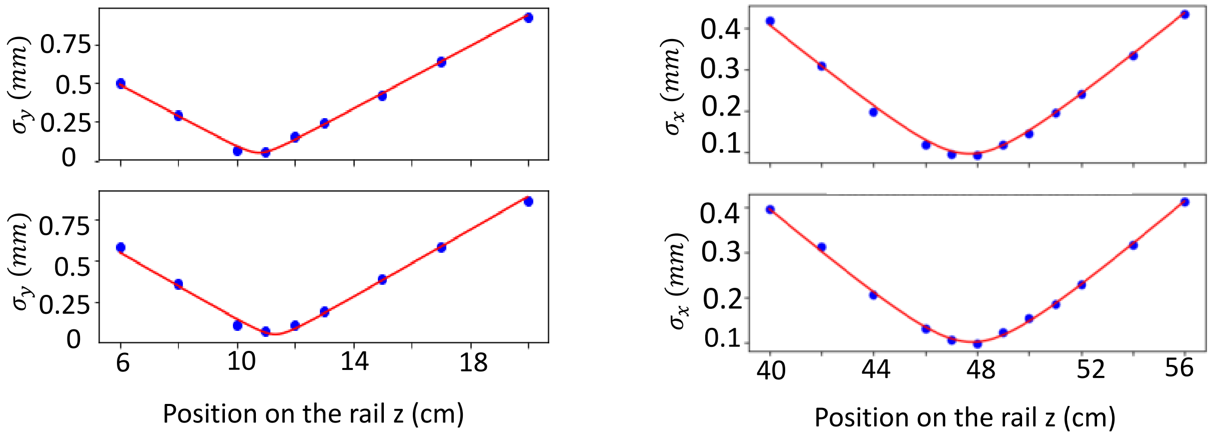

Figure 2.17: Using an InGaAs camera sliding on a rail, the dipole beam profile at different positions on the rail is taken and fitted to the 1D gaussian function. The Gaussian width along each direction is plotted vs the camera position on the rail from which the beam waist is extracted. The beams have waists of $73\mu m$ *and* $55\mu m$*, respectively, at the location of the atoms.*

Using a low-power resonant light beam at 1083 nm transmitted through the dipole fiber, the dipole setup was first aligned to overlap with the magnetic trap, since the resonant beam causes a 'split' in the atomic cloud, the beam splits the cloud in the magnetic trap as shown in Fig. 2.18.

The two beams intersect at the centre of the 10G biased QUIC trap, forming a CODT with trapping frequencies $\omega_{x,y,z} \sim 2\pi \times (1.1, 1.2, 1.7)$ kHz and a trap depth of $\sim 150\mu$K at full power (see Fig. 2.19). The overlapping between the two dipole beams occurs in the focal region within less than 100 μm at an angle of 100^o. To check this overlapping, we first load the cloud into the high power beam which is followed by switching off the magnetic trap, while simultaneously the second dipole beam is ramped up in 100 ms. The cloud is then held in the CODT for 300 ms. By dropping the cloud on the MCP from each individual beam at different times, a TOF signal is observed corresponding to the switch-off time of each dipole beam.

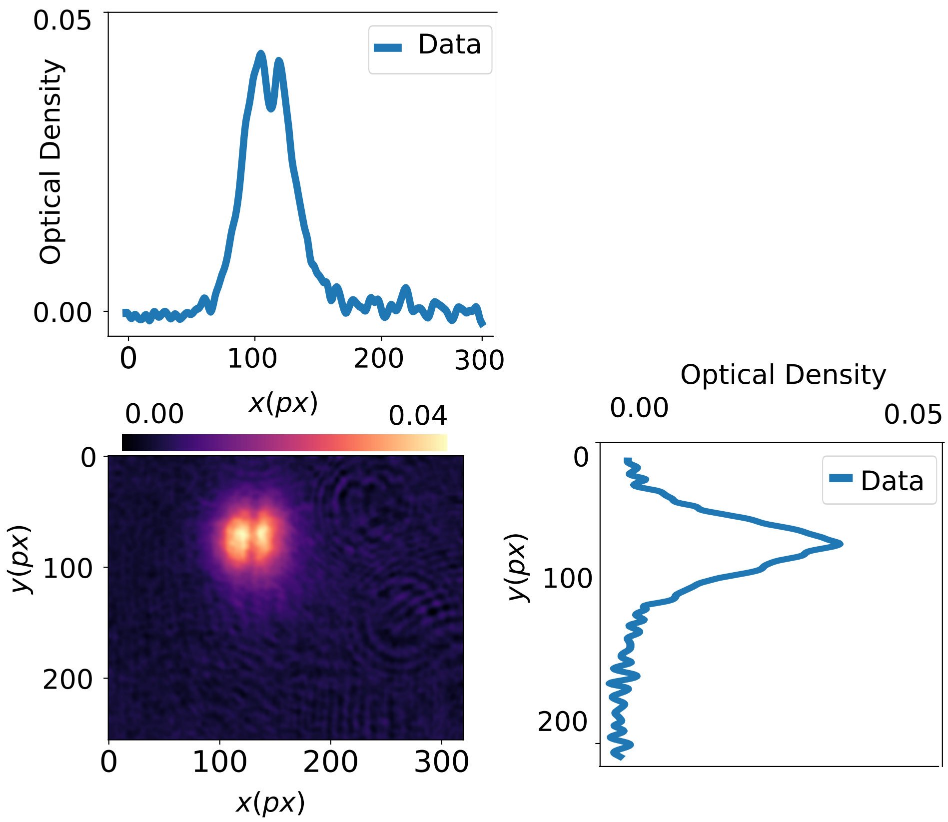

Figure 2.18: the alignment of the dipole beam (1550 nm) was achieved by passing resonant light (1083 nm) through the dipole fiber. A clear crack in the atom cloud is observed, confirming that the resonant beam is aligned and thus the dipole setup must be close to alignment.

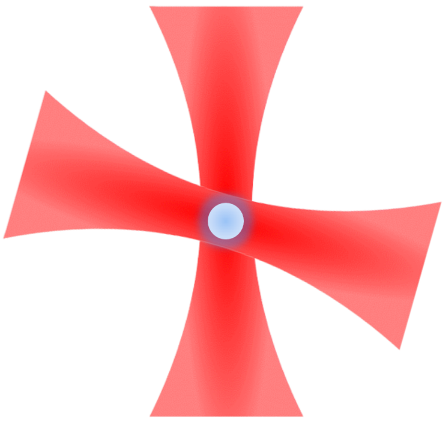

Figure 2.19: Schematic diagram showing the crossed-beam optical dipole trap (CODT) used in our experiment. Overlapping of two far-detuned laser beams (1550 nm) to form 3D confinement.

2.4.5 Loading of optical dipole trap

Since the 1D Doppler cooling process is more efficient at higher densities [40], we observe that the Doppler cooling is more effective with the dipole beams on, in addition to the magnetic trap. Here the dipole beams mostly serve to increase the density of the atomic cloud, making the cooling process more efficient and reducing the final temperature after 1D Doppler cooling. In our experiment, this improves the final atom number by $\sim 50\%$. Hence the dipole beams are linearly increased to full power over 100 ms prior to the start of the 1D Doppler cooling stage.

The atoms are transferred from the QUIC to the dipole trap, after the 1D Doppler cooling stage by linearly ramping the trap down in 100 ms to a non-biased trap with $\sim$ 1.1G/cm gradient along the tight axis, before being abruptly turned off with a FET switch. In the meantime, to preserve the quantization axis of the atoms and prevent any spin flips during this switch-off, an additional large ($\sim$50 cm diameter square) coil mounted above the vacuum chamber was used to generate a uniform magnetic field of $\sim$ 1.6 G aligned along the $\hat{z}$ direction. This field is switched on before the current through the QUIC trap starts ramping down. However, once in the dipole trap, it was found that the background magnetic field (dominated by the z component of the Earth's magnetic field) was sufficient to preserve the quantization, so the extra quantization coil was switched off 700 ms after transfer to the CODT. Immediately after the transfer, we measure $\sim 5 \times 10^6$ atoms at $13.5(1)\mu$K with a phase space density of ~ 0.5 in the CODT, an excellent starting point for runaway evaporative cooling.

2.4.6 Evaporative cooling

Evaporation is performed in the CODT by lowering the trap depth by reducing the power of the dipole beams exponentially over 1 second. As the hotter atoms escape and the remaining atoms are thermalized, this reduces the temperature and enhances the phase-space density. The evaporation duration is set by the relatively high trap frequencies (and thus high re-thermalization rates). Unlike in a previous similar He* experiment [44], we did not observe any improvement in the evaporation process by adding a gradient to cancel the weak components of the dipole potentials along the beam propagation directions.

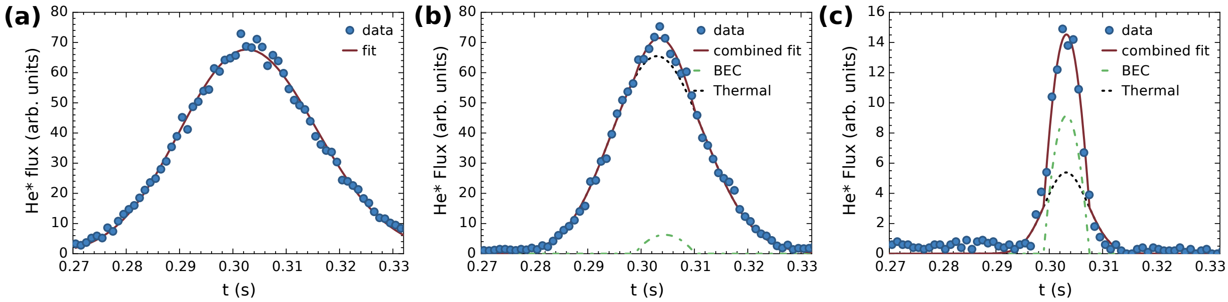

Figure 2.20: Time of flight signal traces taken from the MCP after the dipole trap is switched off and atoms are allowed to fall onto the detector. The three plots show different points in the evaporation sequence. Data is shown as blue circles, with fits shown in red. Above T_c the fit is to a Maxwell-Boltzmann distribution, while below T_c a parabolic Thomas-Fermi fit to the BEC component (green dot-dash line) is added to the thermal fit (black dashed line). The conditions for the plots shown are: (a) reduced temperature T/T_c = 1.02(5), trap frequencies $\omega_{x,y,z} \sim 2\pi \times (1100, 920, 1400) Hz$, total atom number $N = 3.3(2) \times 10^6$. (b) T/T_c = 0.88(7), $\omega_{x,y,z} \sim 2\pi \times (720, 590, 940) Hz$, $N = 1.7(2) \times 10^6$, condensate atom number $N_0 = 0.2(1) \times 10^6$. (c) T/T_c = 0.54(6), $\omega_{x,y,z} \sim 2\pi \times (320, 160, 360) Hz$, $N = 1.5(5) \times 10^6$, $N_0 = 1.2(4) \times 10^6 m$. Each image represents data from 20 shots.

To determine the important parameters of the gas in the CODT, we switch off the dipole trap and allow the atoms to fall under gravity onto the MCP. Examples of the resulting integrated 1D TOF profiles are shown in Fig. 2.20. Above the condensation critical temperature T_c^* (note that T_c refers to the non-interacting critical temperature, while T_c^* is the critical temperature corrected for interactions [62]), the profile is fitted to the same Maxwell-Boltzmann distribution as in Eq. 2.4 to yield the temperature T. Below T_c^* we fit with a bi-modal distribution consisting of the same Maxwell-Boltzmann distribution plus an inverted parabola to represent the far-field Thomas-Fermi density profile of the BEC [62]

$$n_{TF} = n_0 max\Big(1 - \Big(\frac{t - t_0}{R_{TF}}\Big)^2, 0\Big), \tag{2.6}$$

where n_0 is the peak density and t_0 is the arrival time. The half-width of this parabola is the far field Thomas-Fermi radius R_{TF}, from which the chemical potential μ can be extracted as $\mu \approx mR_{TF}^2/2t_{TOF}^2$. While this approximation for the chemical potential from the far field R_{TF} is only valid for condensates in cigar-shaped traps, numerical solutions of the equations of motion following [63] show that it gives at most an 10% error in μ for the trap geometries in our system, which is within our experimental uncertainties. From the chemical potential we can extract the number of atoms in the condensate as

$$N_0 = (2\mu)^{5/2}/15\sqrt{m}\hbar^2\bar{\omega}^3 a \tag{2.7}$$

where a is the He* $s-$wave scattering length. The number of atoms in the thermal cloud N_T is given by, for $T < T_c^*$.

$$N_T \approx 1.202\,(k_B T/\hbar\bar{\omega})^3 \tag{2.8}$$

To obtain the atom number above T_c^*, we sum the integrated counts, correct for the fraction of the cloud at temperature T that will hit the detector, and then scale by an effective quantum efficiency of the detector γ_{QE}. We vary γ_{QE} until the thermal atom number N_T matches the clouds just above and below T_c^*. Note that non-linearities in γ_{QE} at high fluxes mean this is not accurate for N_0.

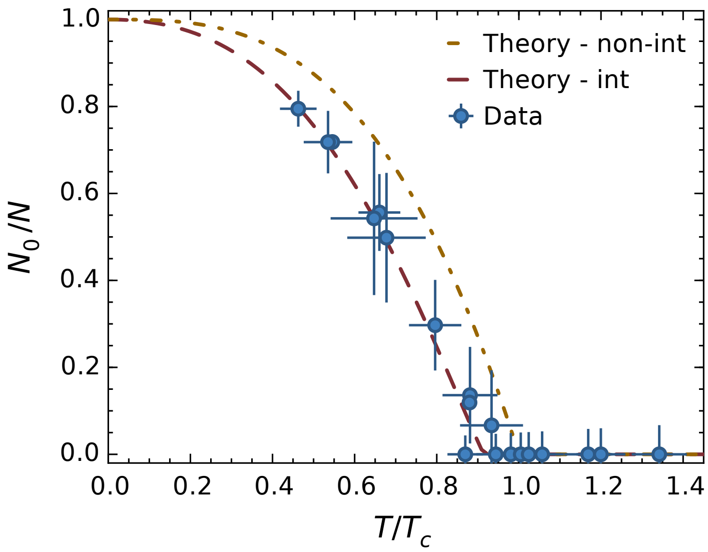

Figure 2.21: Condensate fraction N_0/N verses reduced temperature T/T_c for different points in the evaporation sequence. Data are shown as blue points. The brown dot-dash line shows the non-interacting theory, while the red dashed line shows a correction accounting for two-body interactions. For $N_0/N \gtrsim 0.8$ the thermal component is obscured by the condensate, which prevents reliable fits, hence the final evaporation points are not shown.

The above information, along with the total atom number $N = N_0 + N_T$ and $k_B T_c = 0.94\hbar\bar{\omega}N^{1/3}$, is then combined to produce Fig. 2.21. This shows the condensate fraction N_0/N vs the reduced temperature T/T_c for our sequence as we evaporate through the transition temperature. We cross T_c^* at $\sim 6\mu K$ with $\sim 3 \times 10^6$ atoms, and by evaporating further we are able to produce BECs with no discernible thermal fraction (not shown on the graph) with $\sim 1 \times 10^6$ atoms.

2.5 Control sequence and full TOF trace

The full temporal sequence controlling our experiment is depicted in Fig. 2.22. The MOT is loaded for 1 s. The quadrupole trap is then relaxed over 10ms and the cloud is then compressed by ramping the laser detuning up to $\Delta \sim -0.4\Gamma$ at low intensity. The quadrupole field is then tightened to 16.6G/cm in 100μs prior to loading into the biased magnetic trap. The bias coil current is then ramped up in 100ms to form a QUIC trap with a 10G field offset, removing the magnetic field zero in the quadrupole trap. At this point, the 1D doppler cooling starts for 500 ms, while simultaneously the intensity of the dipole laser beam is ramped up to 100 ms. The CODT loading occurs over 700 ms and is followed by 1s evaporative cooling. Finally, the cloud is held in the final trap for 100 ms to ensure the atoms are thermalized before the dipole trap is switched off and the atoms fall onto the MCP-DLD detector.

In the context of producing a He^* BEC using a stand-alone optical dipole trap, previous study has relied on a hybrid trap system [44]. This typically involved radio-frequency evaporation within a quadrupole magnetic trap, followed by transferring the cloud of atoms into a Conservative Optical Dipole Trap (CODT). Our approach, however, employs an in-vacuum QUIC trap to attain high atomic densities at a relatively low temperature of 83 μK. This low temperature allows for efficient transfer of the atomic cloud into the CODT, where a fast and efficient one-second evaporative cooling process is performed.

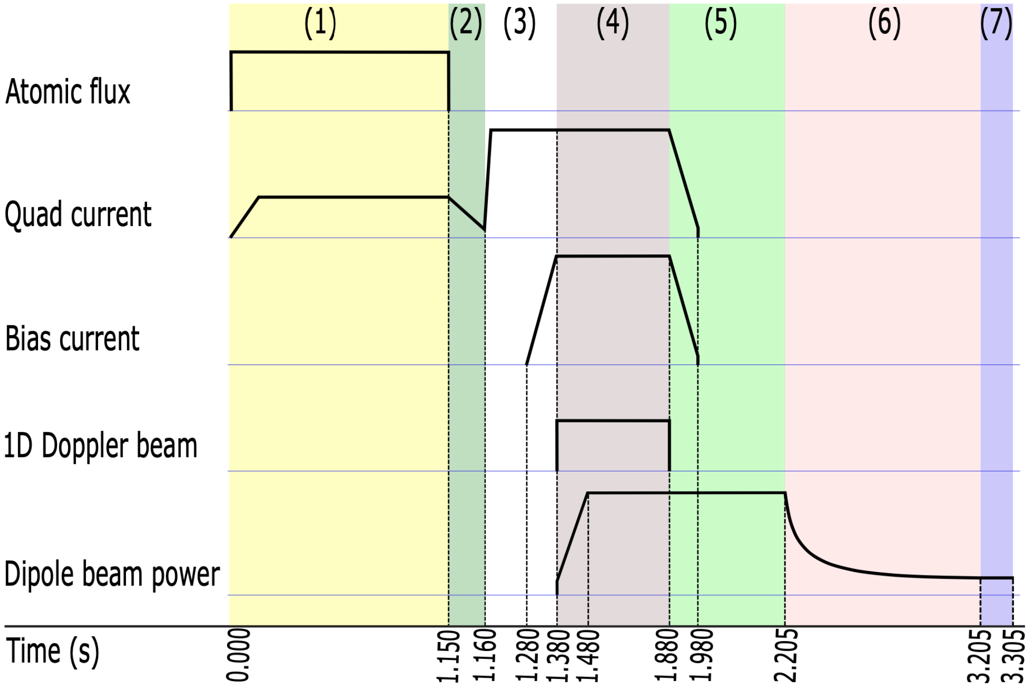

Figure 2.22: The timings of important stages of the experimental BEC production sequence. (1) the MOT is first loaded from the atomic flux (in the diagram representing Zeeman slower, first MOT, etc.). The MOT is then compressed (2) prior to loading into the biased magnetic trap (3). 1D Doppler cooling is then performed in the magnetic trap (4), which is subsequently ramped down for transfer to the dipole trap (5). Finally, an evaporative cooling stage (6) in the dipole trap is followed by a short hold (7) to ensure the atoms are thermalized before the dipole trap is switched off and the atoms fall onto the MCP-DLD detector. Note that to help with visualization, the time axis is not scaled.

For completeness, we show a typical time of fight trace for the whole experimental sequence obtained from the MCP (see Fig. 2.23). It is comprised of three main sections: the first broad signal occurring between $t = 0$ to 1s is due to the penning ionization of He* while loading the MOT which leads to a high level of ions hitting the MCP. There is a high saturated "M-"like peak that occurs between $t = 2.8$ to 3.4 s, which corresponds to the atomic cloud trapped in the magnetic potential. In order to extract useful information from this peak, the gain of the MCP should be reset to remove the saturation before dropping the cloud on the MCP (see Fig. 2.23). The last peak appears at $t = 3.8$ s, which represents the atoms trapped in the optical dipole trap before it is cooled evaporatively to BEC. This peak is well-fitted to a Maxwell-Boltzmann distribution as shown in the inset (zoomed in on the peak).

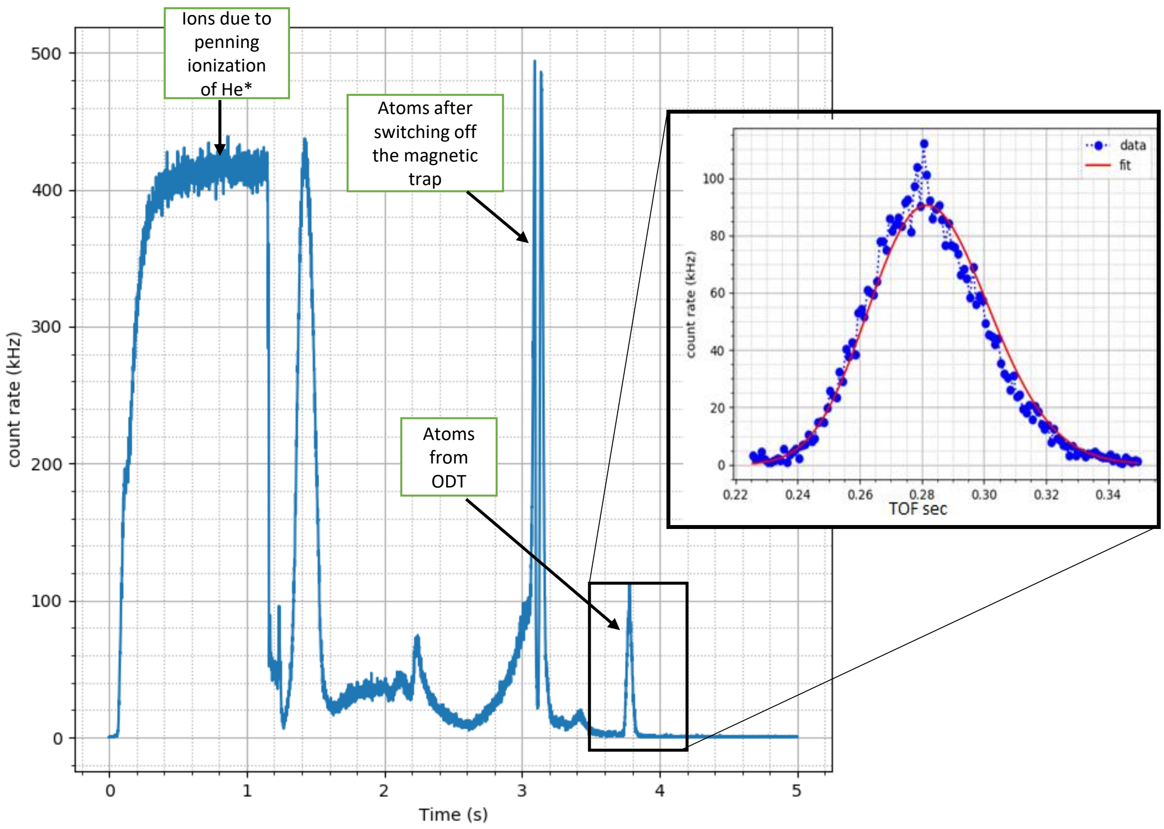

Figure 2.23: The full TOF trace from the MCP for optical dipole trap loading.

2.6 Summary and discussion

We demonstrate a comparatively simple and short method for producing Bose-Einstein condensates of He* atoms. By using a magnetic trap with a 10G bias generated from an in-vacuum set of coils, we are able to cool the cloud below 100 μK in the magnetic trap via 1D Doppler cooling. The degenerate state of metastable helium atoms is accomplished via direct evaporative cooling in a crossed optical dipole trap. We cross the condensation critical temperature with $\sim 3 \times 10^6$ atoms at ~ 6 μK and by evaporating further are able to generate essentially pure BECs with $\sim 10^6$ atoms. The entire sequence to produce a BEC only takes 3.3 sec.

This approach has several benefits, including the elimination of the need for radio-frequency evaporation in a quadrupole magnetic trap, as the low temperature makes it feasible for the cloud to be captured by the CODT. Furthermore, the usage of a dipole trap in the form of a CODT enhances the stability of the experimental cycle and expedites data acquisition time. For instance, to quantify the speed-up for He* BEC production achieved in our experimental setup, if a 3-second sequence is used for 100,000 experimental runs, it would take approximately three consecutive days to complete the process, whereas a 6-second sequence would take six days. This noteworthy decrease in time would accelerate the data collection required to measure many-particle correlations.

The design of the two coils arranged in an anti-Helmholtz configuration is characterized by its simplicity and offering substantial optical access. This presents new opportunities for exploring correlations among multiple particles using metastable helium atoms in experimental setups of particular interest, particularly those that utilize optical lattice potentials.

This page intentionally left blank.

Part II

Atomic condensate in the p-band of a bipartite optical lattice

This page intentionally left blank.

Chapter 3

P-band ultracold atoms in an optical lattice.

THE advent of optical lattices followed the dramatic progress in laser cooling. They now provide a common tool for the manipulation and control of quantum gases. In this chapter, we discuss the theory of optical lattice potentials. We also give a brief introduction to p-band BEC in optical lattices.

3.1 Optical lattices

Optical lattices are artificial crystals of light generated by the interference between far-detuned laser beams where the atoms can be trapped near the nodes or the antinodes of the interference pattern. The early experiments [64] were conducted with very diluted gas (one atom per hundred lattice sites). A new regime with a high filling factor is opened by the advent of quantum degenerate atomic gases, which enables exploring quantum many-body phenomena.

Bose–Einstein condensate (BEC) in optical lattices allows investigation of various quantum many-body phenomena in periodic potentials ranging from strongly correlated systems [65], to implementations in information technology [66]. Due to their high controllability, optical lattices can be spatially reconfigurable, which opens the possibility to study rich and complex dynamics. Moreover, ultracold atoms in optical lattices have been used in various experiments, such as atom diffraction [67, 68], and atom interferometry [69].

Several lattice geometries can be accessed depending on the laser beam configuration. In 1D, two counter-propagating plane waves with momenta $\pm k = \pm k e_x$ along the x-direction produce a standing wave pattern that forms an array of microtraps in one dimension. A sinusoidal lattice potential is formed, such that

$$V(x) = -V_0 \cos^2(k_0 x) \tag{3.1}$$

with $k_0 = 2\pi/\lambda$ is the wave vector of the laser light and V_0 is the potential depth of the optical lattice in units of the recoil energy $E_r = \hbar^2 k_0^2/2m$ where m is the mass of a single atom. In higher spatial dimensions, optical lattices can be generated by superimposing standing waves from different directions, where a periodic structure is formed at the center. For instance, a 2D optical lattice potential of form [5]

$$V(x, y) = -V_0(\cos^2(k_0 x) + \cos^2(k_0 y) + e_x.e_y \cos(\theta)\cos(k_0 x)\cos(k_0 y)) \tag{3.2}$$

can be generated by overlapping two orthogonal standing waves with relative phase difference θ and polarization vectors e_x and e_y. If the polarization vectors are orthogonal, a single-period square lattice emerges. Otherwise, a chequerboard potential is formed in which the depth of neighboring lattice sites changes depending on the relative phase θ. For sufficiently deep optical lattices, the atoms are trapped at the lattice sites, which are approximated by an on-site harmonic potential.

3.1.1 Bloch theorem

The features for a particle moving in a periodic landscape can be understood using *Bloch's theorem*. In this section, we present the mathematical model used to study the behavior of a single particle trapped in a periodic potential $V(x+a) = V(x)$ with a as a translation operator in real space. The periodicity of the optical lattice potentials induces a band structure with allowed energy bands called Bloch bands separated by forbidden gaps [70, 71]. These bands are associated with linear propagating modes called Bloch modes.

A particle in a 1D periodic potential V(x) can be described by the linear Schrödinger equation:

$$H\phi_q^n(x) = \mu_q^n \phi_q^n(x) \qquad\qquad H = -\frac{\hat{p}^2}{2m} + V(x). \tag{3.3}$$

The solutions of this equation can be expressed as a product of a plane wave $e^{(iqx/\hbar)}$ and a periodic function $u_q^n(x)$ with the periodicity of the lattice potential, which is known as Bloch wave functions:

$$\phi_q^n(x) = u_q^n(x)e^{iqx/\hbar} \tag{3.4}$$

where $q = k\hbar$ is a quasi-momentum vector. Using the Bloch ansatz Eq. (3.4) into Eq. (3.3) gives the Schrödinger equation for $u_q^n(x)$

$$\frac{1}{2m}(p+q)^2 u_q^n(x) + V(x)u_q^n(x) = \mu(q)u_q^n(x). \tag{3.5}$$

This Hamiltonian is quadratic in q, and is symmetric under time reversal symmetry. When $\phi_q^n(x) = \phi_{-q}^n(x)$, the spectrum is symmetric with respect to q (i.e $\mu(q) = \mu(-q)$). Since the Bloch waves u_q and the potential $V(x)$ have the same periodicity, they can be expressed as a discrete Fourier sum:

$$V(x) = \sum_l V_l e^{i2lkx} \qquad\qquad u_q^n(x) = \sum_j c_j^{(n,q)} e^{i2jkx}$$

where l, j are integers. The nonzero Fourier amplitudes can be obtained by equating the above Fourier sum with the potential in the plane wave basis. For the non-interacting case, the matrix form of the eigenvalue equation (3.5) can be diagonalized and the band structure of the periodic potential given by (3.1) is derived based on Bloch theorem, with the quasi-momentum q is restricted to the first Brillouin zone: $-\hbar k_0 < q < \hbar k_0$.

$$\sum_j H_{jj'} c_j^{(n,q)} = \mu_q^n c_j^{(n,q)}. \tag{3.6}$$

With the potential given by Eq. (3.1), the coupling matrix elements $H_{jj'}$

$$H_{jj} = E_r(k/k_0 + q)^2, \qquad H_{j;j\pm 1} = -V_0/4,$$

the eigenenergies μ_q^n of the Bloch states $\phi_q^n = \sum_l u_l^{n,q} e^{i2lk_0x}$ are extracted, where the index n is the band index and l is an integer.

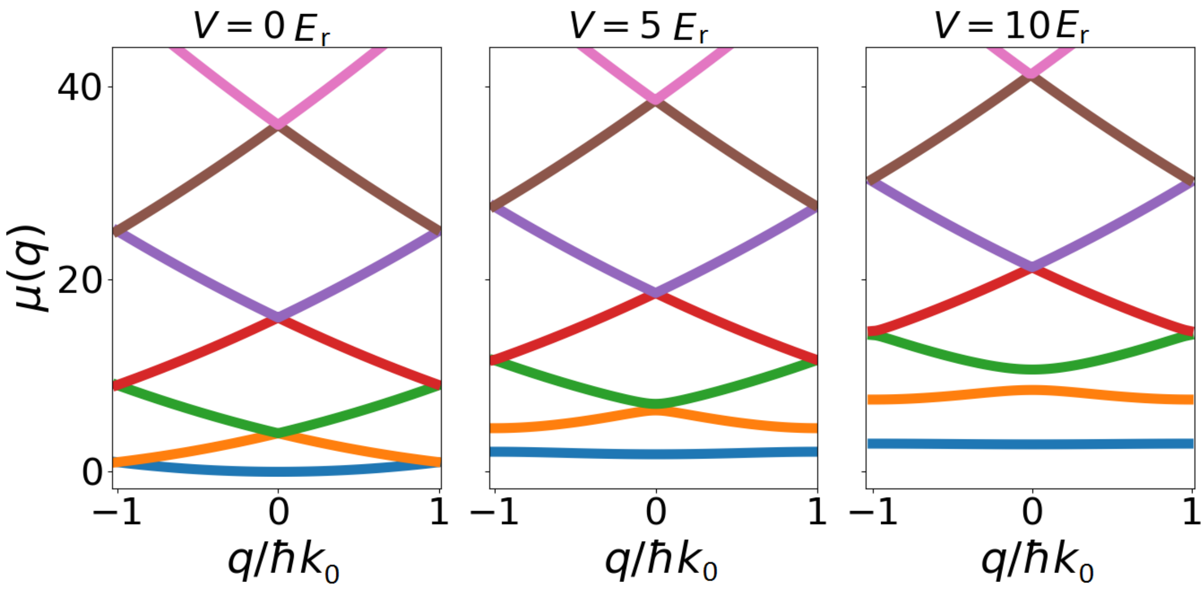

Figure 3.1: Band structure of the 1D optical lattice given by Eq.(3.1): Energy of the Bloch waves ϕ_q^n versus quasi-momentum q, is plotted for different lattice depths between 0, 5 and 15 E_r. For deep lattices the lowest band becomes flat and a full bandgap is formed between the ground state (blue) and the first excited state (orange).

Figure. 3.1 shows the band structure for the lowest four bands of the one-dimensional sinusoidal potential given in Eq.(3.1) for different potential depths. For a shallow lattice $V_0 \to 0$, there are no band gaps and they are similar to the free particle energy-momentum parabola. For a deeper lattice, bandgaps open between the energy bands, and the width of the energy bands decreases.

In Figure.3.2, an example of the real part of a Bloch function of the one-dimensional sinusoidal potential is given in Eq.(3.1) with 5 E_r lattice depth.
The red solid line represents a symmetric Bloch function $\phi_{q=0}^{n=0}(x)$ in the lowest band $n = 0$ with a quasi momentum $q = 0$, and the blue solid line shows an anti-symmetric Bloch function $\phi_{q=\hbar k_0}^{n=0}(x)$ with $q = \hbar k_0$ at the edge of the Brillouin zone.

A cold atomic cloud loaded into an optical lattice potential can be manipulated in different ways such as shaking the optical lattice or modulating the amplitude of the lattice.

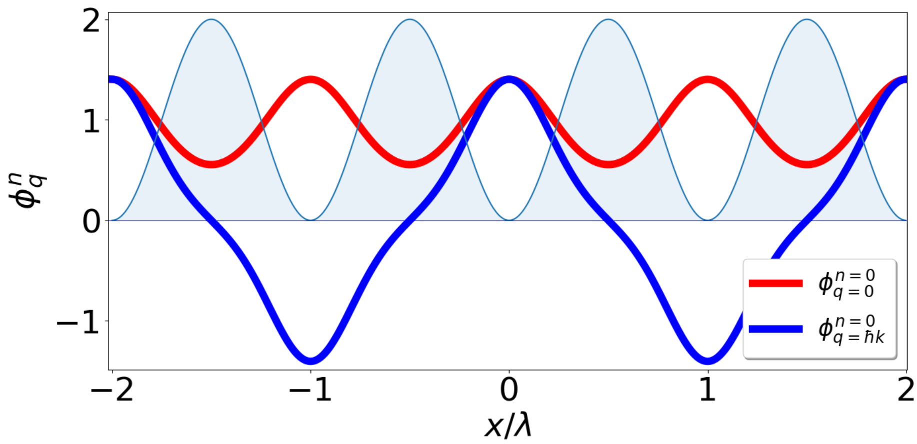

Figure 3.2: Real part of the Bloch wave functions ϕ_k^n in the ground ($n = 0$), corresponding to a quasi momentum of $q = 0$ and $q = \hbar k_0$. The lattice potential is a 1D sinusoidal potential with a lattice depth of 5 E_r. The shaded blue pattern represents the potential in Eq.(3.1)

The response and evolution of the atoms can be detected via absorption imaging time of flight profile, in which the atoms expand and spread out according to their momenta. Due to the periodicity of the lattice, the atoms can only change in momentum by $(\pm\hbar k_0, \pm\hbar k_0)$, which leads to a characteristic pattern consisting of series of peaks at momenta $\pm n\hbar k_0$ in the TOF profile.

3.2 Higher orbital bands in optical lattices

Orbital physics is the phenomena originating from considering the onsite orbital degree of freedom. In addition to spin and charge, the orbital degree of freedom is critical for the emergence of many complex phases in solid-state materials important to understand the essence of many complicated systems such as high T_c superconductivity in the cuprates [72], pnictides [73], colossal magneto-resistance observed in Mn oxides [74], and chiral p-wave superconductivity in Sr_2RuO_4 [75]. In solid-state materials, the electronic structure is determined by the formation of orbitals, which are determined by the distribution of electrons surrounding the ions in the crystal. According to the quantum atomic model, electrons are described by orbital wave functions. These orbitals are distinguished by their size, shape, and orientation, with the s-orbital being spherical and the p-orbital taking on a dumbbell shape with a node at the center where electron probability is zero. The shape of the orbital is dependent upon the quantum numbers associated with its energy state. The complexity of considering multiple degrees of freedom such as orbital and spin has made it difficult to fully understand. However, optical lattice potential offers a controlled platform for simulating multi-orbital systems.

According to Feynman's fundamental "no-node" theorem [76], the conventional coordinate representation of the many-body ground state wavefunctions of bosons is positive definite and thus spontaneous time-reversal symmetry cannot be broken (see Fig(3.3)). Therefore, investigation of orbital many-body physics is challenging.

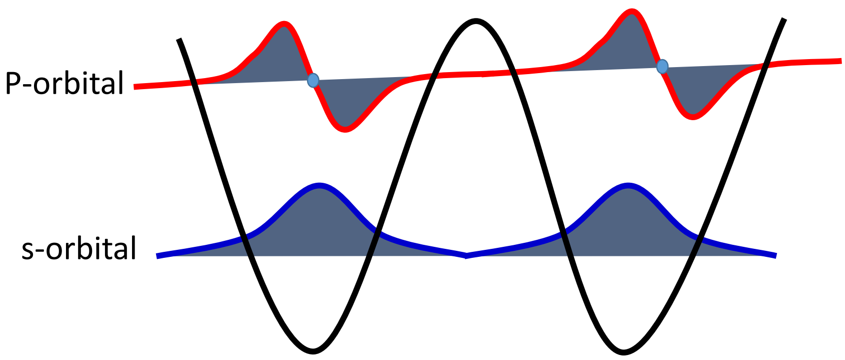

Figure 3.3: Confining double well potential (black) with the ground state (blue) and the first excited state (red). The ground state wave function is a positive definite and preserves the reversal symmetry, whereas the first excited state has a single node in the middle and breaks the reversal symmetry.

The wave function of a weakly interacting bosons ($\sigma \neq 0$) in an optical lattice potential $V(x)$ can be obtained by minimizing the energy functional

$$E[\psi] = \int dx \psi^* \Big(\frac{-\hbar}{2m} \frac{\partial^2}{\partial x^2} - V(x) - \mu + \sigma |\psi|^2 \Big) \psi.$$

The condensate wavefunction $\psi(r)$ is that of the lowest Bloch band corresponding to $k = 0$, which preserves the lattice translation and time reversal symmetries for weak interaction ($\psi(r) = \psi(r + a)$ and $\psi = \psi^*$). However, the long-lived high band states [77, 78, 79, 80], are described by a complex-valued many-body wavefunction and thus break time-reversal symmetry spontaneously. Optical lattices with higher band occupation allow investigating physics beyond conventional s-band Hubbard physics and tight binding model. Considering such state, exotic topological superfluid (SF) phases of p-orbitals for fermions[81, 82, 83] as well as bosons[77, 84] are induced by interaction effects combined with the p-band topology.

3.2.1 Chiral mode and orbital angular momentum

The chiral degrees of freedom can be realized in the matter and light fields. Chirality provides opportunities for the manipulation and control of quantum information and has an impact on quantum technology. The handedness of the chiral matter can be exploited to control electron and spin transport. Quantum devices based on the chiral matter are predicted to operate near room temperatures since the properties of the chiral matter are realized at room temperatures [85].

A chiral superfluid is a type of superfluid that exhibits both superconductivity and chirality. In a chiral superfluid, bosonic particles form a p-wave pairing state, characterized by a non-zero angular momentum, resulting in a circulating current of particles around the axis of rotation. The wavefunction of the bosonic particles in a chiral superfluid can be described by the following equation:

$$\psi(r,\theta) = \rho(r)e^{i\theta}, \tag{3.7}$$

where $\rho(r)$ is the density of particles in a chiral superfluid and θ is the polar angle. The density function describes the magnitude of the pairing, while the phase of the wavefunction describes the orientation of the pairing. In a chiral superfluid, the phase of the wave function has a non-zero angular momentum, leading to a circulating current of particles around the axis of rotation. This circulation of the current around the axis of rotation can be described by the following equation:

$$\Gamma = h/m \int |\psi(r,\theta)|^2 d\theta \tag{3.8}$$

where h is Planck's constant and m is the mass of the bosonic particles. The circulation of the current in a chiral superfluid is quantized, meaning that it can only take on certain discrete values, leading to a quantized angular momentum.

The topology of a chiral superfluid is described by the winding number, which represents the number of times that the wave function of the particles wraps around the axis of rotation. The winding number can be described by the following equation:

$$W = (1/2\pi) \int (\partial\theta/\partial r) d\theta \tag{3.9}$$

To visualize such a state, consider p-orbital wavefunctions of p_x, p_y configuration, which are oriented along x, and y axes respectively as shown in the top panels of Fig. 3.4(a),(b). Under special circumstances, these orbitals may be driven to form a vortex-like state. To be more precise, interaction effects may drive the local p-orbitals to create a chiral state of the form $p_x \pm ip_y$ which carries a quantized orbital angular momentum (AOM) as shown Fig 3.4(c).

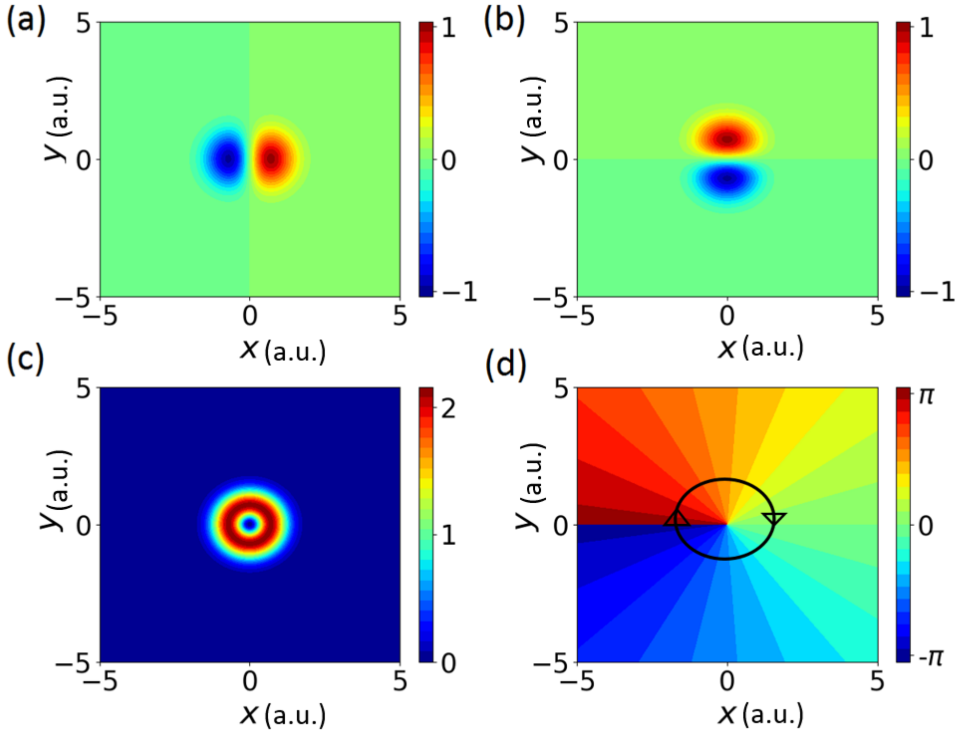

Figure 3.4: Contour plot shows the wavefunctions (a) p_x and (b) p_y orbitals, (c) the spatial density of the resultant vortex-like state $p_x + ip_y$ and (d) its phase structure $arg(p_x + ip_y)$. The phase structure shows that the phase winds around the vortex core by 2π. The color bars represent the peak height in arbitrary units.

In Fig. 3.4(c), a vortex is formed, which can be described by a complex-valued function of the phase winds around the vortex core in multiples of 2π as shown in Fig. 3.4(d). The rotation of the phase around the center of the vortex results in angular momentum. The orbital angular momentum per atom L_m in a unit of $\hbar$ carried by a vortex state is defined as

$$L_m = \frac{\Gamma}{\int |\psi|^2 dxdy} \tag{3.10}$$

Vortices are topological objects with quantized orbital angular momentum that have been extensively explored in a variety of physical systems for their potential application in information processing and storage [86]. The two different spinning directions of a vortex can be used to encode binary information [87, 88], which is the basis of vortex-based random access memories.

3.2.2 Chiral superfluid in bipartite optical lattice

In the optical lattice context, a chiral superfluid phase is realized in the p-bands of a square bipartite optical lattice. In the pioneering work by the group of Hemmerich [77], a system of weakly interacting bosons loaded into the p-band of a 2D bipartite optical lattice spontaneously arranged into a vortex array with global orbital angular momentum (OAM) across the entire lattice [89, 90]. Such a state is defined by a complex order parameter and breaks time-reversal symmetry. In this configuration, the coherence is established by tuning the population imbalance within the excited state which allows realizing such chiral superfluid phases. Chiral quantum states have an implementation in sensing, and storage of quantum information [85].

To describe a chiral superfluid in a bipartite optical lattice potential, we can use a two-component wave function, with each component representing the wave function on one of the sublattices:

$$\psi = (\psi_A, \psi_B). \tag{3.11}$$

The wavefunction of the bosonic particles in a chiral superfluid in a 2D bipartite optical lattice can be described by the following equation:

$$\psi(r,\theta) = \sum_{k,k'} (\Delta_k e^{i\theta_k} \psi_A^k(r) + \Delta'_k e^{i\theta'_k} \psi_B^{k'}(r)) \tag{3.12}$$

where $\Delta_{k,k'}$ proportional to the amplitude of each mode, $(\psi_A^k, \psi_B^{k'})$ are the wavefunctions of the bosonic particles on the A and B sublattices, respectively, and the sum is taken over all wavevectors k,k'.

The density of particles in a chiral superfluid in a 2D bipartite optical lattice can be described by the following equation:

$$n(r) = |\psi(r,\theta)|^2 = \sum_k |\Delta k|^2 (|\psi_A^k(r)|^2 + |\psi_B^k(r)|^2). \tag{3.13}$$

In this formulation, the chiral superfluid state can be characterized by a nonzero circulation of the particle density around a closed path, which can be quantified by the winding number of the phase difference between the two components of the wave function.

In conclusion, a chiral superfluid in a 2D bipartite optical lattice is a system in which bosonic particles are trapped in a two-dimensional lattice with two sublattices and form a p-wave pairing state, resulting in a chiral superfluid state. The wavefunction of the bosonic particles, the density of particles, the circulation of the current, and the topology of the system can be described by equations that include the gap function, the phase of the wavefunction, the wavefunctions of the bosonic particles on the A and B sublattices, and the winding number.

In the next two chapters, we numerically investigate the dynamics of interacting BEC loaded into the first excited state of a bipartite optical lattice. This work is based on the optical lattice potential used in the experiment conducted by Wirth et.al [77]. In chapter 4, we apply the coupled mode theory to analyze the stationary solution of a weakly interacting BEC loaded into the first excited state of a bipartite lattice potential. In chapter 5, we study the nonlinear localization of BEC in a 2D bipartite optical lattice. Combining the nonlinear effect with the lattice topology results in interesting localized self-trapped states in the first and second bandgap.

Chapter 4

Coupled-mode theory for BECs in a bipartite optical lattice.

THE dynamic of the confined condensate is analogous to that of the nonlinear optical waveguide. In nonlinear optics, nonlinearity causes the guided modes to couple, which results in intriguing quantum effects including quantum self-trapping (QST) and nonlinear phase shifting. [91].

We employ the coupled-mode theory [92, 93] to investigate the steady state of an interacting condensate loaded into the p-band of a bipartite optical lattice potential and demonstrate the possibility to create a superposition of Bloch states with a nontrivial orbital texture. Namely, we show that the superposition of the two Bloch states at the quasi-degenerate energy minima of the first band can lead to the formation of unconventional superfluid order with a global orbital angular momentum across the entire lattice.

This chapter supplements work that has previously been published in:

- [47]:- A. H. Abbas, Chiral superfluid in a one-dimensional bipartite optical lattice, Phys. Rev. A 105, 023327 (2022).

4.1 BEC in a bipartite optical lattice

The dynamics of the condensate in an optical lattice potential can be described by the Gross Pitaevskii equation (GPE), which is a nonlinear Schrodinger equation derived using the mean-field theory under the assumption of a macroscopically populated coherent state:

$$i\hbar\frac{\partial\psi}{\partial t} = (-\frac{\hbar^2}{2m}\nabla^2 + V + g_{2d}|\psi|^2)\psi \tag{4.1}$$

where $\nabla^2 = \partial^2/\partial x^2 + \partial^2/\partial y^2$, g_{2d} characterizes the two-body interactions for a condensate with atoms of mass m and s-wave scattering length a_s and V is the time-independent trapping potential. The scattering length a_s is either positive for repulsive interactions or negative for attractive interactions. Here, we consider V to be an optical lattice potential of the one-dimensional (1D) form

$$V(x) = -\frac{V_0}{4}|(e^{ik_0x} + e^{-ik_0x}) + e^{i\theta}|^2, \tag{4.2}$$

or the two-dimensional (2D) form [77]

$$V(x,y) = -\frac{V_0}{4}|(e^{ik_0x} + e^{-ik_0x}) + \epsilon e^{i\theta}(e^{ik_0y} + e^{-ik_0y})|^2, \tag{4.3}$$

where V_0 is the lattice depth, $k_0 = 2\pi/\lambda$ is the lattice wave number, λ is the wavelength of the laser beam. Eq. (4.1) can be rewritten in dimensionless form using the characteristic recoil energy $E_r = \hbar^2 k_0^2/2m$ and time $\omega_L^{-1} = \hbar/E_r$, and the lattice depth is measured in units of the lattice recoil energy, E_r. The GPE (4.1) in dimensionless form is given as

$$i\frac{\partial\psi}{\partial t} = -\nabla^2\psi + V\psi + \sigma|\psi|^2\psi. \tag{4.4}$$

In the normalized GPE (4.3), the wave function is re-scaled as $\psi \to \sqrt{g_{2d}}\psi$, and the sign of the nonlinear parameter $\sigma = sign(g_{2d}) = +1$ or -1, corresponding to repulsive and attractive interatomic interaction respectively.

The lattice anisotropy parameter ϵ can be experimentally adjustable, which accounts for an intensity imbalance between the laser beams (for the isotropic case $\epsilon = 1$). The angle θ is the relative phase between the oscillating standing waves, which can be tuned to control the relative depths of neighboring lattice sites. For $\theta = 0, \pi/2$, the standard single period lattice is realized with a 1D (2D) array of microtraps with equal depths as shown in Fig. 4.1. Furthermore, adjusting the relative phase such that $0 < \theta < \pi/2$ a double period lattice potential can arise with a chequerboard structure as shown in Fig. 4.2. The 1D (2D) lattice potential can be experimentally created by one (two pairs) of counter-propagating laser beams with the same angular frequency $\omega_L = ck_0$.

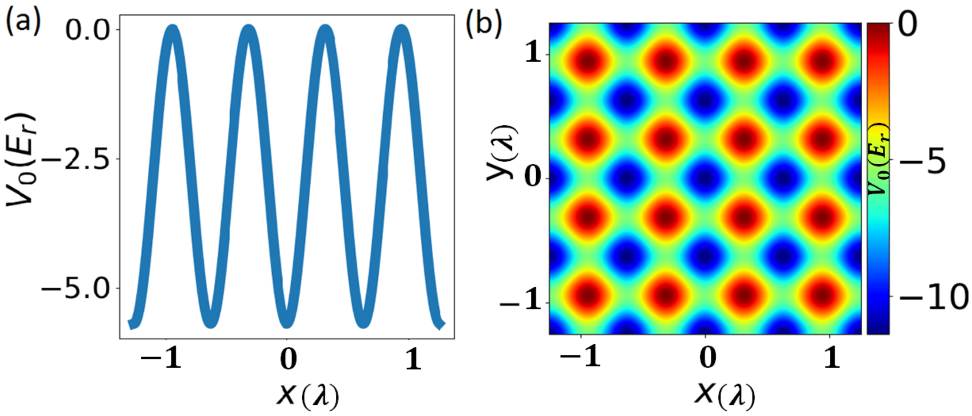

Figure 4.1: Single period lattice geometry in the (a) 1D and (b) 2D cartesian space as described in Eqs.(4.2),(4.4), for $V_0 = 5.7$ and $\theta = \pi/2$. The color bar represents the lattice depth in the units of E_r.

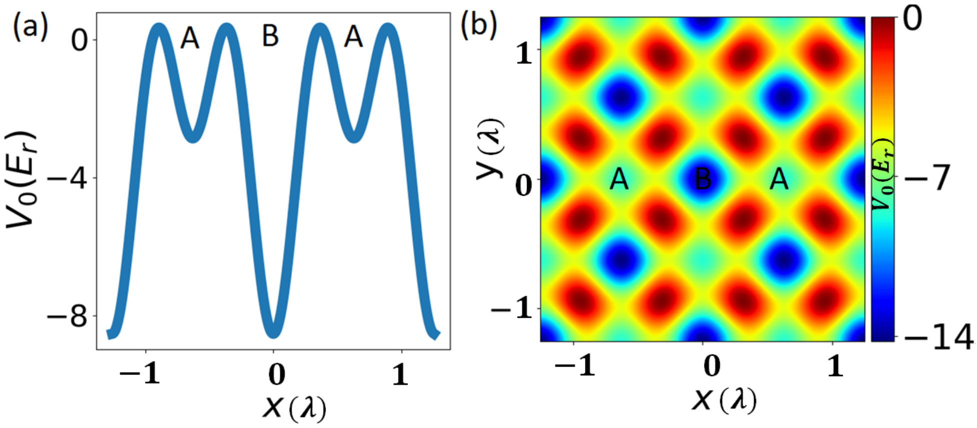

Figure 4.2: Bipartite lattice geometry in the (a) 1D and (b) 2D cartesian space as described in Eqs.(4.2),(4.4) with two potential minima denoted by A and B, for $V_0 = 5.7$ and $\theta = 0.43\pi$. The color bar represents the lattice depth in the units of E_r.

The bipartite lattice configuration of the potentials in Eqs. (4.2),(4.4) are realized for $V_0 = 5.7$ and $\theta = 0.43\pi$. The spatial structure of the 1D lattice potential shows a double period configuration with alternating deep and shallow sites as shown in Fig. 4.2(a). Also for the same setting parameters, the 2D optical potential in Eq. (4.4) exhibits a chequerboard structure with two potential minima denoted by A (shallow site) and B (deep site) as depicted in Fig. 4.2(b).

In the pioneering work conducted by Wirth et.al [77], an orbital superfluidity in the p-band of the 2D bipartite optical lattice shown in Fig. 4.2(b) was observed with a lifetime of several ten milliseconds. An atomic condensate of ^{87}Rb was initially prepared in the ground state of a bipartite optical lattice and then by swapping technique, the lattice parameters were adiabatically tuned so that the initial ground state band atoms became in resonance with the p-bands. The realized orbital superfluidity state is comprised of s-orbital in the shallow lattice sites and p-orbital hosted by the deep sites and is arranged in a pattern of staggered local phases. Interestingly, in the isotropic case, two degenerate minima are formed in the first exited state where p-orbital with $\pi/2$ phase difference resides in the deep wells. A complex-valued superfluid order is induced by the repulsive interaction between the local p-orbits, which breaks time-reversal symmetry, and is characterized by vortical plaquette currents [90].

Fig 4.3 shows the 2D bipartite lattice in the quasi-momentum 4.3 (a) and spatial 4.3 (b) representations. The two primitive lattice vectors are $a_{1,2} = \pi/k_0(\hat{x} \pm \hat{y})$ which correspond to the primitive reciprocal lattice vectors $b_{1,2} = k_0(\hat{x} \pm \hat{y})$. In 4.3 (a) the first Brillouin zone as a function of quasi momentum $k = (k_x; k_y)$ is shown. For convenience the quasi-momenta $q_{1,2} = k_x \pm k_y$ are defined. On this basis the first Brillouin zone is the square region$k_0 < q_{1,2} \leq k_0$.

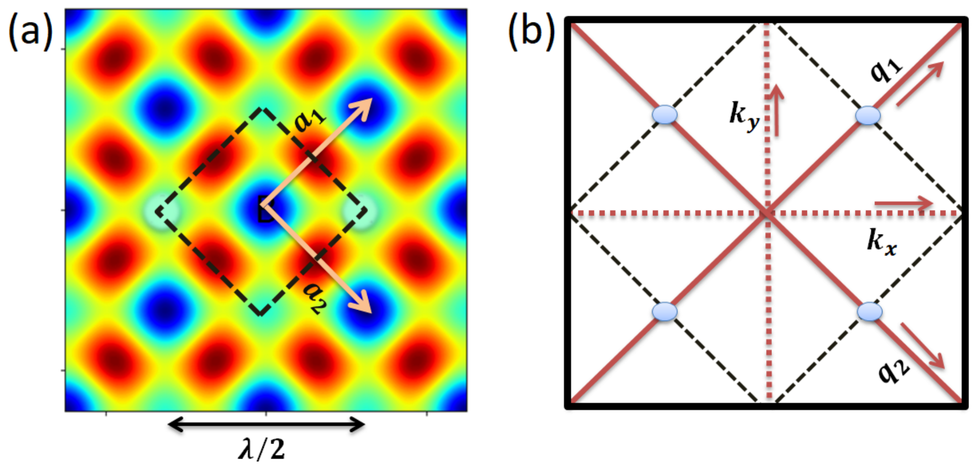

Figure 4.3: (a) shows the contour graph of the square bipartite optical lattice at $V_0 = 5.7E_r$ and $\theta = \pi/2$. The primitive lattice vectors are a_1 and a_2. The dashed lines enclose a unit cell. (b) shows the first two Brillouin zones of the optical lattice as a function of quasi momentum $q_{1,2} = k_x \pm k_y$. The area inside the dashed region represents the first Brillouin zone.

Motivated by this experimental setup, we present a simple theory to analyze the observed unconventional superfluid state in the bipartite potential shown in Fig. 4.2. We apply the coupled-mode theory [94, 95, 93] to study the steady-state solutions of a weakly interacting BEC loaded into the first excited state of the bipartite optical lattice potential. Our analysis starts with the investigation of the linear band-gap structure and Bloch waves of the 1D & 2D bipartite optical lattice potentials. Then we proceed by formulating the coupled mode theory for an interacting condensate loaded into the second band of a bipartite optical potential in one and two spatial dimensions.

4.1.1 One-dimensional band-gap structures

We assume a weakly interacting cigar-shaped condensate loaded into a 1D optical potential. The dynamics of the system can be described by the 1D GP equation:

$$i\frac{\partial\psi}{\partial t} = -\frac{\partial^2\psi}{\partial^2 x} + V(x)\psi + \sigma|\psi|^2\psi \tag{4.5}$$

where $\psi(x,t)$ is the condensate wave function, the trapping potential $V(x)$ is given by Eq. (4.2). The stationary states of a condensate in a 1D periodic potential are described by solutions of the form: $\psi(x,t) = \phi(x)e^{-i\mu t}$, where μ is the corresponding chemical potential and the spatial wave function $\phi(x)$ obeys the time-independent GPE:

$$\Big(-\frac{\partial^2}{\partial x^2} + V(x)\Big)\phi + \sigma|\phi|^2\phi = \mu\phi \tag{4.6}$$

For the non-interacting case ($\sigma = 0$), and according to the Bloch theorem, the stationary wavefunction can be written in terms of Bloch waves $\phi_q(x) = u_q(r)e^{iqx}$.
The linear version of Eq. (4.6) can be expressed in a matrix form $H\phi_q^n = \mu_q^n\phi_q^n$ with coupling matrix H with elements

$$H_{ll} = (k/k_0 + q)^2 \qquad H_{l;l\pm1} = -V_0\cos(\theta) \qquad H_{l;l\pm2} = -V_0/4,$$

The eigenvalues μ_q^n for the n^{th} energy band and the corresponding wavevectors $u^{n,q}$ of the coupling Hamiltonian matrix are calculated for quasi momentum q belongs to the first Brillouin zone (FBZ). The lowest four energy bands of the potential (4.2) with $V_0 = 5.7E_r$ and $\theta = 0.43\pi$ are shown in Fig. 4.4. Our calculations reveal that the first excited state (red line in Fig. 4.4) is characterized by two energetically degenerate minima at

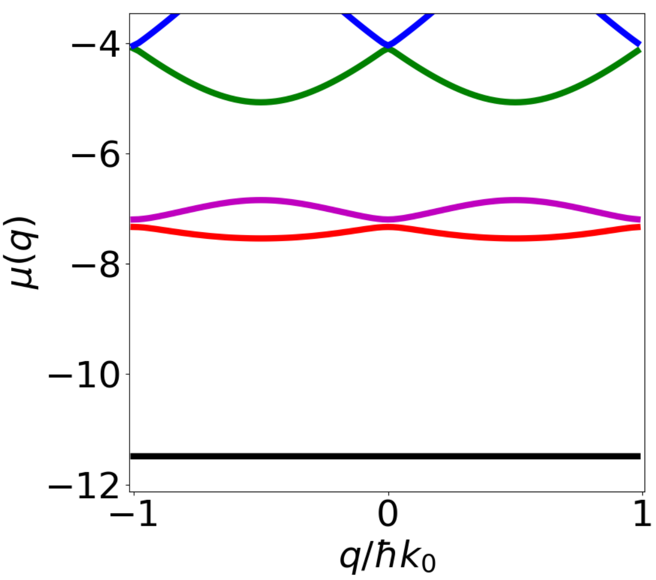

Figure 4.4: The linear energy spectrum of the lowest four energy bands of the one-dimensional potential shown in Fig. 4.2(a)

the $q_{\pm} = (\hbar k_0/2, -\hbar k_0/2)$ points where a cold bosonic system loaded into this band will condense.

The Bloch states $\psi_{q\pm}$ in the real-space associated with the two minima occur at $q_{\pm} = (\hbar k_0/2, -\hbar k_0/2)$ of the second energy band are shown in Fig. 4.5. They show symmetric and anti-symmetric hybridized wavefunction. In another word, their wave functions are a superposition of the local symmetric function at the shallow lattice sites and anti-symmetric function at the deeper wells (shaded strips), i.e $\psi_{q\pm} = \sqrt{n_s}\phi_s + \sqrt{n_q}\phi_{q\pm}$. This hybridization occurs because the energy level of the symmetric wavefunction in the shallow sites is tuned to the energy level of the asymmetric wavefunction in the deep sites, and thus a hybridized wave function is formed as shown in Fig. 4.5.

4.1.2 Two-dimensional band-gap structure

In the 2D lattice potential, the condensate wavefunction is described by the 2D GPE:

$$i\frac{\partial \psi}{\partial t} = -\nabla_{\perp}^2 + V(x,y)\psi + \sigma|\psi|^2\psi \tag{4.7}$$

where $\nabla_{\perp}^2 = \partial^2/\partial x^2 + \partial^2/\partial y^2$ and $V(x,y)$ is a 2D optical lattice potential. The steady state solution of Eq.(4.7) is described by $\psi(x,y) = \phi(x,y)e^{-i\mu t}$, where μ is the chemical

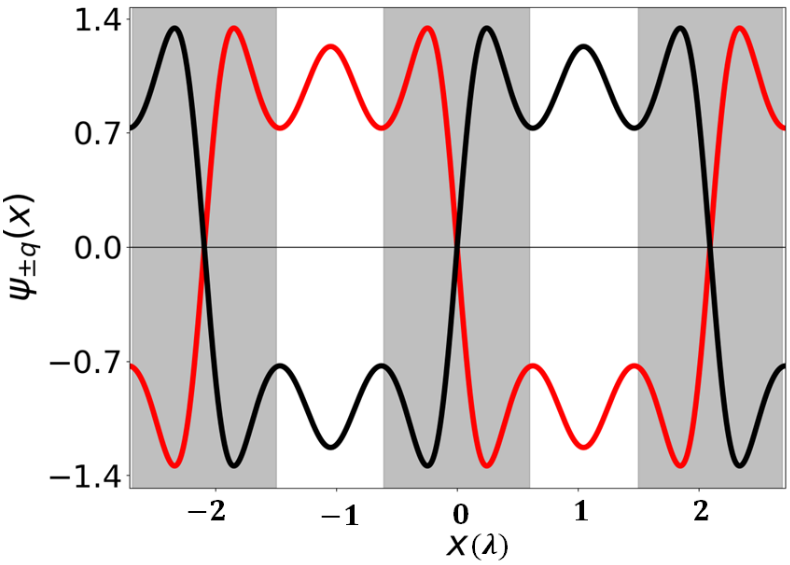

Figure 4.5: The real space Bloch function of the second energy band at points $q_+ = \hbar k_0/2$ (red solid line), $q_- = -\hbar k_0/2$ (black solid line) with $V_0 = 5.7E_r, \theta = 0.43\pi$. It shows a symmetric function in the shallow lattice sites and an anti-symmetric function in the deep lattice sites shown as shaded vertical strips.

potential and the spatial wave function $\phi(x, y)$ satisfy:

$$\Big(-\nabla_\perp^2 + V(x, y)\Big)\phi + \sigma|\phi|^2\phi = \mu\phi. \tag{4.8}$$

For the non-interacting case $\sigma = 0$, the solutions of Eq.(4.8) $\phi(r)$ can be defined by Bloch waves

$$\phi_q^n(r) = u_q^n(r)e^{iq.r}, \tag{4.9}$$

where $u_q(r) = u_q(r + a)$ is a periodic function with the periodicity of the lattice. For the quasi-momentum q within the n^{th} Brillouin zone of the square optical potential, the dispersion relation for the 2D Bloch waves, $\mu^n(q)$, is obtained by solving a system of linear equations

$$(-i\nabla + q)^2 u_q^n - V(x, y)u_q^n = \mu^n(q)u_q^n \tag{4.10}$$

where $\mu^n(q)$ is the set of linear eigenvalues characterized by band-gap structure. Again, the Schrodinger equation Eq.(4.10) can be re-written in matrix form with the diagonal matrix elements as

$$< q + G_{(m,n)}|H_0|q + G_{(m,n)} >= (q - G)^2$$

where $G_{(m,n)} = mb_1 + nb_2$ are the reciprocal lattice vectors with real space basis vectors $b_{1,2} = (\pm k_0/2, k_0/2)$ and m,n are integers. For the 2D bipartite potential given by Eq.

(4.4), The non-zero off-diagonal matrix elements read

$$V_{n,m} = \begin{cases} -\frac{V_0}{2}\cos(\theta) & n,m = [\pm 1, 0], [0, \pm 1]] \\ -\frac{V_0}{4} & n,m = [\pm 1, \pm 1], [\mp 1, \mp 1], \end{cases}$$

A quasi-momentum representation of the first excited state in the 2D reciprocal space is shown in Fig. 4.6. It has four minima shown in blue.

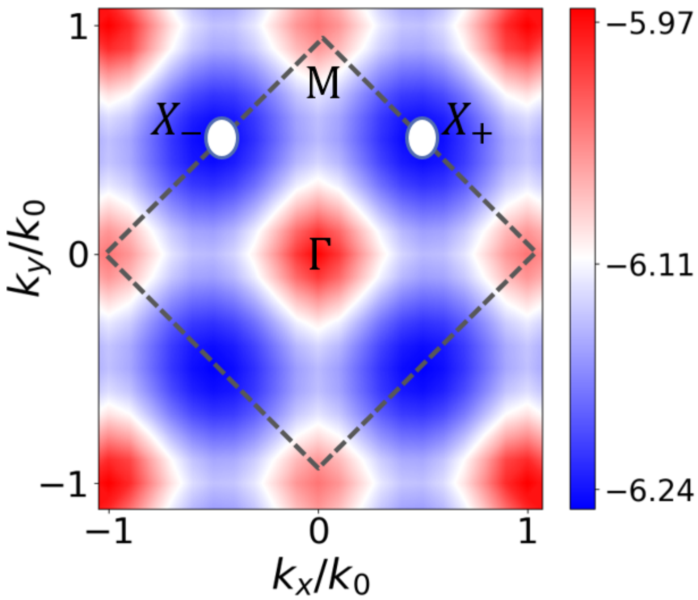

Figure 4.6: Momentum representation for the first excited state in momentum space of the 2D bipartite lattice potential given by Eq. (4.4). Two degenerate band minima are formed in the points $X_\pm$. The dashed lines enclose the first Brillouin zone

A more informative representation for the lowest four energy eigenvalues $\mu(q)$ is shown in Fig. 4.7, along the path connecting the high symmetry points in the reciprocal space $(M(k_0, k_0) \rightarrow X_-(k_0/2, -k_0/2) \rightarrow \Gamma(0,0) \rightarrow X_+(k_0/2, k_0/2) \rightarrow M(k_0, k_0))$ of the FBZ. The first excited state (orange line Fig. 4.7) is characterized by two degenerate minima at $X_\pm = (k_0/2, \pm k_0/2)$ in the FBZ where cold atoms will reside. The shaded areas correspond to the complete bandgaps where the localized states solution of Eq. (4.8) exists (more details will be discussed in chapter 5).

In agreement with the experimental observation, the real-space distribution of the Bloch states corresponding to the point $X_\pm$ $\phi_{X_\pm}$ manifest a $s-p$ hybridized nature with a local phase of $\pm\pi$ as shown in Fig .4.8.

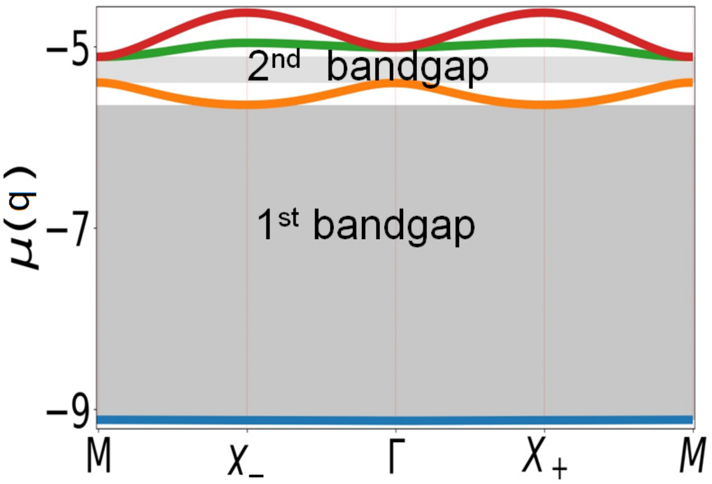

Figure 4.7: Dispersion diagram for a 2D bipartite square lattice in Fig. 4.2(b) ($V_0 = 5.7$, $\theta = 0.43\pi$). The lowest four energy eigenvalues $\mu(q)$ are shown along the path connecting the high symmetry points in the reciprocal space. The shaded areas represent the open bandgaps where the localized solutions exist (discussed in the next chapter).

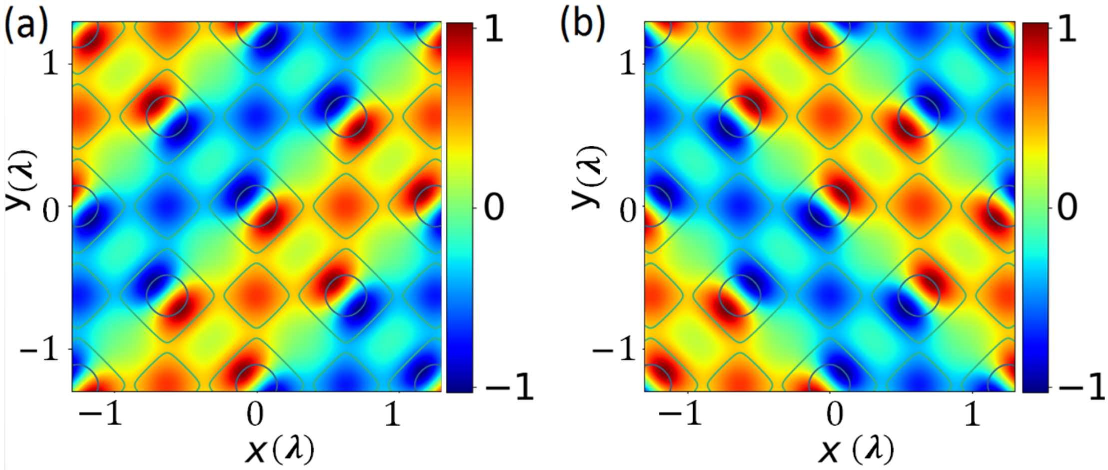

Figure 4.8: The real space structure of the 2D Bloch waves associated with the points (a) X_+, (b) X_-, comprise of local s-and p-orbitals with a local amplitude $\pm\pi$. The color bar represents the peak height of the wavefunction $\psi_{X_\pm}$.

The wave functions 4.8 exhibit superposition of the local s- orbital at the shallow site and the p- orbital with its two peaks residing in the deep B sites. This can be explained as follows: for $\theta = 0.43\pi$, a system is created where the s- orbitals of the shallow lattice site (A sites) are in tune with the p-orbitals of the deep wells (B sites). Consequently, the s-band is hybridized with the p-band [77]. They show striped superfluid orders with different orientations. Due to the lattice symmetry, the Bloch mode at the point (X_-) is a $\pi/2$ rotated of the Bloch mode at the point (X_+) as shown in Fig. 4.8.

Up to this point, we have studied the linear limit of the GPE (4.5) with 1D & 2D bipartite optical potential shown in Fig. 4.2. The linear band-gap structure and the Bloch modes in the case of the 1D and 2D potential were investigated. In what follows, we use our knowledge about the first excited energy band and the associated Bloch states to analyze the steady-state solutions of a weakly interacting condensate loaded into the bipartite lattice potential. For this purpose we use the concepts of nonlinear guided-wave optics [96] to study the coupling between the two modes formed at the two degenerate minima of the first excited state of the bipartite lattice potential given in Eqs. (4.2), (4.4). This approach was developed to analyze the coupling between the BEC ground-state mode and the first excited mode in a double-well potential [94, 95].

4.2 Nonlinear dynamics

A general formulation of the coupled-mode theory for an interacting condensate in an optical lattice potential with a double-well dispersion is presented at the beginning of this section. Implementations in the 1D and 2D bipartite optical lattice potential shown in Fig. 4.2 are then demonstrated.

Coupled-mode theory

For an ideal non-interacting gas limit of Eq. (4.1), the exact stationary solutions are given in the form $\psi(r,t) = \phi(r)e^{i\mu_j t}$, with μ_j are set of linear eigenvalues associated with linear eigenstate. In the nonlinear case $\sigma \neq 0$, the concept of eigenmodes is still valid, which are described by a set of localized solutions [94].

To formulate the coupled-mode theory, we assume a weakly interacting BEC loaded into an energy band with two degenerate minima labeled by l_+, l_-. This degeneracy enables the condensed wavefunction to be expressed as a superposition of the two degenerate Bloch modes $\psi_{l_\pm}(r)$:

$$\psi(r,t) = C_{l_+}(t)e^{-i\mu_{l_+}t}\psi_{l_+}(r) + C_{l_-}(t)e^{-i\mu_{l_-}t}\psi_{l_-}(r) \tag{4.11}$$

with complex time varying amplitudes $C_{l_\pm}(t)$ correspond to the Bloch states $\psi_{l_\pm}(r)$ respectively. Substituting ansatz (4.11) into the GP equation (4.1), then multiplying by $\psi_{l_\pm}$ and integrating over the spatial variable. We obtain the system of coupled-mode equations for the time-varying amplitudes $C_{l_\pm}$.

$$\begin{aligned} i\frac{\partial C_{l_\pm}}{\partial t} &= \sigma\gamma_{l_\pm l_\pm}|C_{l_\pm}|^2 C_{l_\pm} + \sigma\gamma_{l_- l_+}(|C_{l_\pm}|^2 C_{l_\pm} \\ &\quad + C_{l_\pm}^2 C_{l_\pm}^* e^{2i(\mu_{l_-}-\mu_{l_+})t}), \end{aligned} \tag{4.12}$$

where $\gamma_{ij} = \int dr\psi_i^2(r)\psi_j^2(r)/N_{ij}$ is the set of the overlap integrals between the Bloch states $\psi_i(r)$ and $\psi_j(r)$ with $N_{ij} = \int dr\psi_i^*(r)\psi_j(r)$. The solution of the above dynamical equations can be studied by solving the rate equations for the amplitudes $C_{l_\pm}$. For convenience, the complex amplitudes $C_{l_\pm}$ are separated into an amplitude $\sqrt{N_{l_\pm}}$ proportional to density and phase $\theta_{l_\pm}$ ($C_{l_\pm} = \sqrt{N_{l_\pm}}(t)e^{i\theta_{l_\pm}t}$).

To understand the system dynamics, new physical parameters are introduced: the relative populations of the two modes $\Delta N = N_{l_+} - N_{l_-}/(N_{l_+} + N_{l_-})$, where $N = (N_{l_+} + N_{l_-})$ and the relative phase $\Theta = \theta_{l_+} - \theta_{l_-}$. In terms of $\Delta N(t)$ and $\Theta(t)$ the coupled mode equations (4.12) become,

$$\begin{aligned} \frac{\partial \Delta N(t)}{\partial t} &= \sigma\gamma_{l_- l_+}(1-\Delta N^2)\sin(2\Theta) - \eta\Delta N, \\ \frac{\partial \Theta(t)}{\partial t} &= \delta + \sigma\Delta N((\gamma_{l_+ l_+} - \gamma_{l_- l_-}) - 2\gamma_{l_- l_+}(2+\cos(2\Theta))), \end{aligned} \tag{4.13}$$

where, $\delta = (\mu_{l_-} - \mu_{l_+})$ quantifies the detuning between the two modes. In this system of coupled equations, a linear dissipative term ($\eta\Delta N$) is introduced which represents the finite life time due to two body collisions [95]. The dynamics described by Eqs. (4.13) depend on the values of the overlap integrals $\gamma_{l_\pm, l_\pm}$ and γ_{l_-, l_+} which are determined by integration over the Bloch modes profiles $\psi_{l_\pm}(r)$. The fixed points of the dynamical system (4.13) can be determined by setting their time derivatives equal to zero, at $\eta = 0$ one can obtain

$$\begin{aligned} \Delta N_c &= \frac{\delta\sigma}{(\gamma_{l_+ l_+} + \gamma_{l_- l_-}) - 6\gamma_{l_- l_+}} \\ \Theta &= n\pi/2, \qquad\qquad n = 0, 1, 3... \end{aligned} \tag{4.14}$$

It is worthy mentioning that, the system (4.13) also can be represented in a canonical form

$$\frac{d\Delta N}{dt} = \frac{\partial H}{\partial \Theta}, \qquad \frac{d\Theta}{dt} = \frac{\partial H}{\partial \Delta N},$$

where the Hamiltonian H is given by

$$H = \sigma\gamma_{l_-l_+}(1-\Delta N^2)\cos(2\Theta) + \delta\Delta N + \sigma((\gamma_{l_+l_+} - \gamma_{l_-l_-})/2 + 2\gamma_{l_-l_+})\Delta N^2,$$

The dynamics of population imbalance and the relative phase can be investigated through the phase space portrait $(\Delta N, \Theta)$, which shows the possible fixed point solutions of a physical system.

4.2.1 The dynamics of population imbalance and relative phase between the two degenerate modes of the 1D bipartite potential.

The existing approach can be applied to the 1D double period potential shown in Fig. 4.2(a). Since the band-gap structure shows that the first excited state (red line in Fig. 4.4) has two degenerate minima at $q = \pm k_0/2$, the condensed wavefunction can be written as a sum of the two degenerate Bloch modes $\psi_{q\pm}(x)$:

$$\psi(x,t) = \sqrt{N_{q_+}}(t)e^{-i(\mu_{q_+}+\theta_{q_+})t}\psi_{q_+}(x) + \sqrt{N_{q_-}}(t)e^{-i(\mu_{q_-}+\theta_{q_-})t}\psi_{q_-}(x).$$

The overlap integrals γ_{ij} $(i,j = q_\pm)$ between the two degenerate Bloch modes $\psi_{q\pm}$ with the spatial structure shown in Fig. 4.5 are calculated.

For $\gamma_{q_+q_-} \sim 0.7\gamma_{q_+q_+(q_-q_-)}$, the phase space portrait Fig. 4.9, shows the fixed point solutions of the interacting condensate in the first excited state of the 1D bipartite optical potential. The numerical solution reveals that there are three fixed states of the relative population: $\Delta N = 0$, which corresponds $N_{q_+} = N_{q_-} = N/2$ with a relative phase difference between the two modes $\Theta = 0, \pm\pi/2$ (red circles in Fig. 4.9).

By introducing a small dissipative parameter $\eta \neq 0$, we found that for arbitrary initial conditions, the points $(\Delta N, \Theta) = 0, \pm\pi/2$ form a steady state solution for the system as shown in Fig. 4.10. Therefore, the steady-state solution for an interacting condensate in the first energy band of the 1D bipartite optical potential shown in Fig. 4.2(a) can be expressed as a superposition of the Bloch modes $\psi_{q\pm}$ with equal amplitudes and a fixed phase of $\pm\pi/2$ $(\psi_{1D} = \psi_{q_+} + e^{i\pi/2}\psi_{q_-})$ [97].

The density distribution of the superposition state ψ_{1D} and the phase structure are shown in Fig. 4.11. The asymmetric wavefunctions are destructively interfering, which

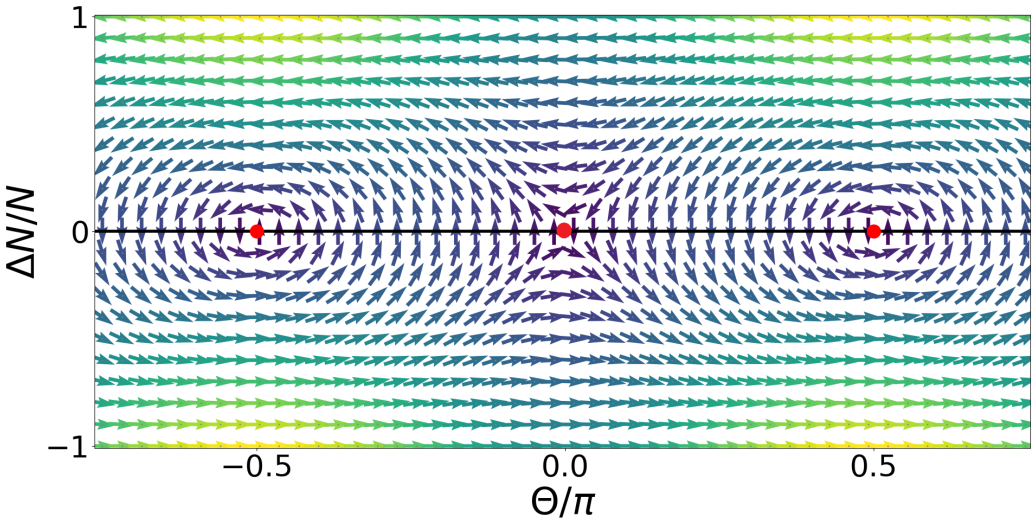

Figure 4.9: The phase portraits of the population imbalance $\Delta N/N$ and phase difference Θ for the system of the coupled-mode equations (4.13) with overlapping integral $\gamma_{q_+q_-} \sim 0.7\gamma_{q_+q_+(q_-q_-)}$ calculated between the two modes shown in Fig. 4.5. The red dots represent the fixed-point solutions.

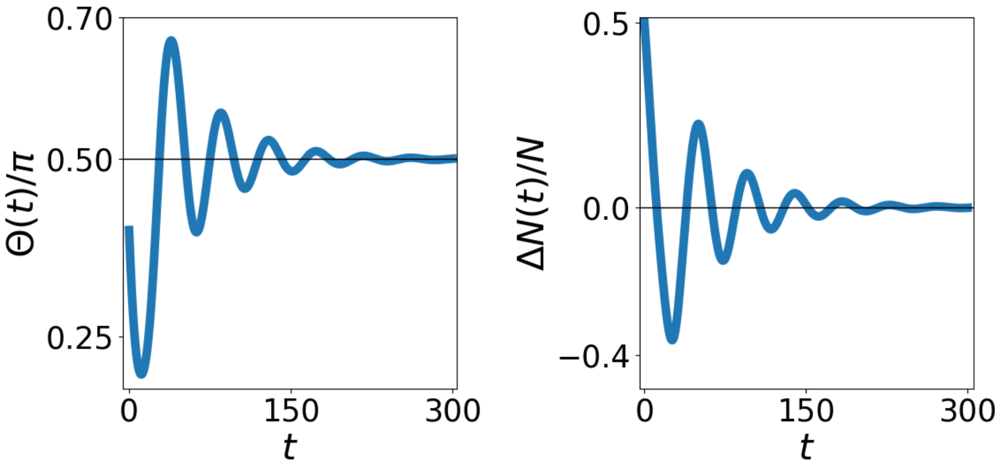

Figure 4.10: The evolution of the phase difference Θ and population imbalance ΔN.

results in a dip formed in the deep lattice sites. In the shallow lattice sites, the symmetric wavefunctions are arranged with alternating phase $\pi/2$ and $-\pi/2$ between the neighbor sites.

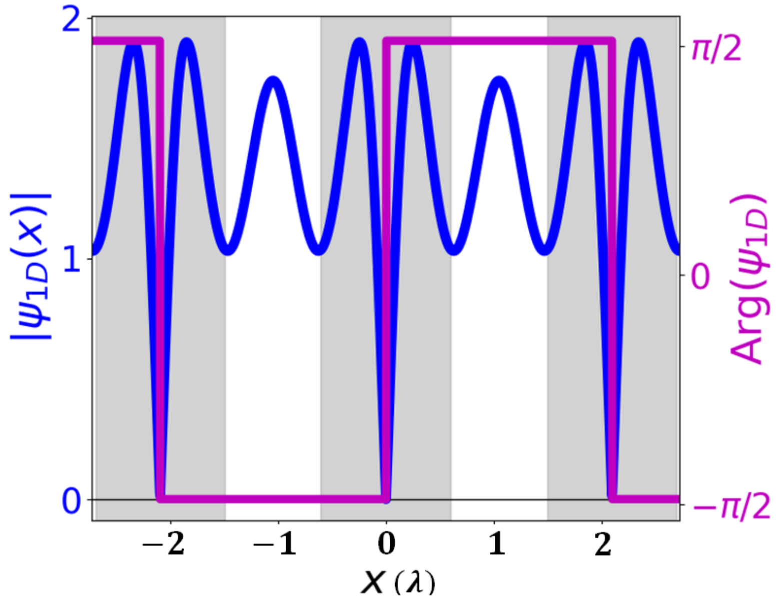

Figure 4.11: The density distribution (solid red line) and the phase structure (dashed blue line) of the steady state formed in the 1^{st} *excited band of the 1D bipartite potential.*

4.2.2 The dynamics of population imbalance and relative phase between the two degenerate modes of the 2D bipartite potential.

To examine the dynamics of interacting condensate in the second band of the 2D bipartite optical lattice potential shown in Fig. 4.2(b), the phase space portrait $(\Delta N, \Theta)$ is visualized in Fig. 4.12. For isotropic limit $\epsilon = 1$, the first excited state (orange line in Fig. 4.7) exhibits two degenerate minima at $X_{\pm}$, i.e $\delta = 0$ $(\mu_{X_+} = \mu_{X_-})$, allowing us to describe the wavefunction as a sum of the two degenerate Bloch modes $\psi_{X_{\pm}}$

$$\psi(r,t) = \sqrt{N_{X_+}}(t)e^{-i(\mu_{X_+}+\theta_{X_+})t}\psi_{X_+}(r) + \sqrt{N_{X_-}}(t)e^{-i(\mu_{X_-}+\theta_{X_-})t}\psi_{X_-}(r).$$

In this case, for $\gamma_{X_+X_-} \sim 0.55\gamma_{X_+X_+(X_-X_-)}$, the phase space plane reveals the existence of fixed point solutions lying at the line $\Delta N = 0$ and phase shift of $\Theta = 0, \pm\pi/2$ (red circles in Fig. 4.12). In the isotropic case $\epsilon = 0$, the two modes $\psi_{X_{\pm}}$ are degenerate or quasi-degenerate (i.e $\delta = 0$), one can safely assume that population imbalance is relatively small $|\Delta N| \ll 1$. And thus the steady states of the system (4.13) are found under conditions of equal modes populations $\Delta N = 0$ (i.e $N_{X_-} = N_{X_+}$) with locked relative phase $\Theta = \pm\pi/2$.

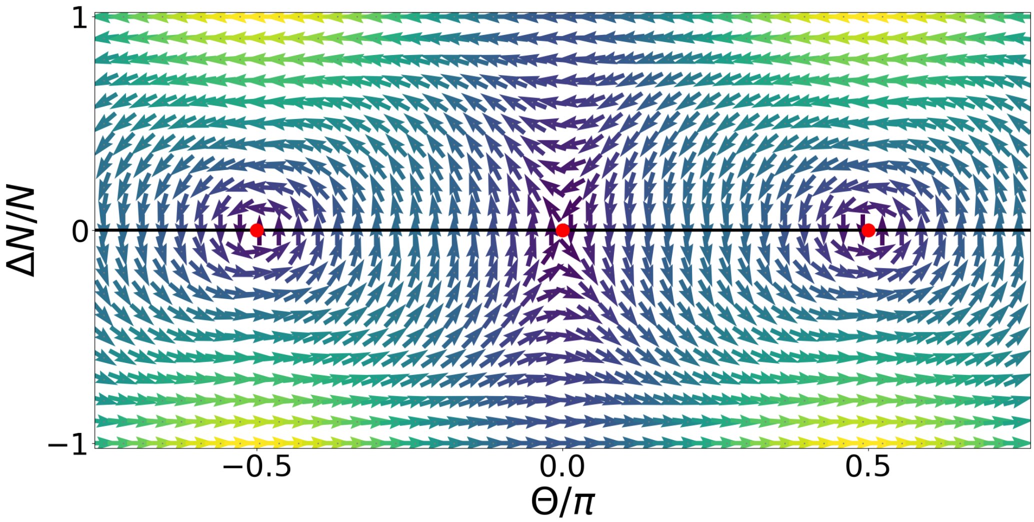

Figure 4.12: The phase portraits of the population imbalance $\Delta N/N$ and phase difference Θ for the system of the coupled-mode equations (4.13) with overlapping integral $\gamma_{X_+X_-} \sim 0.55\gamma_{X_+X_+(X_-X_-)}$ calculated between the two modes shown in Fig. 4.8. The red dots represent the fixed-point solutions.

To prove this the time evolution of the relative phase Θ and the population imbalance ΔN are plotted in the dissipative case $\eta \neq 0$. The system forms a steady state solution at $(\Delta N, \Theta) = (0, \pi/2)$ as shown in Fig. 4.13.

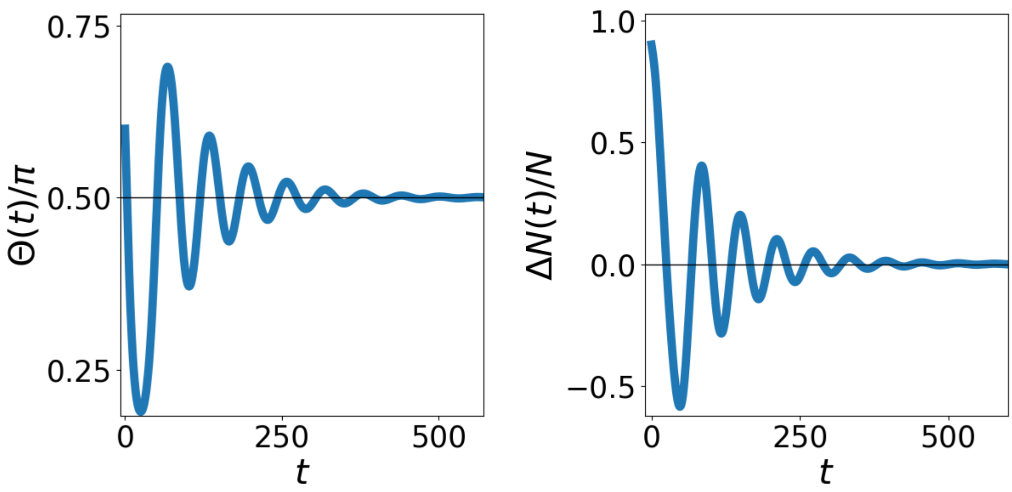

Figure 4.13: The evolution of the phase difference Θ and population imbalance ΔN.

Knowing the steady state solution coordinates $(\Delta N, \Theta)$ the stable solution for our system can be constructed. The superposition of the two degenerate Bloch modes $\psi_{X_\pm}$ with equal amplitudes and a fixed phase of $\pi/2$ results in sequence of 2D vortices such as $\psi_{2D} = (\psi_{X_-} + e^{i\pi/2}\psi_{X_+})$.

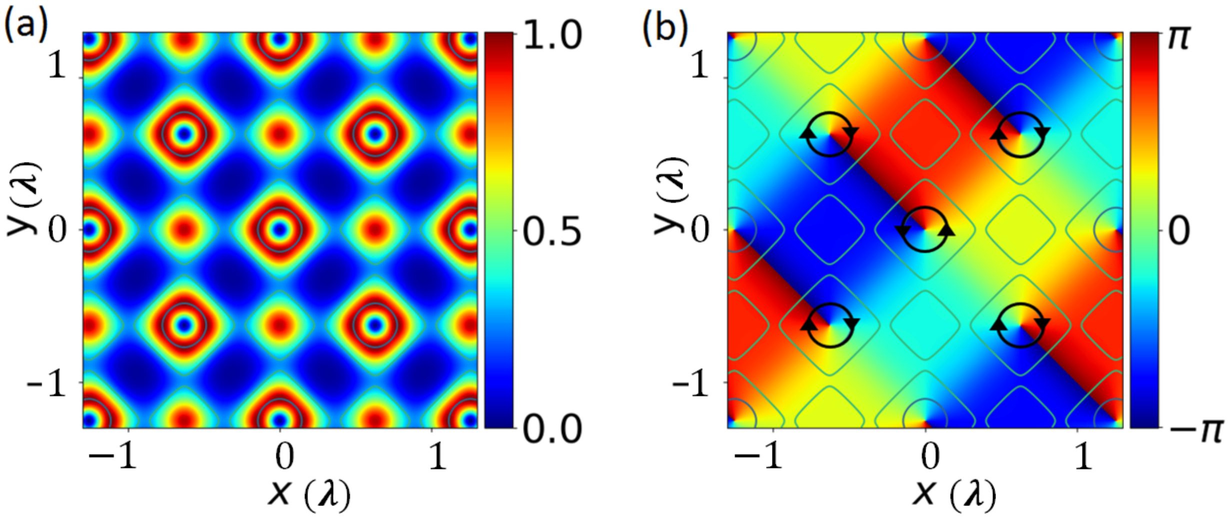

Figure 4.14: (a) The density distribution of the steady state solution $|(\psi_X + e^{i\pi/2}\psi_{-X})|^2$ *for the 2D bipartite optical lattice. (b) The phase structure with black arrows represents the circulation of each vortex.*

The density distribution of the state ψ_s is shown in Fig. 4.14(a). A 2D array of vortices is formed at the deep lattice sites. The phase relations between the s-orbitals at neighboring sites are arranged such that a complete 2π phase is formed around the center of each vortex as shown in Fig. 4.14 (b). By performing the integration (3.10) over the FBZ, one can conclude that the system possesses an angular momentum $L = \pm\hbar$. This unconventional state spontaneously breaks the TR symmetry [89, 90]. The physics of this state is similar to Hund's rule for electronic configuration [79]: the paired state $\psi_{X_-} + i\psi_{X_+}$ is energetically favored since the chiral superposition occupies large volume and thus the repulsive interacting particle can avoid each other.

In the anisotropic situation, where $\epsilon > 0$, the degeneracy between the two minima at $X_\pm$ disappears, and the solution of the coupled system of equations (4.13) displays two fixed points moving up towards the line $\Delta N \to 1$, as illustrated in Fig. 4.15. For $\epsilon = 0.07$ the fixed point solutions occur at $(\Delta N, \Theta) = (\sim 0.6, \pm 0.55\pi)$.

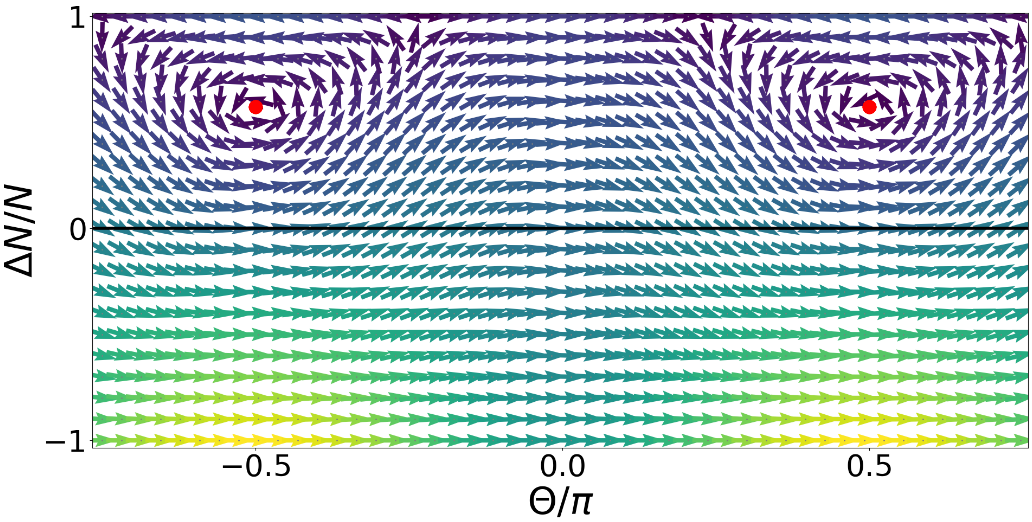

Figure 4.15: For anisotropic case, $\epsilon = 0.07$, the phase space portrait $(\Delta N, \Theta)$ with two fixed point solutions at $\Delta N, \Theta = (0.66, \pm 0.55\pi)$ denoted by red circles.

The time evolution of the population imbalance and the relative phase, in this case, is shown in Fig. 4.16. Fig. 4.17 depicts the density distribution and the phase structure of the superposition state corresponding to $\epsilon = 0.07$. In this case, the density is not distributed uniformly around the center of the deep lattice sites. However, the phase structure still shows an array of vortices formed at the deep lattice sites (see Fig. 4.17 (b)).

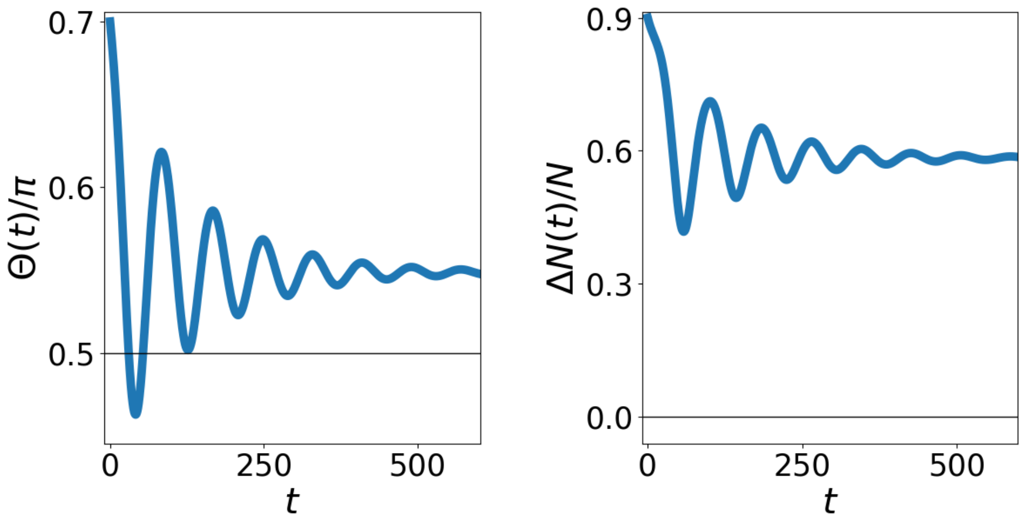

Figure 4.16: The evolution of the phase difference Θ and population imbalance ΔN for non degenerate case $\epsilon = 0.07$.

Our calculations show that the solution $|(\sqrt{N_{X_+}}\psi_X + \sqrt{N_{X_-}}e^{i0.55\pi}\psi_{-X})|^2$ has an angular momentum of $0.63\hbar$, which indicates that the angular momentum formed in the degenerate state gradually vanishes as the lattice anisotropy increases. It is worth pointing out that for the far detuning ($\delta >> 0$) limit, the system forms a striped state (see Fig. 4.18), which implies that the condensate resides on single minima.

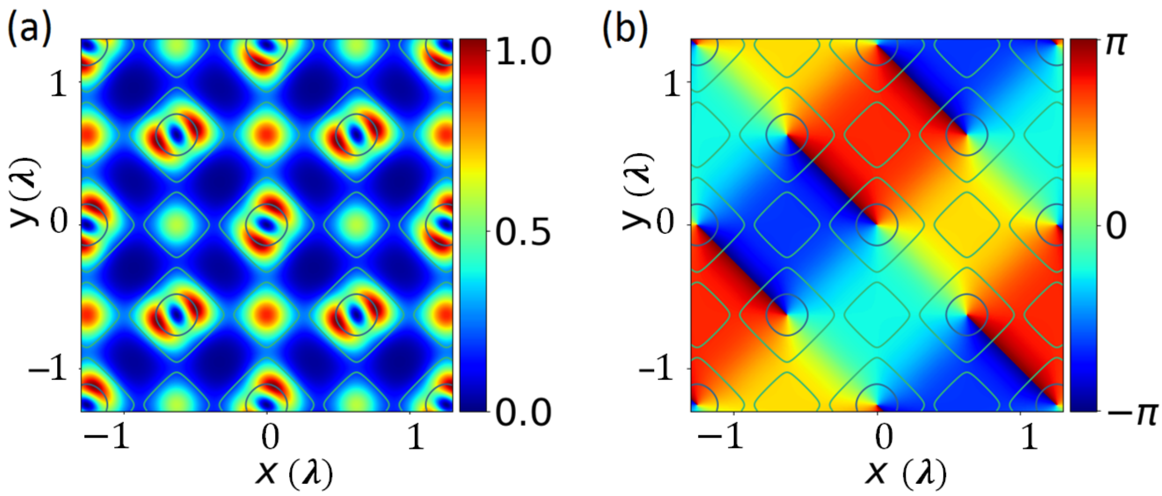

Figure 4.17: (a) The density distribution of the steady state solution given in figure 4.16 $|(\sqrt{N_{X_+}}\psi_X + \sqrt{N_{X_-}}e^{i0.55\pi}\psi_{-X})|^2$. (b) The phase structure.

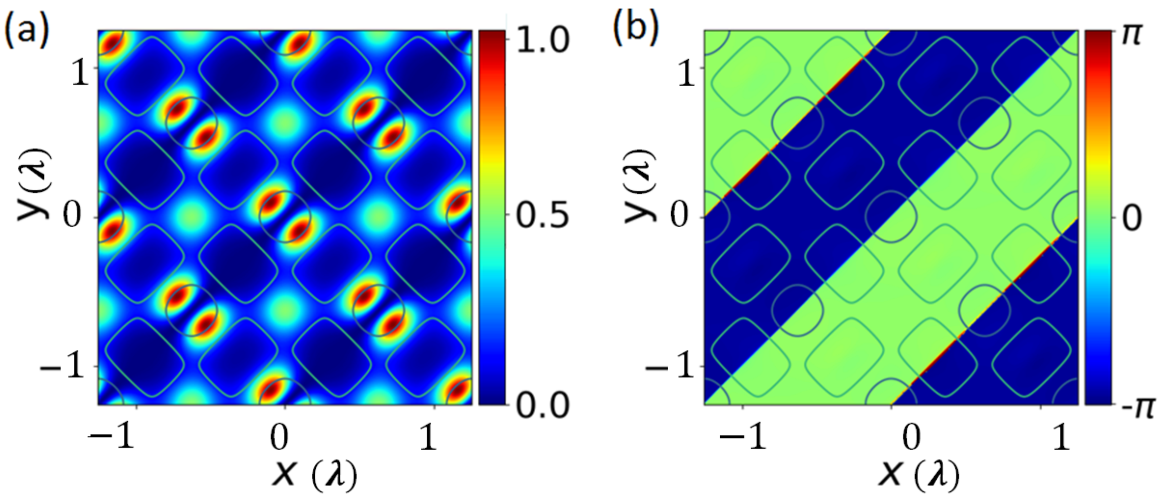

Figure 4.18: (a) The density distribution of the steady state solution for the far detuned limit $\delta >> 0$. (b) The phase structure.

4.3 Summary and conclusion

In this work, we employed the coupled-mode theory to investigate the dynamics of an interacting condensate in the second band of the isotropic 1D & 2D bipartite optical lattice. The standard eigenvalue problem is solved or both cases, followed by the formulation of the coupled-mode approach in a double-well dispersion. Based on the coupled mode formalism, the steady state of weakly interacting bosons in a (two)-dimensional bipartite lattice with double degenerate minima is established.

For the isotropic case $\epsilon = 1$, we show that the first excited state is formed with two inequivalent degenerate energy minima at the edge of the FBZ. A cloud of cold atoms loaded into this energy band will fragment into two degenerate components at $q_\pm$ in 1D lattice and $X_\pm$ in 2D optical potential.

In the anisotropic case, the Bloch states of the second energy band are characterized by a striped structure with local phase $\pm\pi$.

The coupled mode theory is an important approach to analyze the steady state of an interacting condensate in a double-well potential and provides numerical analysis for the non-stationary GP equation.

Gap soliton is a nonlinear state that resides in a complete gap of the linear band spectrum. In the next chapter, we numerically study the solitary solution of the GPE corresponding to the open bandgap (shaded areas) shown in Fig. 4.7.

This page intentionally left blank.

Chapter 5

Nonlinear localization of BEC in a square bipartite optical lattice.

Nonlinear localization of BEC in 2D-dimensional lattices is analogous to the study of self-trapped modes of light waves in nonlinear photonic crystals [98]. Tunability of the optical lattice potential with nonlinear coherent matter waves offers a tool to understand localization in nonlinear systems.

In this chapter, we numerically investigate the bifurcation of gap solitons from the edges of the p-band of the two-dimensional bipartite optical lattice shown in Fig. 4.2(b).

5.1 Gap soliton

Nonlinear photonic band-gap structures provide a unique tool for controlling coherent light propagation and localization. With Kerr nonlinearity, they can support self-trapped localized states of the electromagnetic field in the form of optical gap solitons. Novel integrated photonic devices are being developed as a result of twisting light and localization in nonlinear photonic band-gap structures [98, 99].

Another physical realization of nonlinear wave in a periodic structure is Bose-Einstein condensates (BECs) in optical lattice potentials. Optical lattices are characterized by a band-gap structure, which alters the diffraction properties of matter wave [100].

As shown in the previous chapter, in the linear limit ($\sigma = 0$), the periodicity of the optical lattice potentials induces a band-gap-like structure. These bands are associated with linear propagating modes called Bloch modes. On the other hand, due to the interplay between the lattice's periodicity and inter-particle interactions ($\sigma \neq 0$), nonlinear self-trapped localized modes can arise, known as lattice solitons. When $\sigma > 0$ the nonlinearity is of a self-focusing type (attractive interaction), while when $\sigma < 0$, the nonlinearity is of a self-defocusing type (repulsive interaction). A particular type of soliton is a gap-lattice soliton that resides in the band gap. The existence of such states in the gaps can be explained by using the Bloch-wave envelope approximation near the band edge where the diffraction coefficient $D = \partial^2\mu(k)/\partial k^2$ for a coherent wave depends on the curvature of the band that edge. The diffraction coefficient D can be both negative (anomalous, $D < 0$) and positive (normal, $D > 0$) which balances the interaction sign and leads to the formation of nonlinear localization with zero group velocity in BEC with attractive and repulsive interactions [101].

Both nonlinear matter-wave dynamics and nonlinear photonic crystals can be modeled based on the nonlinear Schrodinger equation (NLSE), which is used to describe both the BEC order parameter and the envelope of the electromagnetic field.

In the context of BECs, gap solitons are localized states that exist in an open bandgap of a linear spectrum of an optical lattice potential. The power of a solitary wave can be defined in terms of the norm of the wavefunction ϕ, $P = \int |\phi(x, y)|^2 dxdy$, which measures the number of atoms in the localized state. A sech-like envelope of the corresponding Bloch wave well approximates the gap soliton of a repulsive and attractive BEC [101].

Theoretically, gap solitons often bifurcate from the Bloch-band edges into the band gaps with increasing power P as the chemical potential moves inside the band gap such as vortex and reduced symmetry solitons [102, 103]. It has been noted that some gap solitons do not bifurcate from the edges of Bloch bands possessing a power curve with multiple branches without touching the band edge [104, 105]. These localized structures have been intensively investigated in several nonlinear periodic systems. For instance, semiconductor microcavities [106], and BEC in optical lattices [107]. Furthermore, gap solitons in BEC enable us to address a wide range of interesting physics, such as the chirality of topological gap solitons [108], a spin-dependent parity symmetry gap soliton [109], multipole and half-vortex gap solitons [110], and dark gap solitons in exciton-polariton condensates [111, 112].

Solitary waves can be numerically computed using iterative numerical methods [113]. Numerical solutions show solitary waves are strongly localized far away from the band edge for a sufficiently wide gap and weakly localized (i.e. spread over several lattice sites) near the band edge [114]. The nonlinear localized states are observed when the lattice possesses a full bandgap, which can be achieved in a relatively deep potential. This requirement is observed in the linear dispersion shown in Fig.4.7 that it possesses a complete bandgap at $-9.25 < \mu(q) \leq -5.72$ (first bandgap) and $-5.4 < \mu(q) \leq -5.25$ (second bandgap). Interestingly, the second energy band hosts two degenerate independent Bloch modes at the points X, X' in the isotropic case which may lead to a solitary wave with a rich phase structure. Moreover, a single Bloch mode is possible in the non-degenerate case, which can be realized in the anisotropic lattice by adjusting $\epsilon < 1$.

This work continues investigating the dynamics of an interacting BEC loaded into the p-band of the 2D bipartite lattice potential shown in Fig. 4.2(b). In what follows, we solve the nonlinear GPE in Eq. (4.8) for the given 2D bipartite potential numerically over the first and the second bandgaps shown in Fig. 4.7, searching for a gap soliton bifurcates from the edges of second Bloch band. To find the soliton solution, the 2D GPE with focusing and defocusing nonlinearity is solved numerically by the Newton-conjugate-gradient method [113] for the 2D bipartite optical potential in (4.4) with $V_0 = 5.7$ and $\theta = 0.43\pi$.

Newton-conjugate-gradient method

Newton-conjugate-gradient (NCG) methods are numerical algorithms used to compute solitary waves, which are solutions to nonlinear partial differential equations that exhibit localized long-lasting wave behavior [115], such as the nonlinear Schrödinger equation or the Korteweg-de Vries equation. NCG methods combine the Newton method for finding roots of nonlinear equations with the conjugate gradient method for solving linear systems. The resulting algorithm can effectively find solitary waves with high accuracy by iteratively improving solutions. The convergence of NCG methods for solitary wave computations can be influenced by various factors, including the choice of initial guess, the size of the time-step used, and the accuracy of the linear solver used in the algorithm.

The NCG method involves an iterative procedure where an initial guess for the solution is updated using the gradient of the function. The gradient provides information about the direction of the steepest descent. The converges can occur relatively faster compared to other iterative methods [113] for both the ground and excited states of a nonlinear wave system.

Consider a real-valued nonlinear wave system in arbitrary spatial dimensions, which can be written in the following form:

$$h_0 u(x) = 0 \tag{5.1}$$

where $u(x)$ is a vector of unknowns and h_0 is a nonlinear operator, which for instance in the GPE,

$$i\frac{\partial}{\partial t} + \frac{\partial^2}{\partial x^2} + |u|^2 = 0. \tag{5.2}$$

The main goal is to solve solitary waves in Eq. (5.1) by iteration methods. Assume that $u_k(x)$ is an approximate solution that is close to the exact solution $u(x)$. The next iteration solution $u_{k+1}(x)$ can be expressed as

$$u_{k+1}(x) = u_k(x) + \Delta u_k(x), \tag{5.3}$$

where $u_k(x) = u(x) + e_k(x)$, with $e_k(x) << 1$ is the error term. Substitute this expression into (5.1) and expand it around $u_k(x)$, which gives

$$h_0 u_k(x) + h_{1k} e_k = O(e_k^2). \tag{5.4}$$

Here h_{1k} is the linearization operator of the solitary wave Eq. (5.1). The NCG method iteratively updates the approximation u_k to the solution u, by finding a search direction p_k and updating the approximation using a step size α_k:

$$u_{k+1} = u_k + \alpha_k p_k, \tag{5.5}$$

the search direction p_k is computed using the conjugate gradient method, and the step size α_k is found using the Newton method.

In the conjugate gradient method, the search direction is chosen to be conjugate to the previous search directions, which leads to faster convergence. The search direction p_k is given by:

$$p_k = -M^{-1} h_k u + \beta_k p_{k-1}, \tag{5.6}$$

where M^{-1} is a self-adjoint and positive-definite pre-conditioning operator, and β_k is chosen to ensure conjugacy and is given by:

$$\beta_k = \frac{\langle M^{-1}(h_k u_k)^T, h_k u_k\rangle}{\langle M^{-1}(h_{k-1}u_{k-1})^T, h_{k-1}u_{k-1}\rangle}. \tag{5.7}$$

The Newton-CG method continues until a suitable stopping criterion, such as a prescribed tolerance on the residual or a maximum number of iterations, is satisfied. The method is designed to approximate the true minimum of a given function within a certain user-defined tolerance level. The numerical iterations are terminated when the approximate solution $u_k(x)$ has reached a certain accuracy. This error can be computed by evaluating the M^{-1} weighted norm of the residual vector $R_i = -h_0 u_k - h_{1k}\Delta u_k^i$ in the CG iterations, given by

$$|R_i|_M = \langle R_i, M^{-1}R_i\rangle. \tag{5.8}$$

Then we take the stopping criterion of CG iterations to be

$$|R_i|_M < \epsilon_{cg}|h_0 u_k|_M, \tag{5.9}$$

where ϵ_{cg} is a small positive parameter to limit the CG iterations. In the numerical analysis presented herein, we employ the preconditioning operator $M = c - \nabla^2$, with $c = 1.5$ and $\epsilon_{cg} = 10^{-2}$.

This method can be applied to a wide range of nonlinear wave equations and has been shown to be effective in computing solitary wave solutions with high accuracy and stability. The combination of the conjugate gradient method and the Newton method results in fast convergence and high accuracy in the computation of solitary wave solutions.

5.2 Focusing nonlinearity

The p-band shown in Fig. 4.7 of the 2D bipartite potential in Eq. (4.4) hosts two Bloch modes, which are located at the X and X' points of the first Brillouin zone. They present a $\pi/2$ rotation of each other as shown in Fig. 4.8. These two modes are driven to form of an array of vortices with an interesting phase structure (see Fig. 4.14) in the degenerate case. This suggests that two solutions are possible: single-Bloch-mode solution in the anisotropic case $\epsilon < 1$ and degenerate mode solution in the isotropic case $\epsilon = 1$.

5.2.1 Single-Bloch-mode soliton

In the first bandgap under focusing nonlinearity ($\sigma > 0$), a power curve with three distinct branches that do not touch the lower edge of the second band is shown in Fig. 5.1. For this solution, a single Bloch mode is only considered. The initial guess is taken as the single Bloch state at the point X (ϕ_X) (see Fig. 5.1(a)) modulated by *sech*-like function.

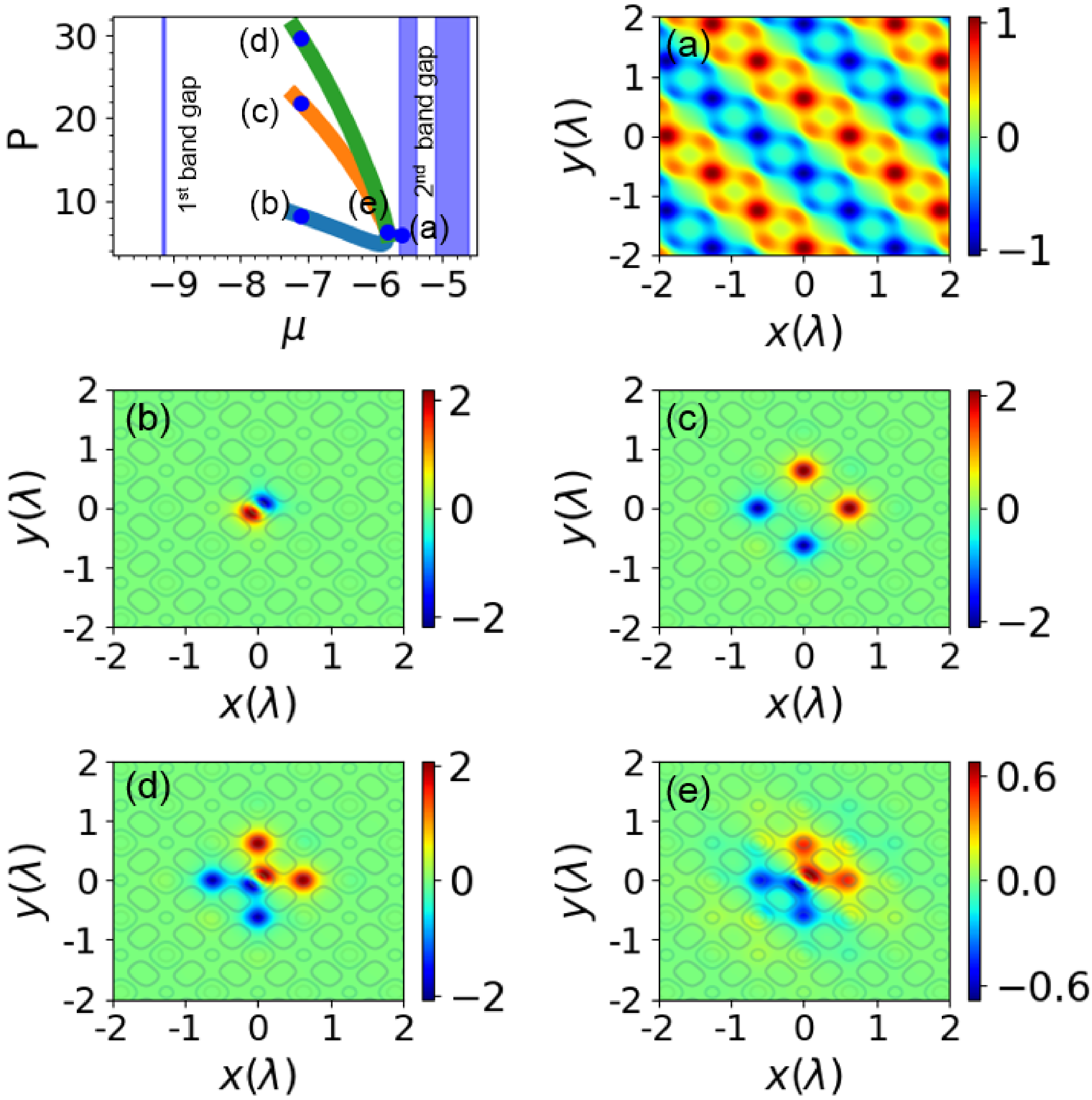

Figure 5.1: The power curve for self-focused gap states in the first bandgap. (a) The spatial structure of the Bloch state at the point X (ϕ_X). The spatial structure of the self-focused gap solitons at the marked points b, c, d corresponds to ($\mu = -7.1$) of the existing power curve. (e) The solitary solution at $\mu = -5.8$ shows the same structure as (d) but less localization. The color bars show the peak-to-peak height of the wave function.

At fixed chemical potential $\mu = -7.1$ in the first bandgap, the spatial structure of the self-focused gap solitons at the marked points (b, c, d) of the existing power curve are shown in Fig. 5.1(b,c,d).

On the low power branch (blue line in Fig. 5.1), a strongly localized soliton is observed away from the band edge. An out-of-phase diagonal dipole soliton with its two peaks residing in the central deep lattice site is found at the point marked by (b) (see Fig. 5.1(b)). For the intermediate power branch (orange line in Fig. 5.1), a gap soliton is comprised of four out-of-phase peaks that are formed in the nearest shallow lattice sites as shown in Fig. 5.1(c). The middle-power branch bifurcates from the high-power branch (green line in Fig. 5.1). On the high-power branch, a less localized gap soliton is formed (see Fig. 5.1(d)). It is comprised of a diagonal out-of-phase dipole soliton in the central deep well superimposed with four peaks in the nearest neighbor shallow lattice sites. In Fig. 5.1(e) the high power soliton solution 5.1(d) is shown near the band edge ($\mu = -5.8$), which is less localized and spreads over several lattice sites.

5.2.2 Degenerate-modes soliton

This soliton solution can be viewed by considering the initial guess as a coherent superposition of two degenerate Bloch modes at $X_\pm$ with $\pi/2$ phase delay ($\psi_{X_+} \pm i\psi_{X_-}$) modulated by *sech*-like function.

The power curve of this solution is shown in Fig. 5.2, it bifurcates from the edge of the second energy band with increasing power as the chemical potential decreases. In the strong localization regime, the vortex state is formed in the deep lattice sites superimposed with four peaks residing at the nearest shallow sites as shown in Fig. 5.2(a) with a phase structure shown in Fig. 5.2(b).

The phase diagram shows that the vortex formed at the central deep lattice site carries a unit topological charge. Forming a vortex soliton in this system implies that this system can be driven from chiral superfluid, where a 2D array of vortices is formed with a global angular momentum (see chapter 4) into the nonlinear localized state, which resides in the first bandgap. This kind of vortex has been realized in a photonic crystal [116] and described theoretically for BEC in a square optical lattice [117].

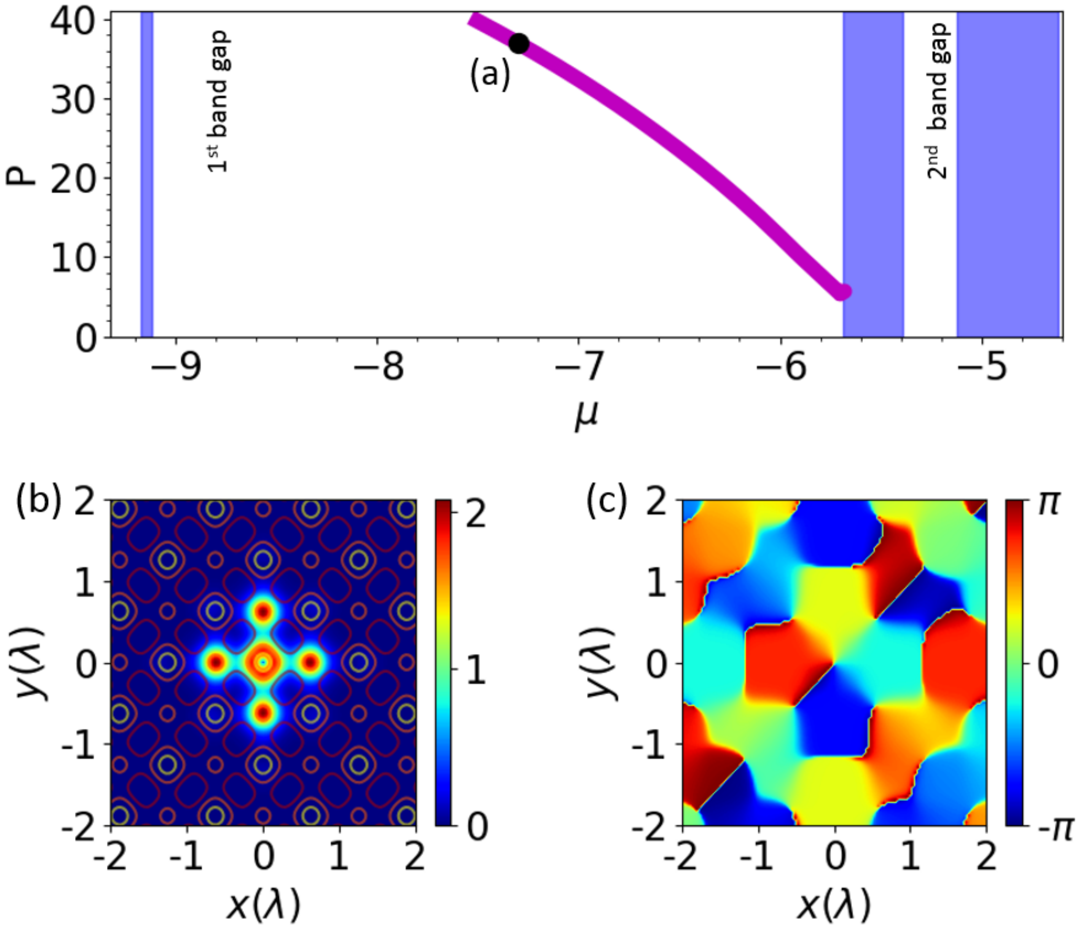

Figure 5.2: The power curve for self-focused vortex soliton in the first bandgap is shown in the top panel. (b) The spatial structure of the vortex at the marked point labeled by (a) of the existing power curve with the color bar represents the peak-to-peak height of the probability density. (c) The phase structure of the gap vortex state with a color bar refers to the phase.

5.3 Defocusing nonlinearity

For the defocusing nonlinearity ($\sigma < 0$), three different power curves are found in the 2^{nd} band gap. Unlike the focusing case, they bifurcate from the second band edge and raise as the chemical potential moves inside the second bandgap (see Fig. 5.3(a)). The corresponding spatial structure of the soliton solution at the marked points (a, b, c) of the power curve are shown in Fig. 5.3(a), (b), (c).

At a chemical potential $\mu = -5.23$ in the second bandgap, the solutions exhibit an out-of-phase dipole aligned along the x-axis in the central deep lattice sites and unipole in the nearest neighbor shallow sites. These soliton solutions show different degrees of localization along different axes (see Fig. 5.3).

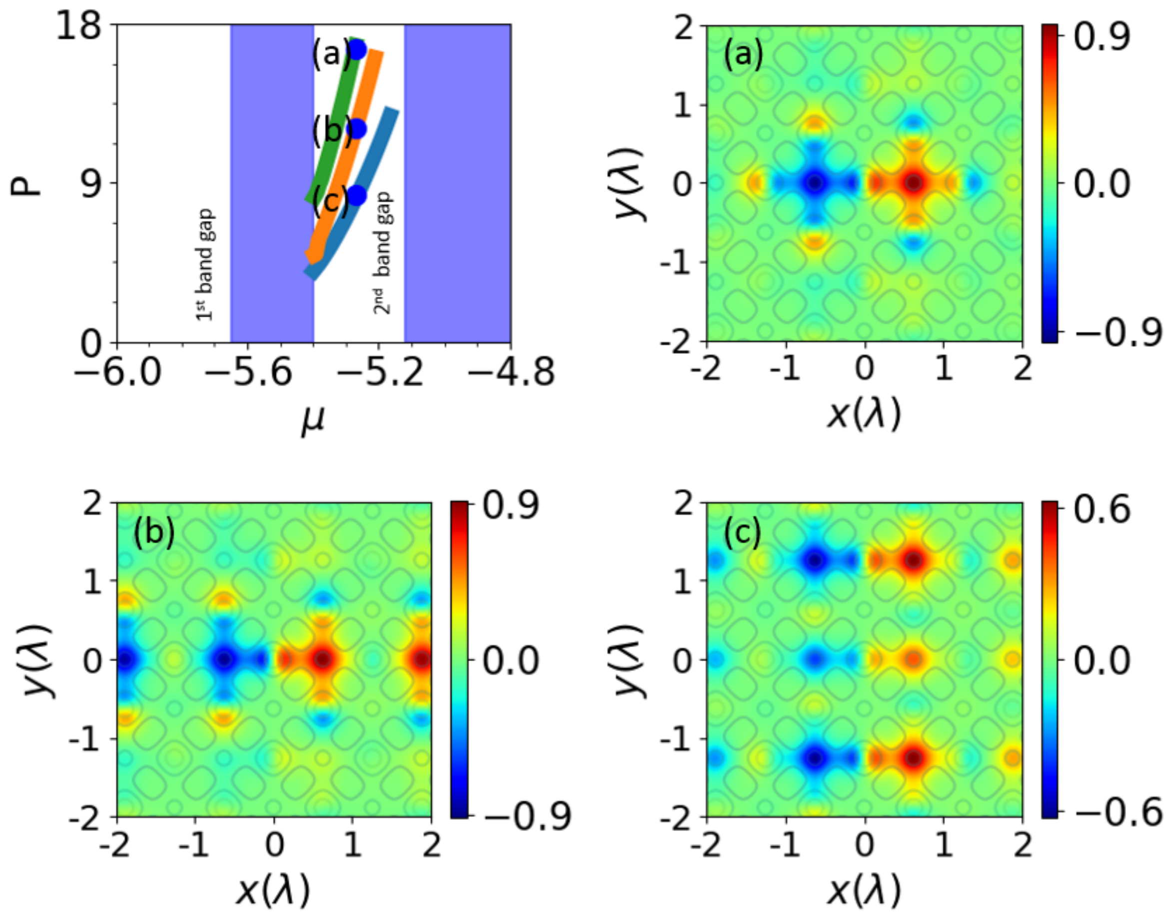

Figure 5.3: The power curve for the self-defocused gap states in the second bandgap. The spatial structure of the self-defocused gap solitons at the marked points corresponding to ($\mu = -5.23$) of the existing power curve are shown in (a),(b),(c). The color bars represent the peak-to-peak height of the wave function.

On the high power branch (green line in Fig. 5.3), the soliton solution at the marked point (a) is shown in Fig. 5.3(a). It is confined to three lattice sites along the x-direction but weakly localized along the y-axis. Thus, this soliton is weakly localized along the y direction and more localized along the x direction. In contrast, on the intermediate-power branch (orange line in Fig. 5.3, the soliton solution (Fig. 5.3(b)) at b is largely confined along the vertical axis and is less localized along the horizontal direction. However, on the lower branch (blue line in Fig. 5.3), the soliton solution shows stronger localization along both x- and y-axes.

5.4 Summary and conclusion

In conclusion, we demonstrated the localization of Bose-Einstein condensates in two-dimensional bipartite optical lattices. We presented solitary wave solutions bifurcated from edges of second Bloch bands in two-dimensional bipartite optical lattice potential. Our calculations reveal that solitary waves can be found under either focusing or defocusing nonlinearity as previously demonstrated for gap solitons, both in the context of BECs and optical waves [117, 113].

Existence of two linearly independent degenerates Bloch modes result in solitary wave solution of various structures such as dipole solitons, vortex solitons, and monopole-dipole solitons. Furthermore, gap solitons with different degrees of localization are observed in the second bandgap. Our findings could have implications in nonlinear topological systems and photonics. They can be used to study localized structures in nonlinear optics and BEC in an optical lattice. In addition, bipartite optical lattices provide a versatile method for studying localized states. For instance, tuning the lattice anisotropy may lead to a rich band-gap structure and hence more gap solitons can be engineered with unique features.

Chapter 6

Conclusion and Future Work

This thesis work comprises two main projects: (1) Experimental realization of He*BEC in optical dipole trap. (2) Numerical investigation of interacting atomic condensate in the p-band of a bipartite optical lattice.

In the first part, we demonstrate a simple experimental scheme to reach He* BEC by direct evaporative cooling in a cross-optical dipole trap, which is the first step towards a new generation of experiments with He* BEC in an optical lattice. A new in vacuum quadrupole-Ioffe configuration magnetic trap is designed to provide good optical access to the condensate cloud. Thus, in the future, more laser beams can be inserted to allow the building of an optical lattice potential. The novel QUIC magnetic trap allows one stage of in-trap cooling, which is sufficient for direct transfer to the dipole trap without the need for any additional evaporative cooling in the magnetic trap. We efficiently load an atomic cloud of $\sim 4.9 \times 10^7$ atoms in the magnetic trap at a temperature of 83 μK after 500 ms of 1D Doppler cooling. The optical dipole loading starts 100 ms prior to the 1D Doppler cooling stage. In the CODT at full power, we measure $\sim 5 \times 10^6$ atoms at 13.5(1) μK with a phase space density of ~ 0.5. After 1 s of evaporative cooling, we produce the pure BEC state with million atoms. Moreover, the entire experimental sequence takes 3.3 s.

Correlation functions are good observables for quantifying and understanding many-body problems. However, it is challenging to measure them with alkaline BECs. As mentioned in the introduction, metastable helium has been used to study the high-order momentum correlations since the individual He* atom is detectable with a high temporal and spatial precision.

The He* BEC group at ANU studied momentum correlation function of various order in two ultracold scattering halos [118]. Alternative approaches have been developed to construct momentum microscopy with other elements [119, 120]. However, these methods are limited to either a small number of atoms or required many experimental cycles. Such a correlation function requires a vast amount of data and hence short experimental sequence is necessary. These requirements are valid in our experimental setup. The efficient production of He* BEC in an optical dipole trap every $\sim$ 3 sec will speed up the data acquisition. Using a hexagonal DLD, a three-dimensional momentum correlation can be extracted with a single atom precision. Therefore our experimental setup offers an effective way to perform three-dimensional momentum microscopy.

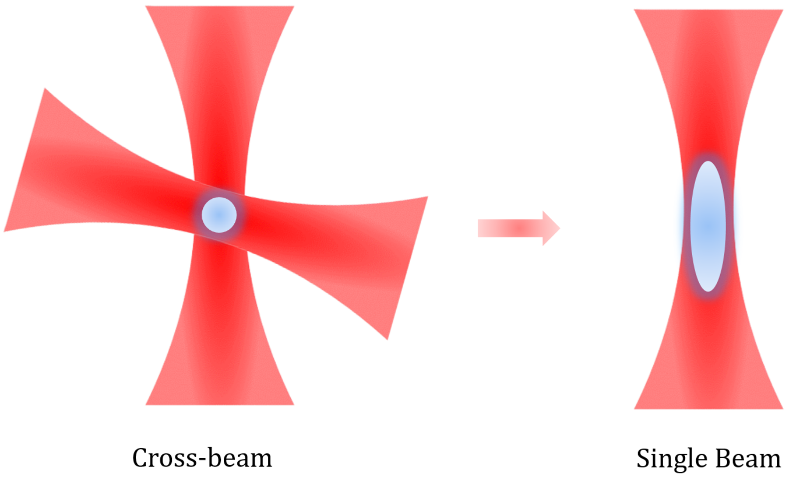

Figure 6.1: 3D confinement of He BEC cloud in cross optical dipole trap. By switching off one of the two beams, the condensate cloud will be confined to a single dipole trap.*

Prospective experiments can be implemented in the future using our current experimental setup (He* BEC in a crossed-beam optical dipole potential). For instance, observing the evolution of the correlation functions following a quantum quench during a dimensional crossover. This can be experimentally achieved by starting with 3D confinement in the CODT followed by 1D confinement in a single by switching off one of the two beams from the crossed optical dipole trap as shown in Fig. 6.1. This configuration offers a clean and well-controlled ultracold atom setup to observe observing the emergence of coherence when the dimensional crossover occurs. Dimensionality plays an important role in understanding physics in low spatial dimensions. The effects of dimensionality and disorder on quantum depletion and condensate density can be studied. Moreover, a long-term plan for the lab is to study the physics of optical lattice potential. Using the advantage of single particle detection, He* BEC in optical lattice potential provides a highly controllable experimental setup to simulate condensed matter Hamiltonians with tunable parameters such as inter-particle interactions and local phase.

In the second part of this dissertation, we present a numerical study to investigate the physics of interacting condensate in the p-band of a bipartite optical lattice potential.

In chapter 4, we numerically investigate the stationary states of an interacting condensate in a bipartite lattice potential. In particular, we apply the coupled-mode theory to investigate the condensates loaded into the p-band with double degenerate minima of a bipartite optical lattice potential. We demonstrate the possibility to create a superposition of Bloch states with a nontrivial orbital texture. Namely, we show that the complex superposition of the two Bloch states at the quasi-degenerate energy minima of the p-band of the 2D bipartite optical potential can lead to the formation of a 2D vortex array with global orbital angular momentum across the entire lattice.

The coupled mode theory is a good approach to study the nonlinear coupling of wavefunctions. As a prospective study, the coupled mode theory can be implemented on different lattice geometry e.g optical lattice with hexagonal boron nitride geometry, in which the chiral state is realized recently [121].

Finally, we have numerically investigated the localization of BECs loaded into the first excited state of a two-dimensional bipartite optical lattice. By implementing an iterative method, the nonlinear limit of the GPE is solved numerically with both attractive and repulsive interactions. we study the bifurcation of gap solitons away from the upper and lower edges of the first excited band.

We find that the two-dimensional bipartite optical lattice admits monopole and dipole gap solitons. The existence of two-dimensional spatially localized states such as dipole and vortex solitons are reported in the first bandgap under focusing nonlinearity. These solitons are associated with the topology of the lattice potential. Gap solitons with different degrees of localization are bifurcated from the edge of the first excited state into the second bandgap under defocusing nonlinearity. These findings are highly relevant to localized structures in nonlinear optics and atomic matter waves.

In conclusion, the bipartite optical lattice potential provides a rich system for investigating physics beyond the *Tight Binding Model* (TBM). It exhibits a unique band structure with many tunable parameters such as lattice anisotropy (ϵ) and the relative phase θ. Tweaking these parameters may lead to new topological states. This system can provide a reconfigurable novel band-gap structure which can be useful for studying localization in photonic crystals and nonlinear optics.

Bibliography

[1] Pethick, C. & Smith, H. *Bose-Einstein Condensation in Dilute Bose Gases (2nd ed.)* (Cambridge University Press, 2008). URL https://doi.org/10.1017/CBO9780511802850.

[2] Pitaevskii, L. & Stringari., S. *Bose-Einstein Condensation.* (Oxford University Press, 2003). URL https://doi.org/10.1093/acprof:oso/9780198758884.001.0001.

[3] Manni, F., Lagoudakis, K. G., André, R., Wouters, M. & Deveaud, B. Penrose-onsager criterion validation in a one-dimensional polariton condensate. *Phys. Rev. Lett.* **109**, 150409 (2012). URL https://link.aps.org/doi/10.1103/PhysRevLett.109.150409.

[4] Penrose, O. & Onsager, L. Bose-einstein condensation and liquid helium. *Phys. Rev.* **104**, 576–584 (1956). URL https://link.aps.org/doi/10.1103/PhysRev.104.576.

[5] Greiner, M. *Ultracold quantum gases in three-dimensional optical lattice potentials.* (Dissertation in the Physics department of the Ludwig-Maximilians-Universität München, 2003). URL https://edoc.ub.uni-muenchen.de/968/.

[6] Harold J. Metcalf, P. S. *Laser Cooling and Trapping.* (Springer, 1999). URL https://doi.org/10.1007/978-1-4612-1470-0.

[7] Grimm, R., Weidemüller, M. & Ovchinnikov, Y. B. Optical dipole traps for neutral atoms **42**, 95–170 (2000). URL https://doi.org/10.1016/S1049-250X(08)60186-X.

[8] Patil., R. *Correlation Dynamics and Single-Atom Detection with Ultracold Metastable Helium.* (Indian Institute of Science Education and Research Pune Press, 2020). URL https://dr.iiserpune.ac.in:8080/jspui/bitstream/123456789/4677/1/.

[9] Anderson, M. H., Ensher, J. R., Matthews, M. R., Wieman, C. E. & Cornell, E. A. Observation of bose-einstein condensation in a dilute atomic vapor. *Science* **269**, 198–201 (1995). URL http://dx.doi.org/10.1126/science.269.5221.198.

[10] Davis, K. B., Mewes, M., Andrews, M. R. & Ketterle, W. Bose-einstein condensation in a gas of sodium atoms. *Phys. Rev. Lett.* **75**, 3969–3973 (1995). URL https://link.aps.org/doi/10.1103/PhysRevLett.75.3969.

[11] Bloch, I., Dalibard, J. & Zwerger, W. Many-body physics with ultracold gases. *Rev. Mod. Phys.* **80**, 885–964 (2008). URL https://link.aps.org/doi/10.1103/RevModPhys.80.885.

[12] Cooper, N. R., Dalibard, J. & Spielman, I. B. Topological bands for ultracold atoms. *Rev. Mod. Phys.* **91**, 015005 (2019). URL https://link.aps.org/doi/10.1103/RevModPhys.91.015005.

[13] Geiger, R., Landragin, A., Merlet, S. & Pereira Dos Santos, F. High-accuracy inertial measurements with cold-atom sensors. *AVS Quantum Science* **2**, 024702 (2020). URL https://doi.org/10.1116/5.0009093.

[14] Courteille, P., Freeland, R. S., Heinzen, D. J., van Abeelen, F. A. & Verhaar, B. J. Observation of a feshbach resonance in cold atom scattering. *Phys. Rev. Lett.* **81**, 69–72 (1998). URL https://link.aps.org/doi/10.1103/PhysRevLett.81.69.

[15] Inouye, S., Andrews, M. R., Stenger, J. & Ketterle, W. Observation of feshbach resonances in a bose–einstein condensate. *Nature* **81**, 392–151 (1998). URL https://doi.org/10.1038/32354.

[16] Bloch, I., Dalibard, J. & Zwerger, W. Many-body physics with ultracold gases. *Rev. Mod. Phys.* **80**, 885–964 (2008). URL https://link.aps.org/doi/10.1103/RevModPhys.80.885.

[17] Ott, H. Single atom detection in ultracold quantum gases: a review of current progress. *Rep. Prog. Phys.* **79**, 054401 (2016). URL https://iopscience.iop.org/article/10.1088/0034-4885/79/5/054401.

[18] Bakr, W. S., Gillen, J. I., Peng, A., Fölling, S. & Greiner, M. A quantum gas microscope for detecting single atoms in a hubbard-regime optical lattice. *Nature* **462**, 74–77 (2009). URL http://www.nature.com/nature/journal/v462/n7269/full/nature08482.html.

[19] Sherson, J., Weitenberg, C., Bloch, I. & Kuhr, S. Single-atom-resolved fluorescence imaging of an atomic mott insulator. *Nature* **467**, 68–72 (2010). URL http://www.nature.com/nature/journal/v467/n7311/full/nature09378.html.

[20] Bücker, R., Perrin, A., Manz, S., Schumm, T. & Schmiedmayer, J. Single-particle-sensitive imaging of freely propagating ultracold atoms. *New Journal of Physics* **11**, 103039 (2009). URL https://doi.org/10.1088/1367-2630/11/10/103039.

[21] Bergschneider, A., Klinkhamer, V. M., Becher, J. H. & Jochim, S. Spin-resolved single-atom imaging of ^{6}Li in free space. *Phys. Rev. A* **97**, 063613 (2018). URL https://aip.scitation.org/doi/pdf/10.1063/1.1820524.

[22] Vassen, W., Cohen-Tannoudji, C., Leduc, M., Truscott, A. & Trippenbach, M. Cold and trapped metastable noble gases. *Rev. Mod. Phys.* **84**, 175–210 (2012). URL http://link.aps.org/doi/10.1103/RevModPhys.84.175.

[23] Schellekens, M., Hoppeler, R., Perrin, A. & Westbrook, C. I. Hanbury brown twiss effect for ultracold quantum gases. *Science* **310**, 648–651 (2005). URL http://science.sciencemag.org/content/310/5748/648.

[24] Manning, A. G., Khakimov, R. I., Dall, R. G. & Truscott, A. G. Wheeler's delayed-choice gedanken experiment with a single atom. *Nature Phys.* **11**, 539–542 (2015). URL https://doi.org/10.1038/nphys3343.

[25] Lopes, R., Imanaliev, A., Aspect, A., Cheneau, M. & Westbrook, C. I. Atomic hong–ou–mandel experiment. *Nature* **520**, 66–68 (2015). URL https://doi.org/10.1038/nature14331.

[26] Khakimov R. I., Henson B. M., Shin D. K., Hodgman S. S. & Truscott A. G. Ghost imaging with atoms. *Nature* **540**, 100–103 (2016). URL http://dx.doi.org/10.1038/nature20154.

[27] Shin, D. K., Henson, B. M., Hodgman, S. S., Wasak, T. & Truscott, A. G. Bell correlations between spatially separated pairs of atoms. *Nature Communications* **10**, 4447 (2019). URL https://doi.org/10.1038/s41467-019-12192-8.

[28] Drake, G. & Yan., Z.-C. High precision spectroscopy as a test of quantum electrodynamics in light atomic systems. *Canadian Journal of Physics.* **86**, 45–54 (2008). URL https://doi.org/10.1139/p07-154.

[29] Vassen, W., Cohen-Tannoudji, C. & Trippenbach, M. Cold and trapped metastable noble gases. *Rev. Mod. Phys.* **84**, 175–210 (2012). URL https://link.aps.org/doi/10.1103/RevModPhys.84.175.

[30] Leo, P. J., Venturi, V., Whittingham, I. B. & Babb, J. F. Ultracold collisions of metastable helium atoms. *Phys. Rev. A* **64**, 042710 (2001). URL https://link.aps.org/doi/10.1103/PhysRevA.64.042710.

[31] Shlyapnikov, G. V., Walraven, J. T. M., Rahmanov, U. M. & Reynolds, M. W. Decay kinetics and bose condensation in a gas of spin-polarized triplet helium. *Phys. Rev. Lett.* **73**, 3247–3250 (1994). URL https://link.aps.org/doi/10.1103/PhysRevLett.73.3247.

[32] Haller, E., Gustvasson, M., Manfred, J. M., Johann, G. D. & Nägerl, H. Realization of an excited, strongly correlated quantum gas phase. *SCIENCE* **325**, 1224–1227 (2009). URL https://www.science.org/doi/10.1126/science.1175850.

[33] Haller, E., Mark, M. J., Hart, R. & Nägerl, H.-C. Confinement-induced resonances in low-dimensional quantum systems. *Phys. Rev. Lett.* **104**, 153203 (2010). URL https://link.aps.org/doi/10.1103/PhysRevLett.104.153203.

[34] Lamporesi, G., Catani, J., Barontini, G., Nishida, Y. & Minardi, F. Scattering in mixed dimensions with ultracold gases. *Phys. Rev. Lett.* **104**, 153202 (2010). URL https://link.aps.org/doi/10.1103/PhysRevLett.104.153202.

[35] Bergeman, T., Moore, M. G. & Olshanii, M. Atom-atom scattering under cylindrical harmonic confinement: Numerical and analytic studies of the confinement induced resonance. *Phys. Rev. Lett.* **91**, 163201 (2003). URL https://link.aps.org/doi/10.1103/PhysRevLett.91.163201.

[36] Olshanii, M. Atomic scattering in the presence of an external confinement and a gas of impenetrable bosons. *Phys. Rev. Lett.* **81**, 938–941 (1998). URL https://link.aps.org/doi/10.1103/PhysRevLett.81.938.

[37] Petrov, D. S., Holzmann, M. & Shlyapnikov, G. V. Bose-einstein condensation in quasi-2d trapped gases. *Phys. Rev. Lett.* **84**, 2551–2555 (2000). URL https://link.aps.org/doi/10.1103/PhysRevLett.84.2551.

[38] Robert, A., Sirjean, O., Browaeys, A., Poupard, J. & Aspect, A. A bose-einstein condensate of metastable atoms. *Science* **292**, 461–464 (2001). URL https://science.sciencemag.org/content/292/5516/461.

[39] Pereira Dos Santos, F., Léonard, J., Wang, J., Barrelet, C. J. & Cohen-Tannoudji, C. Bose-einstein condensation of metastable helium. *Phys. Rev. Lett.* **86**, 3459–3462 (2001). URL https://link.aps.org/doi/10.1103/PhysRevLett.86.3459.

[40] Tychkov, A. S., Jeltes, T., McNamara, J. M., Herschbach, N. & Vassen, W. Metastable helium bose-einstein condensate with a large number of atoms. *Phys. Rev. A* **73**, 031603 (2006). URL https://link.aps.org/doi/10.1103/PhysRevA.73.031603.

[41] Dall, R. & Truscott, A. Bose–Einstein condensation of metastable helium in a bi-planar quadrupole Ioffe configuration trap. *Opt. Commun.* **270**, 255 – 261 (2007). URL http://www.sciencedirect.com/science/article/pii/S0030401806009680.

[42] Keller, M., Kotyrba, M., Leupold, F., Ebner, M. & Zeilinger, A. Bose-einstein condensate of metastable helium for quantum correlation experiments. *Phys. Rev. A* **90**, 063607 (2014). URL https://link.aps.org/doi/10.1103/PhysRevA.90.063607.

[43] Flores, A. S., Mishra, H. P., Vassen, W. & Knoop, S. Simple method for producing bose–einstein condensates of metastable helium using a single-beam optical dipole trap. *Appl. Phys. B* **121**, 391–399 (2015). URL https://doi.org/10.1007/s00340-015-6243-5.

[44] Bouton, Q., Chang, R., Hoendervanger, A. L., Nogrette, F. & Clément, D. Fast production of bose-einstein condensates of metastable helium. *Phys. Rev. A* **91**, 061402 (2015). URL https://link.aps.org/doi/10.1103/PhysRevA.91.061402.

[45] Shin, D. K., Bryce, M. H., Roman, I. K., Jacob, A. R. & Andrew, G. T. Widely tunable, narrow linewidth external-cavity gain chip laser for spectroscopy between 1.0-1.1 μ m. *Opt. Express* **24**, 27403–27414 (2016). URL https://doi.org/10.1364/OE.24.027403.

[46] Shin., D. *Nonlocal correlations between freely propagating pairs of atoms.* (The Australian National University Press, 2022). URL https://hdl.handle.net/1885/267367.

[47] Abbas, A. H., Meng, X., Ross, J. A., Truscott, A. G. & Hodgman, S. S. Rapid generation of metastable helium bose-einstein condensates. *Phys. Rev. A* **103**, 053317 (2021). URL https://link.aps.org/doi/10.1103/PhysRevA.103.053317.

[48] Byron, L. J., Dall, R. G. & Truscott, A. G. Trap loss in a metastable helium-rubidium magneto-optical trap. *Phys. Rev. A* **81**, 013405 (2010). URL https://link.aps.org/doi/10.1103/PhysRevA.81.013405.

[49] Uhlmann, L. J., Dall, R. G., Truscott, A. G., Hoogerland, M. D. & Buckman, S. J. Electron collisions with laser cooled and trapped metastable helium atoms: Total scattering cross sections. *Phys. Rev. Lett.* **94**, 173201 (2005). URL https://link.aps.org/doi/10.1103/PhysRevLett.94.173201.

[50] Hodgman, S. S., Dall, R. G., Baldwin, K. G. H. & Truscott, A. G. Complete ground-state transition rates for the helium 2 ^3p manifold. *Phys. Rev. A* **80**, 044501 (2009). URL https://link.aps.org/doi/10.1103/PhysRevA.80.044501.

[51] Dall, A. G., R. G.and Manning, Hodgman, S. S., RuGway, W., Kheruntsyan, K. V. & Truscott, A. G. Ideal n-body correlations with massive particles. *Na-*

ture Phys. **9**, 341–344 (2013). URL http://www.nature.com/nphys/journal/v9/n6/abs/nphys2632.html#supplementary-information.

[52] Hodgman, S. S., Khakimov, R. I., Lewis-Swan, R. J., Truscott, A. G. & Kheruntsyan, K. V. Solving the quantum many-body problem via correlations measured with a momentum microscope. *Phys Rev Lett* **118**, 240402 (2017). URL https://link.aps.org/doi/10.1103/PhysRevLett.118.240402.

[53] Swansson, J., Baldwin, K., Hoogerland, M., Truscott, A. & Buckman, S. A high flux, liquid-helium cooled source of metastable rare gas atoms. *Appl. Phys. B* **79**, 485–489 (2004). URL https://doi.org/10.1007/s00340-004-1600-9.

[54] Phillips, W. D. & Metcalf., H. Laser deceleration of an atomic beam. *Phys. Rev. Lett.* **49**, 596–599 (1982). URL http://link.aps.org/doi/10.1103/PhysRevLett.48.596,.

[55] Simonet., J. *Optical traps for Ultracold Metastable Helium atoms, de l'hélium métastable. PhD thesis* (Université Pierre et Marie Curie., 2011). URL https://tel.archives-ouvertes.fr/tel-00651592.

[56] Tol, P. J. J., Herschbach, N., Hessels, E. A., Hogervorst, W. & Vassen, W. Large numbers of cold metastable helium atoms in a magneto-optical trap. *Phys. Rev. A* **60**, R761–R764 (1999). URL https://link.aps.org/doi/10.1103/PhysRevA.60.R761.

[57] Mewes, M.-O., Andrews, M. R., van Druten, N. J., Durfee, D. S. & Ketterle, W. Bose-einstein condensation in a tightly confining dc magnetic trap. *Phys. Rev. Lett.* **77**, 416–419 (1996). URL https://link.aps.org/doi/10.1103/PhysRevLett.77.416.

[58] Esslinger, T., Bloch, I. & Hänsch, T. W. Bose-einstein condensation in a quadrupole-ioffe-configuration trap. *Phys. Rev. A* **58**, R2664–R2667 (1998). URL https://link.aps.org/doi/10.1103/PhysRevA.58.R2664.

[59] Fortágh, J. & Zimmermann, C. Magnetic microtraps for ultracold atoms. *Rev. Mod. Phys.* **79**, 235–289 (2007). URL https://link.aps.org/doi/10.1103/RevModPhys.79.235.

[60] Petrich, W., Anderson, M. H., Ensher, J. R. & Cornell, E. A. Stable, tightly confining magnetic trap for evaporative cooling of neutral atoms. *Phys. Rev. Lett.* **74**, 3352–3355 (1995). URL https://link.aps.org/doi/10.1103/PhysRevLett.74.3352.

[61] Yavin, I., Weel, M., Andreyuk, A. & Kumarakrishnan, A. A calculation of the time-of-flight distribution of trapped atoms. *American Journal of Physics* **70**, 149–152 (2002). URL https://doi.org/10.1119/1.1424266.

[62] Dalfovo, F., Giorgini, S., Pitaevskii, L. P. & Stringari, S. Theory of bose-einstein condensation in trapped gases. *Rev. Mod. Phys.* **71**, 463–512 (1999). URL https://link.aps.org/doi/10.1103/RevModPhys.71.463.

[63] Castin, Y. & Dum, R. Bose-einstein condensates in time dependent traps. *Phys. Rev. Lett.* **77**, 5315–5319 (1996). URL https://link.aps.org/doi/10.1103/PhysRevLett.77.5315.

[64] Grynberg, G. Cold atoms in dissipative optical lattices. *Phys. Rep.* **355**, 335 – 451 (2001). URL https://doi.org/10.1016/S0370-1573(01)00017-5.

[65] Greiner, M., Mandel, O., Esslinger, T., Hänsch, T. & Bloch, I. Quantum phase transition from a superfluid to a mott insulator in a gas of ultracold atoms. *Nature.* **415**, 39–44 (2002). URL https://www.nature.com/articles/415039a.

[66] Ladd, T., Jelezko, F., Laflamme, R., Nakamura, C. & O'Brien., J. L. Quantum computers. *Nature.* **464**, 45–53 (2010). URL https://doi.org/10.1038/nature08812.

[67] Gould, P. L., Ruff, G. A. & Pritchard, D. E. Diffraction of atoms by light: The near-resonant kapitza-dirac effect. *Phys. Rev. Lett.* **56**, 827–830 (1986). URL https://link.aps.org/doi/10.1103/PhysRevLett.56.827.

[68] Ashida, Y. & Ueda, M. Diffraction-unlimited position measurement of ultracold atoms in an optical lattice. *Phys. Rev. Lett.* **115**, 095301 (2015). URL https://link.aps.org/doi/10.1103/PhysRevLett.115.095301.

[69] C.S Adams, J., M.Sigel. Atom optics. *Physics Reports.* **240**, 143–210 (1994). URL https://www.sciencedirect.com/science/article/pii/0370157394900663.

[70] Russell, P. Photonic crystal fibers. *Science.* **299** (2003). URL https://www.science.org/doi/10.1126/science.1079280.

[71] Eisenberg, H. S., Silberberg, Y., Morandotti, R., Boyd, A. R. & Aitchison, J. S. Discrete spatial optical solitons in waveguide arrays. *Phys. Rev. Lett.* **81**, 3383–3386 (1998). URL https://link.aps.org/doi/10.1103/PhysRevLett.81.3383.

[72] Bednorz, K., J. Muller. Possible high tc superconductivity in the ba-la-cu-o system. *Zeitschrift fur Physik B Condensed Matter.* **64**, 189–193 (1986). URL https://link.springer.com/article/10.1007/BF01303701#citeas.

[73] Kamihara, Y. e. a. Piron-based layered superconductor: Laofep. *J. Am. Chem. Soc.* **128**, 10012–10013 (2006). URL https://pubs.acs.org/doi/10.1021/ja063355c.

[74] von Helmolt, R., Wecker, J., Holzapfel, B., Schultz, L. & Samwer, K. Giant negative magnetoresistance in perovskitelike $\mathrm{la}_{2/3}\mathrm{ba}_{1/3}\mathrm{mno}_x$ ferromagnetic films. *Phys. Rev. Lett.* **71**, 2331–2333 (1993). URL https://link.aps.org/doi/10.1103/PhysRevLett.71.2331.

[75] Kallin., C. Chiral p-wave order in sr_2ruo_4. *Rep. Prog. Phys.* **75**, 4 (2012). URL https://iopscience.iop.org/article/10.1088/0034-4885/75/4/042501.

[76] Feynman., R. P. *Statistical Mechanics* (Addison-Wesley Publishing Company, 1972). URL https://doi.org/10.1201/9780429493034.

[77] Wirth, G., Ölschläger, M. & Hemmerich, A. Evidence for orbital superfluidity in the p-band of a bipartite optical square lattice. *Nature Phys.* **7**, 015302 (2011). URL https://doi.org/10.1038/nphys1857.

[78] Soltan-Panahi, P., Lühmann, D. & Struck, J. Quantum phase transition to unconventional multi-orbital superfluidity in optical lattices. *Nature phys.* **8**, 71–75 (2012). URL https://doi.org/10.1038/nphys2128.

[79] Kock, T., Ölschläger, M., Mathey, L. & Hemmerich, A. Observing chiral superfluid order by matter-wave interference. *Phys. Rev. Lett.* **114**, 115301 (2015). URL https://link.aps.org/doi/10.1103/PhysRevLett.114.115301.

[80] Xiaopeng, L. & W Vincent, L. Physics of higher orbital bands in optical lattices: a review. *Rep. Prog. Phys.* **79**, 116401 (2016). URL https://iopscience.iop.org/article/10.1088/0034-4885/79/11/116401.

[81] Zhou, Q., Porto, J. V. & Das Sarma, S. Condensates induced by interband coupling in a double-well lattice. *Phys. Rev. B* **83**, 195106 (2011). URL https://link.aps.org/doi/10.1103/PhysRevB.83.195106.

[82] Zhang, Z., Hung, H.-H., Ho, C. M., Zhao, E. & Liu, W. V. Modulated pair condensate of p-orbital ultracold fermions. *Phys. Rev. A* **82**, 033610 (2010). URL https://link.aps.org/doi/10.1103/PhysRevA.82.033610.

[83] Sun, K., Liu, W. V., Hemmerich, A. & Sarma, S. D. Topological semimetal in a fermionic optical lattice. *Nat. Phys.* **8**, 67 (2012). URL https://doi.org/10.1038/nphys2134.

[84] Isacsson, A. & Girvin, S. M. Multiflavor bosonic hubbard models in the first excited bloch band of an optical lattice. *Phys. Rev. A* **72**, 053604 (2005). URL https://link.aps.org/doi/10.1103/PhysRevA.72.053604.

[85] Clarice, D., Aiello, John, M. & Abendroth, e. A chirality-based quantum leap. *ACS Nano* **16**, 4989–5035 (2022). URL https://pubs.acs.org/doi/10.1021/acsnano.1c01347.

[86] Pukrop, M., Schumacher, S. & Ma, X. Circular polarization reversal of half-vortex cores in polariton condensates. *Phys. Rev. B* **101**, 205301 (2020). URL https://link.aps.org/doi/10.1103/PhysRevB.101.205301.

[87] Cowburn, R. Change of direction. *Nature Mater.* **6**, 255–256 (2007). URL https://doi.org/10.1038/nmat1877.

[88] Thomas, J. Vortex ups and downs. *Nature Nanotech.* **2** (2007). URL https://doi.org/10.1038/nnano.2007.102.

[89] Cai, Z. & Wu, C. Complex and real unconventional bose-einstein condensations in high orbital bands. *Phys. Rev. A* **84**, 033635 (2011). URL https://link.aps.org/doi/10.1103/PhysRevA.84.033635.

[90] Ölschläger, M., Wirth, G. & Hemmerich, A. Unconventional superfluid order in the f band of a bipartite optical square lattice. *Phys. Rev. Lett.* **106**, 015302 (2011). URL https://link.aps.org/doi/10.1103/PhysRevLett.106.015302.

[91] Smerzi, A., Fantoni, S., Giovanazzi, S. & Shenoy, S. R. Quantum coherent atomic tunneling between two trapped bose-einstein condensates. *Phys. Rev. Lett.* **79**, 4950–4953 (1997). URL https://link.aps.org/doi/10.1103/PhysRevLett.79.4950.

[92] EA Ostrovskaya, M. L. B. H. F. C. D. A., YS Kivshar. *Physical Review A.* **61**, 031601 (2000).

[93] Gao, T., Egorov, O. A., Estrecho, A. G., E.and Truscott & Ostrovskaya, E. A. Controlled ordering of topological charges in an exciton-polariton chain. *Phys. Rev. Lett.* **121**, 225302 (2018). URL https://link.aps.org/doi/10.1103/PhysRevLett.121.225302.

[94] Ostrovskaya, E. A. *et al.* Coupled-mode theory for bose-einstein condensates. *Phys. Rev. A* **61**, 031601 (2000). URL https://link.aps.org/doi/10.1103/PhysRevA.61.031601.

[95] F.Kh. Abdullaev, M. W., J.S. Shaari. Coupled-mode theory for bose–einstein condensates with time dependent atomic scattering length. *Physics Letters A* **345**, 237–244 (2005). URL https://doi.org/10.1016/j.physleta.2005.07.011.

[96] Silberberg, Y. & Stegeman., G. I. Nonlinear coupling of waveguide modes. *Appl. Phys. Lett.* **50** (1987). URL https://doi.org/10.1063/1.98049.

[97] Abbas, A. H. Chiral superfluid in a one-dimensional bipartite optical lattice. *Phys. Rev. A* **105**, 023327 (2022). URL https://link.aps.org/doi/10.1103/PhysRevA.105.023327.

[98] Mingaleev, S. F. & Kivshar, Y. S. Nonlinear transmission and light localization in photonic-crystal waveguides. *J. Opt. Soc. Am. B* **19**, 2241–2249 (2002). URL https://doi.org/10.1364/JOSAB.19.002241.

[99] Sakoda, K. *Optical Properties of Photonic Crystals* (Springer, 2001). URL https://link.springer.com/book/10.1007/b138376.

[100] Pu, H., Baksmaty, L. O., Zhang, W., Bigelow, N. P. & Meystre, P. Effective-mass analysis of bose-einstein condensates in optical lattices: Stabilization and levitation. *Phys. Rev. A* **67**, 043605 (2003). URL https://link.aps.org/doi/10.1103/PhysRevA.67.043605.

[101] Ostrovskaya, E. A. & Kivshar, Y. S. Photonic crystals for matter waves: Bose-einstein condensates in optical lattices. *Opt. Express* **12**, 19–29 (2004). URL https://doi.org/10.1364/OPEX.12.000019.

[102] Bartal, G., Manela, O., Cohen, O., Fleischer, J. W. & Segev, M. Observation of second-band vortex solitons in 2d photonic lattices. *Phys. Rev. Lett.* **95**, 053904 (2005). URL https://link.aps.org/doi/10.1103/PhysRevLett.95.053904.

[103] Fischer, R., Träger, D., Neshev, D. N., Sukhorukov, A. A. & Kivshar, Y. S. Reduced-symmetry two-dimensional solitons in photonic lattices. *Phys. Rev. Lett.* **96**, 023905 (2006). URL https://link.aps.org/doi/10.1103/PhysRevLett.96.023905.

[104] Song, D., Lou, C., J.H., K., Jingjun, X. & Chen, Z. Self-trapping of optical vortices at the surface of an induced semi-infinite photonic lattice. *Opt. Express* **18**, 5873–5878 (2010). URL https://doi.org/10.1364/OE.18.005873.

[105] Wang, J. & Yang, J. Families of vortex solitons in periodic media. *Phys. Rev. A* **77**, 033834 (2008). URL https://link.aps.org/doi/10.1103/PhysRevA.77.033834.

[106] Cerda-Méndez, E. A. *et al.* Exciton-polariton gap solitons in two-dimensional lattices. *Phys. Rev. Lett.* **111**, 146401 (2013). URL https://link.aps.org/doi/10.1103/PhysRevLett.111.146401.

[107] Meng, H., Zhou, Y., Li, X., Wang, W. & ren Shi, Y. Gap solitons in bose–einstein condensate loaded in a honeycomb optical lattice: Nonlinear dynamical stability, tunneling, and self-trapping. *Physica A-statistical Mechanics and Its Applications* **577**, 126087 (2021). URL https://doi.org/10.1016/j.physa.2021.126087.

[108] Solnyshkov, D. D., Bleu, O., Teklu, B. & Malpuech, G. Chirality of topological gap solitons in bosonic dimer chains. *Phys. Rev. Lett.* **118**, 023901 (2017). URL https://link.aps.org/doi/10.1103/PhysRevLett.118.023901.

[109] Zhang, Y., Xu, Y. & Busch, T. Gap solitons in spin-orbit-coupled bose-einstein condensates in optical lattices. *Phys. Rev. A* **91**, 043629 (2015). URL https://link.aps.org/doi/10.1103/PhysRevA.91.043629.

[110] Lobanov, V. E., Kartashov, Y. V. & Konotop, V. V. Fundamental, multipole, and half-vortex gap solitons in spin-orbit coupled bose-einstein condensates. *Phys. Rev. Lett.* **112**, 180403 (2014). URL https://link.aps.org/doi/10.1103/PhysRevLett.112.180403.

[111] Cheng, S.-C. & Chen, T.-W. Dark gap solitons in exciton-polariton condensates in a periodic potential. *Phys. Rev. E* **97**, 032212 (2018). URL https://link.aps.org/doi/10.1103/PhysRevE.97.032212.

[112] Chen, T.-W. & Cheng, S.-C. Surface gap solitons in exciton polariton condensates. *Phys. Rev. E* **98**, 032212 (2018). URL https://link.aps.org/doi/10.1103/PhysRevE.98.032212.

[113] Yang, J. Newton-conjugate-gradient methods for solitary wave computations. *Journal of Computational Physics* **228**, 7007–7024 (2009). URL https://doi.org/10.1016/j.jcp.2009.06.012.

[114] Shi, Z. & Yang, J. Solitary waves bifurcated from bloch-band edges in two-dimensional periodic media. *Phys. Rev. E* **75**, 056602 (2007). URL https://link.aps.org/doi/10.1103/PhysRevE.75.056602.

[115] Hestenes, M. R. & Stiefel, E. Methods of conjugate gradients for solving linear systems. *Journal of Research of the National Bureau of Standards.* **49**, 409–436 (1952). URL https://doi.org/10.6028/jres.049.044.

[116] Bartal, G., Manela, O., Cohen, O., Fleischer, J. W. & Segev, M. Observation of second-band vortex solitons in 2d photonic lattices. *Phys. Rev. Lett.* **95**, 053904 (2005). URL https://link.aps.org/doi/10.1103/PhysRevLett.95.053904.

[117] Ostrovskaya, E. A. & Kivshar, Y. S. Matter-wave gap vortices in optical lattices. *Phys. Rev. Lett.* **93**, 160405 (2004). URL https://link.aps.org/doi/10.1103/PhysRevLett.93.160405.

[118] Hodgman, S. S., Khakimov, R. I., Lewis-Swan, R. J., Truscott, A. G. & Kheruntsyan, K. V. Solving the quantum many-body problem via correlations measured with a momentum microscope. *Phys. Rev. Lett.* **118**, 240402 (2017). URL https://link.aps.org/doi/10.1103/PhysRevLett.118.240402.

[119] Bergschneider, A., Klinkhamer, V. M., Becher, J. H., Preiss, P. M. & Jochim, S. Spin-resolved single-atom imaging of ^{6}Li in free space. *Phys. Rev. A* **97**, 063613 (2018). URL https://link.aps.org/doi/10.1103/PhysRevA.97.063613.

[120] Bücker, R., Perrin, A., Manz, S. & Schmiedmayer, J. Single-particle-sensitive imaging of freely propagating ultracold atoms. *New Journal of Physics* **11**, 103039 (2009). URL https://doi.org/10.1088/1367-2630/11/10/103039.

[121] Wang, X.-Q., Luo, G.-Q., , W., Liu, Hemmerich, A. & Xu, Z.-F. Evidence for an atomic chiral superfluid with topological excitations. *Nature.* **596**, 227–231 (2021). URL https://doi.org/10.1038/s41586-021-03702-0.